Topics in Quantum Measurement of Many-Body Systems

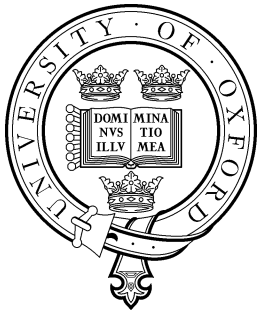

Thomas Joseph Elliott

Lincoln College

University of Oxford

A thesis submitted for the degree of

Doctor of Philosophy

Trinity 2016

Abstract

In quantum physics, measurement exhibits fundamentally different behaviour to the classical case, having direct effect on the observed system. As a result, the very act of observation in quantum systems plays a non-trivial role, and can be used as a method of controlling the dynamics of the system. With the rise of quantum technologies, understanding and exploiting these phenomena offers a great boon. Here, we investigate a selection of the possibilities offered by quantum measurement for characterising and manipulating many-body systems, with particular focus on ultracold atomic gases.

We first study how microscopic quantum structures can be used to indirectly probe larger systems. After deriving a general result, we consider the specific case of impurity atoms immersed in a quantum gas, and demonstrate that this enables density-related properties of the gas to be inferred from measurements of solely the impurity internal state. Following this, we explore how the backaction from measurement can be used for control of quantum systems. Utilising the quantum Zeno effect that results from persistent measurement of a quantum state, we show how fully-quantum many-body light-matter interactions enable the engineering of atomic states and dynamics through measurement of the light, leading to an abundance of interesting phenomena, including genuinely multipartite entangled states, long-range correlated tunnelling, and the quantum simulation of long-range and correlated interactions. The resulting structure imparted by the light on the matter can also be used to detect and measure atomic entanglement. Finally, we generalise quantum Zeno dynamics to the regime where the measurement timestep is finite, and demonstrate that the resulting system evolution can exhibit correlated processes.

To Gizmo, Boris, Dudley, Charlie, Ace, Billy, Sooty, and Sam.

"There's always *bloody quantum."*

— Terry Pratchett, Night Watch

Acknowledgements

Firstly, I would like to thank my supervisor, Vlatko Vedral. His guidance and friendship have been both major assets and a great pleasure, and I am honoured to have worked with such a talented physicist. I hope our collaboration continues into the future. I extend this thanks also to the members of the Vedral group in Oxford, and the associated contingent in Singapore, themselves also a pack of wonderful, genial, and talented physicists.

I would also like to thank members of the Jaksch group with whom I have collaborated and/or had discussions about physics. I especially thank Tomi Johnson, who was instrumental in my first experiences as a theoretical quantum physicist, during my tenure as a summer project student and throughout my MPhys project. I gained much valued insight and knowledge while working with Tomi, Stephen Clark and Dieter Jaksch. Thanks also to Dieter and Stephen for use of their TEBD code and cluster.

Thanks to my co-authors, both on the publications that are [1–4] and are not [5–8] included in this thesis, as well as others with whom I have discussed these ideas. Of particular influence in shaping the works in this thesis are Felix Binder, Stephen Clark, Dieter Jaksch, Tomi Johnson, Wojciech Kozlowski, Igor Mekhov, and Vlatko Vedral.

I am grateful for the friendship of a number of people: fellow physicists in the department; climbers in OUMC; and my housemates. An honourable mention goes to Benjamin Yadin, who has had the dubious honour and probable misfortune to not

only have shared an office with me during our DPhils, but was also there during our time as undergraduates.

Thanks to my family, especially my parents and brother Ben, for their love and support over the years, both before and during my studies.

A major thanks to Kerry-Anne Kite for innumerable things, not least of which are the support, and the (at least partial) preservation of my sanity, especially given how little I started with...

Thanks also to the institutions who have funded and/or accommodated me at various points throughout my DPhil: the Engineering and Physical Sciences Research Council; the subdepartment of Atomic and Laser Physics, and Lincoln College at the University of Oxford; the Institute for Interdisciplinary Information Sciences at Tsinghua University, and the Centre for Quantum Technologies at the National University of Singapore.

Finally, thank you to anyone and everyone who has taken the time to read this thesis.

Contents

Chapter 1

Introduction

At the start of the 20th century, quantum theory was thrust forth into existence through Planck's energy quantisation, as a solution to the black-body problem [9]. In the years that followed, the theory was expanded and refined into quantum mechanics, perhaps best known as described by Schrödinger [10], Heisenberg [11], and Dirac [12]. Since then, it has become a pillar of our understanding of the natural world, pervading many areas of physics, as a description of matter at the smallest scales in quantum electrodynamics (QED) and chromodynamics (QCD) [13–15], through to ever-increasing scales, as we seek to harness the 'power of quantum' for macroscopic applications, for technologies such as computing, communication, and other information processing [16–19].

At the very heart of quantum theory are a number of fascinating phenomena that cannot be accounted for in classical descriptions of nature, and that are without straightforward classical analogues, not least of which is quantum measurement. Interpretational issues aside, measurement in the quantum regime fundamentally differs from the classical case in a crucial way, through its backaction on a state. A classical measurement, though it can alter our knowledge of the state of a system (e.g. by reducing probabilistic uncertainty), does not directly affect its dynamics (of course, an intrusive measurement device could alter the trajectory taken by the system, but this is not integral to the underlying measurement process). On the other hand, a

quantum measurement will change the dynamics, and an observed system will fundamentally behave differently to one that is left unobserved. It is aspects of this marvel that we will investigate in this thesis.

As noted above, quantum technologies have become an extremely active and fruitful area of research in recent years. Some particularly exciting outcomes of this include (but are not limited to) computers that function on the large-scale entanglement of many atoms or photons [17, 18, 20–22] to allow for the efficient solution to problems that would be intractable on a classical computer, the simulation of quantum systems that would also not be feasible to perform with a classical machine [20, 21, 23–26], the teleportation of quantum states over long distances [16–18, 27], and the prospect of reducing the minimal complexity required of a system to replicate a stochastic process beyond classical limits [28].

As the field grows, there are perhaps two key problems to address: firstly, in which system(s) should such technologies be implemented; and secondly, how can the technologies be implemented within a given choice of system. In this thesis, we shall focus primarily on the latter question, though some of our results and discussion will straddle over to the first question.

Focussing on implementations of quantum technologies using ultracold atomic systems [22, 24], we shall first address the problem of reading out the result of a calculation by a quantum technology. Typical methods for this in cold atom systems require the destruction of the system; this is suboptimal, and we instead explore a non-destructive approach to the problem. We then consider the addition of optical cavities to the system [19, 29–35], and use the new range of dynamical processes and control introduced by this hybrid system [2, 3, 7, 8, 36–51] as a way to enhance the implementation of quantum technologies in such systems. In particular, we make use of the backaction effect that results from quantum measurement as a way to engineer the states and dynamics of the system, in effect 'programming' our technology. Finally, we consider more generally how frequent measurement can be used to steer the

evolution of quantum systems, in a formalism that is independent of the particular underlying system.

As may be evident, there is a common theme running throughout all of this: quantum measurement. We use it both as a tool for determining how a quantum system behaves, and also as a way to control how the system behaves. This interesting synergy underpins the results presented here, which are adaptated from a selection of the papers [1–4] I have researched and written during my time as a DPhil student.

The structure of this thesis is as follows: we first review in Chapter 2 as background the relevant material researched and described by others prior to this work that has relevance to the results later presented. This serves both as a brief introduction/refresher to the concepts, and to establish notation. It covers elementary quantum mechanics, and succint details of quantum information, atoms in optical lattices, and fully-quantum light-matter interactions. Following this, the original research is divided up and presented as four chapters:

- In Chapter 3 we investigate a method of using qubit probes as a way to obtain information about a system. We show how measurements of the qubit state enables one to determine moments of the system operator to which the qubit couples. We propose specifically how this could be implemented with impurity atoms as a way to non-destructively measure ultracold atomic gases, to obtain means, variances and correlations of the gas density. The protocol is demonstrated with a simulated example of the Bose-Hubbard model, for realistic experimental parameters [1].

- Chapter 4 elevates the role of quantum measurement from being simply a tool to read out system properties, to a tool for controlling the system dynamics. It is shown how the introduction of tunable quantised light fields in optical cavities enables a multimode atomic structure to be generated, with non-trivial spatial overlaps. We demonstrate how this allows for the engineering of multiple

classes of states with interesting properties such as multipartite entanglement. Further, the multimode matter structure can be used as part of a protocol to detect and measure entanglement in atomic systems [2].

- Chapter 5 extends the work of the previous chapter, by also including the atomic dynamics induced by the presence of light in the cavities. These dynamics mediate novel processes including long-range density-density interactions and correlated tunnelling events. The application of measurement backaction to these dynamics enables a selective tuning of the processes, allowing for the engineering of Hamiltonians for quantum simulations. Such Hamiltonians are shown to include reservoir models and global dynamical gauge fields [3].

- Chapter 6 investigates a generalisation of quantum Zeno dynamics to the regime where measurements, though still frequent, are now finitely spaced in time (quasi-Zeno). We develop effective Hamiltonians to describe the system evolution in this regime, which exhibit higher-order processes that temporarily vacate the measurement subspace. This formalism is applied to examples of many-body systems, and it is shown that the quasi-Zeno dynamics mediate correlated processes [4].

Finally, we conclude this thesis in Chapter 7, summarising the work, discussing some implications, providing thoughts on the directions that future research building upon these ideas could take, and commenting on experimental progress in the field.

At this point, it is probably prudent to clarify some points on the use in this thesis of units, notation, and linguistics. As is typically the case with theorists for whom the actual numerical value of physical quantities is not the primary concern, we will use natural units, in which the reduced Planck's constant $\hbar = 1$ [14]. While the vast majority of the notation used in this thesis is in keeping with conventional uses of Dirac notation and second quantisation as detailed in Chapter 2, for stylistic

preference (and in keeping with the notation's origins) we forgo the typical practice denoting operators through the use of circumflexes (e.g. $\hat{O}$), instead treating operators and observables synonymously, and with the distinction between operators and eigenvalues hopefully evident from the context. Note also that unless otherwise specified, logarithms log are taken to base 2, while the natural logarithm is written as ln. Spelling is intentionally in keeping with British English, favouring not to Americanise words. The use of the personal pronoun 'we' is present throughout this thesis, and is representative of the collaborative nature of scientific work, and also hopefully makes the text feel more inclusive to the reader. However, the work presented here in this thesis is ultimately my own, formed from my own ideas, from my own calculations, and is as written by me; any errors present are my responsibility.

Chapter 2

Background Material

In this chapter, we provide a brief review of the necessary background material to the research presented in this thesis. This is not intended as a pedagogical treatment, nor is it exhaustive. Rather, it serves to either (depending on the background of the reader) fill in any gaps, or provide a concise refresher in parts of the material. The salient points in each topic are summarised, and references are given to other sources where a more complete treatment can be found. This chapter also establishes the notation used throughout the thesis, clarifies the foundations upon which the original work presented in the remainder of this thesis is built, and enables a clear distinction of what is new.

We begin with the fundamental tenets behind quantum mechanics, and explain how physical quantities are mapped to a mathematical structure in Dirac notation, and it is shown how classical and quantum uncertainty can be expressed in this language. We then review the basics of particle statistics for systems of indistinguishable particles, and the second quantisation formalism in which they can readily be described. An overview of the models of quantum measurements used in this thesis is given, and it is discussed how this can lead to the quantum Zeno effect. We then proceed to review some topics in the field of quantum information relevant to this work, namely, entropy, entanglement and quantum simulations. We also introduce the paradigmatic Bose-Hubbard model, which provides a description of the behaviour

of ultracold atoms in periodic potentials. Finally, we cover descriptions of interactions between light and matter in the fully-quantum regime, and the extension of such models to many-body atomic systems.

2.1 Elementary Quantum Mechanics

2.1.1 Postulates of Quantum Mechanics

There are many different formulations of quantum mechanics and the associated postulates, which are all mathematically equivalent. In this thesis, we shall adopt the Dirac formulation [17, 52–55], and begin with the postulates as stated by Nielsen and Chuang [17]. We assume a basic knowledge of the reader in linear algebra.

The first postulate concerns the description of a quantum state, and how it may be described mathematically:

- A closed physical system is completely described by its state vector, which belongs to a complex vector space, referred to as the state space of the system.

Mathematically, this state space corresponds to a Hilbert space. In Dirac notation, the state vector may be written as an object known as a 'ket' $|\psi\rangle$, which can be some linear combination ('superposition') of basis vectors of the state space $\{|i\rangle\}$:

$$|\psi\rangle = \sum_i c_i |i\rangle, \tag{2.1}$$

where c_i is referred to as the probability amplitude of the state to be in basis state $|i\rangle$. To each ket is designated a corresponding dual vector $\langle\psi|$, referred to as a 'bra', which is defined as $\langle\psi| = \sum_i c_i^* \langle i|$. The corresponding inner product ('bra-ket') of two states $|\psi\rangle$ and (the dual of) $|\phi\rangle = \sum_i c'_i |i\rangle$ is

$$\langle\phi|\psi\rangle = \sum_i c'^*_i c_i, \tag{2.2}$$

where we have used the condition that the basis vectors must be mutually orthonormal; $\langle i|j\rangle = \delta_{ij}$. A physical state vector must satisfy the condition of normalisation, whereby

$$\langle\psi|\psi\rangle = \sum_i |c_i|^2 = 1. \tag{2.3}$$

The extension can be made to cover function spaces, where the basis vectors are described by a function of some continuous variable(s). This leads to the notion of a wavefunction. For such a continuous variable x, this is defined

$$|\psi\rangle = \int dx\psi(x)|x\rangle \tag{2.4}$$

where the wavefuntion $\psi(x) = \langle x|\psi\rangle$. The orthonormality condition is written as $\langle x|x'\rangle = \delta(x - x')$, and the inner product is defined

$$\langle\phi|\psi\rangle = \int dx\langle\phi|x\rangle\langle x|\psi\rangle = \int dx\phi^*(x)\psi(x). \tag{2.5}$$

The second postulate concerns the evolution of a quantum state vector in time:

- The evolution of the states of a closed physical system is given by a unitary transformation U through $|\psi\rangle \to U|\psi\rangle$. The continuous time evolution of such a system is given by the Schrödinger equation

$$i\frac{d|\psi\rangle}{dt} = H|\psi\rangle, \tag{2.6}$$

  where H is a Hermitian operator called the Hamiltonian of the system.

The unitary transformation governing the evolution of the state between times t_1 and t_2 is thus represented by a unitary operator

$$U(t_1, t_2) = e^{-iH(t_2-t_1)}. \tag{2.7}$$

It transpires that the Hamiltonian corresponds to an operator defined by the energy levels of the system. As H is a Hermitian operator, we can express it in a basis in which it is diagonal:

$$H = \sum_i E_i|E_i\rangle\langle E_i|. \tag{2.8}$$

The eigenvectors of this operator $|E_i\rangle$ (referred to as energy eigenstates or 'stationary states') are the states in which the energy of the system is well-defined, and the corresponding energies of these states are given by the eigenvalue E_i. The lowest energy state is called the ground state of the system. The Hamiltonian is thus intimately dependent on the system under consideration.

The third postulate concerns the measurement of a quantum system, when another external system interacts with our previously closed system:

- A collection of measurement operators $\{M_m\}$ acting on the state space of the system describe the act of quantum measurement, where m describes the possible measurement outcomes. The probability of obtaining outcome m for state $|\psi\rangle$ is given by $P(m) = \langle\psi|M_m^\dagger M_m|\psi\rangle$, and the resulting state transformation is $|\psi\rangle \to M_m|\psi\rangle/\sqrt{P(m)}$.

The measurement operators must satisfy the completeness relation $\sum_m M_m^\dagger M_m = \mathbb{I}$ such that the probabilities are normalised; $\sum_m P(m) = 1$. We note also that the measurement outcome (and hence any physically observable effect) is independent of any global phase of the state $\exp(i\varphi)|\psi\rangle$, and so such global phases may effectively be ignored.

A set of special cases of quantum measurement are projective measurements. We shall discuss these in more detail below, but for now we note that for such measurements we replace the M_m with projection operators ('projectors') $\mathcal{P}_m$ which in addition to the completeness relation are also idempotent and mutually orthogonal;

$$\mathcal{P}_m\mathcal{P}_n = \mathcal{P}_m\delta_{mn}. \tag{2.9}$$

This allows us to define the notion of an observable, which is a physical quantity of the system that may be measured. We can express the operator associated with an observable using these projectors:

$$Q = \sum_m q_m\mathcal{P}_m, \tag{2.10}$$

where q_m are the measurable outcome values for the observable, and $\mathcal{P}_m$ define the corresponding subspace of states with this outcome. Thus, the Hamiltonian is the operator associated with the energy observable. This procedure of converting observables into operators is called first quantisation.

For two arbitrary Hermitian operators Q_1 and Q_2, if their commutator $[Q_1, Q_2] \equiv Q_1Q_2 - Q_2Q_1$ is equal to zero, there is a basis ('representation') in which they are mutually diagonal, this basis defined by a set of mutual eigenvectors that they share. In the case of quantum mechanics, two commuting operators share a complete set of mutual eigenstates, and conversely, two non-commuting observables do not share such a complete set of mutual eigenstates. This has the consequence that if two observables do not have commuting operators, it is not possible to define a complete set of states with a definite value for both observables simultaneously.

An example of two such observables are position $\boldsymbol{x}$ and momentum $\boldsymbol{p}$. The associated operators can be written (in the basis of position eigenstates)

$$\boldsymbol{x} = \int d\boldsymbol{r}\boldsymbol{x}|\boldsymbol{x}\rangle\langle\boldsymbol{x}| \tag{2.11}$$

and

$$\boldsymbol{p} = -i\nabla. \tag{2.12}$$

From this, we can see that $[\boldsymbol{x}_i, \boldsymbol{p}_j] = i\delta_{ij}$, and thus one cannot simultaneously know the values of position and momentum in a given direction of a system. We can also use this to write the eigenstates of momentum in the position representation, which are (up to normalisation)

$$\psi_{\boldsymbol{p}}(\boldsymbol{x}) = e^{i\boldsymbol{p}.\boldsymbol{x}}. \tag{2.13}$$

We note that the above formalism is considered in what is referred to as the 'Schrödinger picture', where it is the states that evolve in time. There is an equivalent formalism, the 'Heisenberg picture', in which it is instead the operators that evolve

in time. By considering the change in operator elements under the above unitary transformations $\langle i|Q|j\rangle \rightarrow \langle i|U^\dagger QU|j\rangle$, in the Heisenberg picture the operators evolve

$$Q \rightarrow U^\dagger QU. \tag{2.14}$$

The corresponding continuous time evolution is described by the Heisenberg equation:

$$i\frac{dQ}{dt} = [Q, H]. \tag{2.15}$$

A hybrid of the two, the 'interaction picture', has time dependence in both the states and the observables, determined by a particular choice in the separation of the Hamiltonian.

The fourth, and final postulate concerns the description of composite systems:

- The state space of a composite physical system is given by the tensor product of the state spaces of the component systems, and the corresponding state vectors are formed in the same such manner.

There are multiple notations to represent this product space of two systems A and B. The first is straightforwardly with tensor product symbols; $|A\rangle \otimes |B\rangle$, but more efficiently, the product can be taken to be implicit, and the full system written as $|A\rangle|B\rangle$, or even $|A, B\rangle$. We note also that in general it is not possible to always write a state in this product form, but instead a sum over such products is required. This is called entanglement, and we will discuss this in more detail below.

Although not a postulate, it is also desirable to have a way of reintroducing classical probabilities into the formalism. Density operators provide such a method. They also provide a convenient tool for describing subsystems of larger, composite systems. Physically, density operators can arise from either classical uncertainty in a single quantum state, or from a statistical ensemble of multiple quantum states; both situations may be described in a mathematically equivalent manner. The density operator

is defined thus: given a system that has probabilities $\{P_i\}$ of being in quantum states $\{|\psi_i\rangle\}$, the associated density operator ρ describing the system is

$$\rho = \sum_i P_i |\psi_i\rangle\langle\psi_i|. \tag{2.16}$$

The states considered thus far are a special case of this, where one of the P_i is equal to one, and the rest are zero. Such states are called pure states, while the more general case are referred to as mixed states. The above formalism for pure states can be generalised to the mixed state case.

The evolution of a density operator under unitary transformation U is given by

$$\rho \to U\rho U^\dagger, \tag{2.17}$$

and the associated continuous time evolution equation is

$$i\frac{d\rho}{dt} = [H, \rho]. \tag{2.18}$$

Similarly, the action of a measurement can be generalised to density operators; the probability of measurement outcome m is given by

$$P(m) = \mathrm{Tr}(M_m^\dagger M_m \rho), \tag{2.19}$$

and has the associated action $\rho \to M_m \rho M_m^\dagger / P(m)$. The measurement operators must still satisfy the completeness relation $\sum_m M_m^\dagger M_m = \mathbb{I}$ from the pure state case.

There are certain properties that a density operator must satisfy in order to be a valid state. The first is that it must be Hermitian, which follows straightforwardly from the definition. The second is that it must have unit trace, which is equivalent to the normalisation condition for pure states, as it enforces that the total probability is one. The third is that it must be a positive operator, in order that we have $0 \leq P_i \leq 1$ for all the probabilities, in all possible choices of basis.

There is a straightforward method to check whether a given density operator corresponds to a pure or mixed state. Consider the trace of ρ^2. This quantity is

called the purity of the state, as it is equal to one for a pure state, and lies between zero and one for a mixed state.

The utility of the density operator formalism becomes most apparent when one asks about the behaviour of a component subsystem of the full system. Suppose we have some composite system that can be split into two parts A and B. The state ρ_{AB} of the composite system can be used to extract the reduced density operator that describes the state of one of the subsystems. This is done through the partial trace operation, where the trace is performed only on the parts of the tensor product corresponding to the other subsystem(s):

$$\rho_A = \mathrm{Tr}_B(\rho_{AB}). \tag{2.20}$$

2.1.2 Many-Body Systems and Quantum Statistics

We now turn to the case of many-particle systems. As noted above, such systems can be constructed by taking a tensor product of the state spaces of each of the individual particles. However, such a treatment is unfavourable, as it becomes very cumbersome to describe large systems, particularly those with varying numbers of particles; we must define a 'vacuum' state for each possible particle to represent its non-existence, and the composite state space must be made of an infinite (or at least, the maximum possible number of particles) product of the individual particle state spaces.

Another downside to the first quantised notation is that it does not inherently contain any symmetries possessed by indistinguishable particles, and so such symmetries must be added ad hoc. When two particles are identical, then their exchange should not have an observable effect on their state, and leaves only the freedom to add a global phase $|\psi\rangle \to \exp(i\varphi)|\psi\rangle$ [56]. This can be divided up into three cases; bosons ($\varphi = 0$), fermions ($\varphi = \pi$) and anyons ($\varphi \neq 0, \pi$). These phase factors are called the quantum statistics of the particles [57–60], and bosonic and fermionic statistics may be found in the fundamental particles of nature (e.g. electrons and quarks are

fermions, while photons, gluons, and the weak force carriers W and Z are bosons). Anyonic statistics arise as emergent phenomena [60], and will not be discussed here. Indeed, we shall focus on bosonic particles in this thesis.

A consequence of this symmetry is that a state of indistinguishable bosons must be identical under the exchange of any two such particles. For this reason, and as a resolution to the above problem of varying particle numbers, we can, instead of working in a Hilbert space consider a Fock space, in which the symmetrisation is inherent. Fock space states, instead of describing the state occupied by the individual particles, describe the number of particles in each mode; that is, the number of bosons in the system of a given species that are in a particular state.

The Fock state with requisite symmetrisation can be found by applying a sum over permutations of the state. For a Hilbert space state

$$|\Psi_{\text{Hilbert}}\rangle = |\psi_1, \ldots, \psi_N\rangle, \tag{2.21}$$

the corresponding Fock state is given by

$$|\Psi_{\text{Fock}}\rangle \equiv |n_1, \ldots, n_M\rangle = \frac{1}{\sqrt{N!}} \sum_{\mathfrak{P}} \mathfrak{P} |\Psi_{\text{Hilbert}}\rangle, \tag{2.22}$$

where n_i are the occupation numbers for modes i, and the operators $\{\mathfrak{P}\}$ permute the single-particle states. Fock states with different occupation numbers are orthogonal:

$$\langle m_1, \ldots, m_M | n_1, \ldots, n_M \rangle = \prod_{i=1}^{M} \delta_{m_i n_i}. \tag{2.23}$$

We can define a set of operators $\{b^\dagger, b\}$, the creation and annihilation operators, which create or destroy particles occupying their associated mode respectively, while preserving the exchange symmetry. For bosonic modes, the action of these operators is

$$b_i^\dagger |n_1, \ldots, n_i, \ldots, n_M\rangle = \sqrt{n_i + 1} |n_1, \ldots, n_i + 1, \ldots, n_M\rangle, \tag{2.24a}$$

$$b_i |n_1, \ldots, n_i, \ldots, n_M\rangle = \sqrt{n_i} |n_1, \ldots, n_i - 1, \ldots, n_M\rangle. \tag{2.24b}$$

The operators obey the commutation relations

$$[b_i, b_j] = [b_i^\dagger, b_j^\dagger] = 0, \tag{2.25a}$$

$$[b_i, b_j^\dagger] = \delta_{ij}. \tag{2.25b}$$

The vacuum state $|0\rangle$ is defined as that in which all the modes are unoccupied. Any basis state of the Fock space can be obtained by application of creation operators on this vacuum state

$$|n_1, \ldots, n_M\rangle = \prod_{i=1}^{M} \frac{1}{\sqrt{n_i!}} b_i^{\dagger n_i} |0\rangle. \tag{2.26}$$

We note that we shall use the convention that b_i are used for matter bosons, and a_j for light bosons. Quantum states can now in this formalism essentially be written in terms of the operators that create them. This promotion of states to operators is called second quantisation. More generally, single-particle states can be created in any basis by an appropriate creation operator, formed from linear combinations of creation operators in our preferred basis.

We can also define number operators $N_i = b_i^\dagger b_i$, for which the Fock space basis states are eigenstates:

$$N_i |n_1, \ldots, n_i, \ldots, n_M\rangle = n_i |n_1, \ldots, n_i, \ldots, n_M\rangle, \tag{2.27}$$

with the total number of particles given by the total number operator $N = \sum_i N_i$.

A state of particular note is the coherent state $|\beta\rangle$, defined as the eigenstate of the annihilation operator with eigenvalue β: $b|\beta\rangle = \beta|\beta\rangle$ [61]. This state takes the form

$$|\beta\rangle = e^{-|\beta|^2/2} \sum_n \frac{\beta^n}{\sqrt{n!}} |n\rangle. \tag{2.28}$$

Operators can be re-expressed in terms of Fock space states; a single-particle operator s in Hilbert space becomes

$$S = \sum_{i,j} \langle \psi_i | s | \psi_j \rangle b_i^\dagger b_j, \tag{2.29}$$

while a two-particle Hilbert space operator t becomes

$$T = \sum_{i,j,k,l} \langle\psi_i|\langle\psi_j|t|\psi_k\rangle|\psi_l\rangle b_i^\dagger b_j^\dagger b_k b_l. \tag{2.30}$$

We will make extensive use of this formalism in this thesis, as many examples of the systems we consider are formed of indistiguishable particles.

2.1.3 Quantum Measurement and the Quantum Zeno Effect

The measurements we will consider in this thesis will predominantly be projective measurements. As noted above, to each observable is associated an operator of the form $Q = \sum_m q_m \mathcal{P}_m$. When q_m is non-degenerate, each projector can be written as the outer product of the corresponding eigenstate $\mathcal{P}_m = |q_m\rangle\langle q_m|$, while for degenerate eigenvalues these projectors cover the whole of the degenerate subspace spanned by the eigenstates corresponding to this eigenvalue.

The action of the measurement, following the above prescription in the postulate, is to then project the state into the corresponding eigenstate or eigenspace of the observable; with probability

$$P(m) = \mathrm{Tr}(\mathcal{P}_m \rho), \tag{2.31}$$

we measure outcome m with measurement value q_m, and the state is transformed

$$\rho \to \frac{\mathcal{P}_m \rho \mathcal{P}_m}{P(m)}. \tag{2.32}$$

We will also briefly consider measurement according to the quantum jump formalism [62]. In this formalism, the system is allowed to interact with an environment, and this environment can detect certain processes of the system, e.g. the emission of a photon. When this occurs, there is a backaction on the system described by a 'jump' operator, while in periods of non-detection, the system evolves under a non-Hermitian Hamiltonian which suppresses states that should probabilistically trigger more detection events (as non-detection is also effectively a form of measurement).

We will not give a more complete description of this formalism in general, and instead introduce the relevant properties to our study when necessary.

Returning to the case of projective measurements, a rather curious phenomenon can occur when a system is continuously measured. Suppose we have a system and an associated observable with non-degenerate eigenvalues. When the system is measured, it is projected into the corresponding eigenstate; $\rho \to \mathcal{P}_m \rho \mathcal{P}_m / P(m)$. In the subsequent time δt, the system then undergoes unitary evolution $U = \exp(-iH\delta t) \approx 1 - iH\delta t + \mathcal{O}(\delta t^2)$. Supposing we make a further measurement at δt, the probability of obtaining the same outcome is given by

$$P(m|m) = \frac{1}{P(m)} \mathrm{Tr}(\mathcal{P}_m U \mathcal{P}_m \rho \mathcal{P}_m U^\dagger) \approx 1 + \mathcal{O}(\delta t^2). \tag{2.33}$$

Thus, in the limit $\delta t \to 0$, the probability that the system will transition out of the state tends towards zero, and hence the system is frozen into this state. This is called the quantum Zeno effect (QZE) [63–65].

Considering instead the case where the measurement eigenvalues are degenerate, a similar effect occurs, quantum Zeno dynamics (QZD) [66–68]. An analogous analysis shows that the system evolution is again frozen, but only partially, into the subspace spanned by the measured eigenvalue. We can determine the effective evolution of the system within this subspace by considering the evolution after N such measurements in some time $\tau = N\delta t$, and taking the limit $\delta t \to 0$ ($N \to \infty$), while τ is held constant:

$$\lim_{N\to\infty} (\mathcal{P}_m U \mathcal{P}_m)^N \approx \lim_{N\to\infty} \left(\mathcal{P}_m \left(1 - iH\frac{\tau}{N} + \mathcal{O}(\delta t^2) \right) \mathcal{P}_m \right)^N = e^{-iH_Z \tau}, \tag{2.34}$$

where we have defined the Zeno Hamiltonian

$$H_Z = \mathcal{P}_m H \mathcal{P}_m. \tag{2.35}$$

This result will play a major role in parts of this thesis, as it demonstrates a very clear path for the use of measurement to control the evolution of a system. Similar

evolutions, in which a system is confined to evolve within a particular subspace, may also be physically manifest by other means. Strong decoherence can induce such evolution (as the environment is essentially performing a measurement of the system state [19]), as can energetic confinement by adiabatic evolution [66, 68].

2.2 Quantum Information

Quantum information is a field that has come to the forefront of research in recent years. It generalises the concepts of classical information to quantum systems, and provides a framework for describing the operation of quantum technologies. We will provide an overview of some of the topics in this field that are relevant to the work in this thesis.

2.2.1 Bits, Qubits, and Quantum Circuits

In the classical world, information can be represented by a series of 'bits', two-state systems that are typically labelled by 0 and 1 [16–18]. Multiple such bits can be combined together as bit strings, such as 1001110 or 1011011, into which can be encoded messages. As a simple example, one bit can be used to encode a simple `YES`/`NO` message, with the mapping `NO`$\rightarrow 0$ and `YES`$\rightarrow 1$. In this picture, the bit forms the fundamental unit of information, in units also called bits. Since a string of N bits has 2^N possible states, it can encode up to 2^N different messages. Correspondingly, a system with M possible states can be used to encode $\log M$ bits of information.

In the quantum case, a similar scenario can be considered, where a quantum bit, or 'qubit' is formed from a two-state quantum system [16–18]. The crucial difference between this and the classical case is the possibility for qubits to exist in superpositions of the states $c_0|0\rangle + c_1|1\rangle$. Thus, one can encode into a quantum state a superposition of different messages. As with the classical case, a system with M states can encode $\log M$ bits of information. One may be misled into thinking that because a two-dimensional quantum state has infinite degrees of freedom in its specification (the

relative size and phase of the amplitudes between two basis states) that an infinite amount of information may be encoded; such reasoning is incorrect, as the states are not orthogonal, and hence cannot correspond to *distinct* messages (this corresponds to the lack of perfect distinguishability for non-orthogonal quantum states).

A useful set of operators to use when working with qubits are the Pauli matrices [54, 55]. These matrices, labelled X, Y and Z, can be used to describe three bases that each have equal overlap with the basis states of the other two. These matrices are:

$$\sigma^X = \begin{pmatrix} 0 & 1 \\ 1 & 0 \end{pmatrix}; \tag{2.36a}$$

$$\sigma^Y = \begin{pmatrix} 0 & -i \\ i & 0 \end{pmatrix}; \tag{2.36b}$$

$$\sigma^Z = \begin{pmatrix} 1 & 0 \\ 0 & -1 \end{pmatrix}. \tag{2.36c}$$

Devices that processes these qubits are called quantum computers [17,18]. We will employ a particular model of such devices, known as circuit-based quantum computing. In this model, a quantum computer takes an input state, acts on it with a set of unitary operations (also referred to as 'gates'), and outputs a different quantum state. This can be represented pictorially by a quantum circuit, as described in Fig. 2.1(a). These quantum circuits are analogous to logic circuits, with time running from left to right.

A special case of these quantum circuits, which we will make use of, is where we can consider the system split into two components, the 'main' system, and a 'control' qubit [Fig. 2.1(b)]. Gates are performed on the main system, conditional on the state of the qubit. This allows interferometric protocols to be run on the system, and a measurement of the final state of the qubit allows information about the system to then be extracted. We will later discuss specific examples of this, to determine properties such as entanglement of the system state.

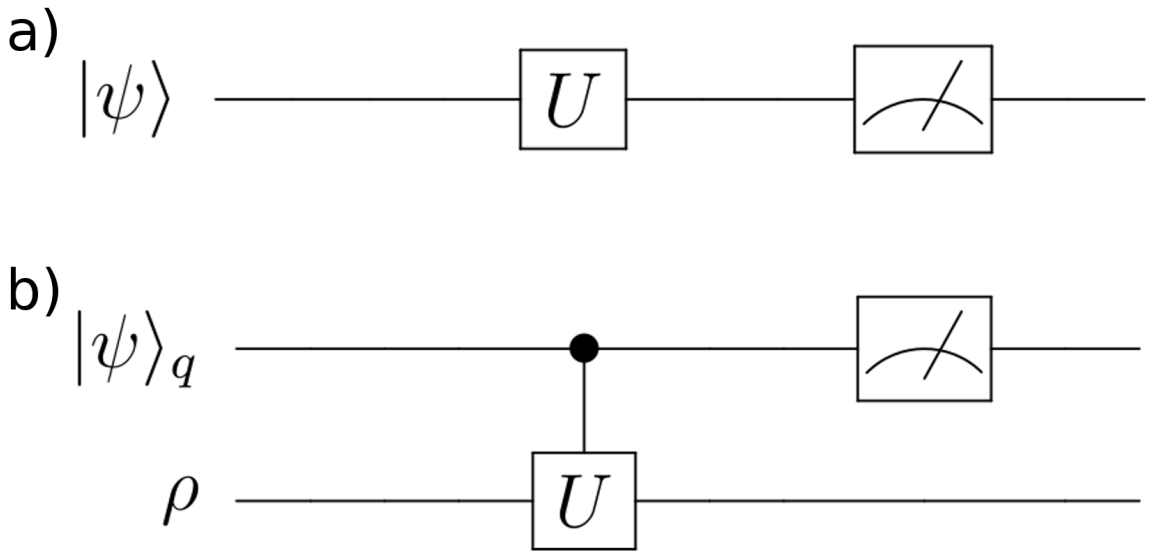

Figure 2.1: **Circuit-based model of quantum computing.** (a) A quantum circuit pictorially represents a model of quantum computation. Here, an input state $|\psi\rangle$ is acted on by a gate U, and then measured (time runs sequentially left to right). (b) A particular class of circuits use a control qubit, with operations performed on the rest of the state conditional on the control state (open circle $\circ$ for $|0\rangle$, solid circle $\bullet$ for $|1\rangle$). Measurement is then performed on the control qubit.

2.2.2 Quantum Simulation

Due to the exponential scaling of the state space of a quantum system with the number of constituent subsystems (e.g. the 2^N possible states of an N qubit system), it is in general very difficult to use a classical computer to calculate the behaviour of a quantum system of more than a few particles (current supercomputers are able to describe the behaviour of approximately 40 qubits [69]). However, it has been pointed out that a universal quantum computer (that is, one in which any gate can be performed at any time) would be able to emulate the behaviour of any quantum system [20, 21, 23]. Moreover, as the state space of the universal quantum computer also scales exponentially with the number of resources, larger systems can be managed with an efficient scaling of the computer size. Such devices are referred to as quantum simulators [24–26, 70].

However, the construction of a universal quantum computer of a size large enough

to outperform a classical computer for such calculations is so far non-existent, and is the long-term goal of much current research. In the meantime, as a stopgap, one can instead consider purpose-built quantum simulators, designed to compute the physics of a particular system, or set of systems. A class of such devices are analogue quantum simulators, where the device is engineered to have a Hamiltonian equivalent to that of the system being simulated [26].

The use of such analogue quantum simulators is that they aim to behave in an identical way to the system under consideration (or an idealised model thereof), and thus their output is intended to be a state identical to that of the simulated system (the verification of the output of quantum simulators and computers forms a current line of research [70, 71]). The simulators have the advantage that they are designed with controllability in mind, and so are typically easier to measure than their original counterparts, and often allow for the variation of parameters in a manner that would not be easily (if at all) tunable in the original system. They can also be used to simulate exotic systems that, though mathematically well-defined, may not be known to occur naturally. Analogue quantum systems have famously been successfully used to simulate Hubbard models [26, 72, 73], as well as other phenomena such as magnetic monopoles [74], artificial gauge fields [75–86], and the Dicke model [87]. We shall later discuss how measurement can be used as a method to engineer the dynamics of such devices.

2.2.3 Entropy and Entanglement

In thermodynamics, entropy is used as a measure of 'disorder' in a system, and the more degrees of freedom a system has (or rather, the more accessible states it has), the higher the entropy [56]. This concept was generalised by Shannon to also find application in information theory [88]. The Shannon entropy parameterises the uncertainty in a classical probability distribution: for a system that can be found in

a classical state $|i\rangle$ with probability P_i, the Shannon entropy is given by

$$H(\rho) = -\sum_i P_i \log(P_i). \tag{2.37}$$

This can be generalised to the quantum regime, and the von Neumann entropy [64] of a quantum state ρ is defined

$$S(\rho) = -\mathrm{Tr}(\rho \log(\rho)). \tag{2.38}$$

When the density matrix is written in its diagonal form, with diagonal elements P_i, this expression becomes identical to the Shannon entropy. It is zero for a pure state, and for a maximally-mixed state of dimension D takes its maximum value $\log(D)$. Thus, for an N qubit state, the maximum possible entropy is $S = N$.

One of the much vaunted phenomena that can result from quantum mechanics is entanglement [89, 90]. Entanglement is a type of correlation that does not exist in the classical world. It is often classified by a definition of what is not an entangled state. A separable state of two subsystems A and B is one which can be written

$$\rho_{\mathrm{Sep}} = \sum_i P_i \rho_i^{(A)} \otimes \rho_i^{(B)}. \tag{2.39}$$

For this state, correlations between the subsystems appear only because of classical uncertainties. States which cannot be written in a separable form are defined as entangled states. Such states must therefore possess correlations between the subsystems that can only occur from a quantum mechanical description. Multipartite entanglement refers to situations where there is entanglement between more than two subsystems, and genuine multipartite entanglement is when all possible bipartitionings of a state into subsystems show entanglement.

A quintessential example of entangled states are the Bell states, describing two qubit systems. These are defined

$$\begin{aligned} |\Phi^{\pm}\rangle &= \frac{1}{\sqrt{2}}(|01\rangle \pm |10\rangle) \\ |\Psi^{\pm}\rangle &= \frac{1}{\sqrt{2}}(|00\rangle \pm |11\rangle). \end{aligned} \tag{2.40}$$

There is no definitive, efficient method to determine whether or not a quantum state is entangled. However, there are certain methods one can use as aids to help discriminate between separable and entangled states. One set of such tools are entanglement witnesses, observables for which one can apply a constraint that must be satisfied by the expectation value of the observable for a separable state. States violating this constraint must then therefore be entangled. This provides a sufficient, but not necessary criterion for determining whether a state is entangled.

For pure states, there is a definitive method however. As noted above, a pure state has zero von Neumann entropy. However, considering the von Neumann entropy of the reduced states of the subsystems, if the system is entangled, we find that this is non-zero. Thus, for pure states, if $S(\rho_A) = S(\rho_B) > 0$, the state is entangled (equivalently, if $\mathrm{Tr}(\rho_A^2) \neq 1$, the state is entangled). Even if the overall state is mixed, any state for which $\mathrm{Tr}(\rho_{A,B}^2) < \mathrm{Tr}(\rho_{AB}^2)$ is entangled (though the converse is not true) [91].

This leads to a measure of entanglement for pure states, called the entanglement entropy [90]. The entanglement entropy is defined as the von Neumann entropy Eq. (2.38) of the reduced density matrix of one of the subsystems:

$$E(\rho_{AB}) = S(\rho_A) = S(\rho_B). \tag{2.41}$$

Thus, we see that the Bell states are all 'maximally entangled' states, as they have $E = 1$, the maximum possible value for two-state subsystems.

For mixed states, there is no general expression for parameterising the amount of entanglement that is efficiently computable. However, there are measures which are typically used, one of which is the logarithmic negativity [92]. This is defined as the logarithm of the trace norm of the state after a partial transpose in one of the subsystems. This is equivalent to

$$E_N = \log(2\mathfrak{N} + 1), \tag{2.42}$$

where the negativity $\mathfrak{N} = \sum_i (|\lambda_i| - \lambda_i)/2$, and λ_i are the eigenvalues of $\rho_{AB}^{T_A}$. The logarithmic negativity is greater than zero only if the state is entangled, so forms a sufficient criterion for determining entanglement. However, some entangled states have zero negativity, and so it is not a necessary condition.

2.3 Bose-Hubbard Model

2.3.1 Physical Motivation

Perhaps the most prolific examples of systems which are studied with quantum simulations are Hubbard models and their variants. These are based around tight-binding models, which describe the behaviour of particles in a lattice structure moving between neighbouring sites. The most straightforward extension to this is the inclusion of interactions between particles occupying the same site. These two processes are the principal components of Hubbard models. The original Hubbard Hamiltonian describes fermionic particles [93], and was proposed as a model of electrons moving in a crystal lattice.

Here we shall focus on the bosonic variant, the Bose-Hubbard Hamiltonian [26,72]. This Hamiltonian forms the basis of descriptions of the behaviour of ultracold atoms in optical lattices. This model has a rich phase behaviour, which has been subject to intense theoretical study, and verified experimentally, providing one of the first realisations of a quantum simulator [73]. It has been extended in a multitude of ways beyond the base model, to include phenomena such as next-nearest neighbour interactions, long-range dipolar interactions, density-dependent tunnelling, disorder, and interactions with external fields [26,94]. We will later consider an example of the latter, when optical cavities are introduced to the system [29,31].

2.3.2 Derivation and Properties of the Bose-Hubbard Hamiltonian

An optical lattice is formed by interfering two counter-propagating beams in each dimension of the lattice. The wavelength of the laser determines the lattice spacing, which is given by $\lambda/2$. The laser light then traps neutral atoms in the minima of a periodic potential due to the Stark shift (the deformation of the energy levels in an atom by an external electric field [95, 96]). The depth of the wells in this lattice structure can be varied by the laser intensity; the stronger the laser, the deeper the potential, and hence the more localised the atoms become [72, 97, 98].

In such a system, the atoms are described by the Hamiltonian

$$H = \int d\boldsymbol{r}\psi^\dagger(\boldsymbol{r})\left(-\frac{\nabla^2}{2m} + V_T(\boldsymbol{r})\right)\psi(\boldsymbol{r}) + \frac{2\pi a_s}{m}\int d\boldsymbol{r}\psi^\dagger(\boldsymbol{r})\psi^\dagger(\boldsymbol{r})\psi(\boldsymbol{r})\psi(\boldsymbol{r}), \quad (2.43)$$

where m is the mass of the atom, $V_T(\boldsymbol{r})$ is the trapping potential, and a_s is the atomic s-wave scattering length, mediating atomic contact interactions. Thus, the first term governs the kinetic energy, while the second describes atom-atom interactions. We assume the atoms to be sufficiently cooled that their energies are low enough to approximate that they occupy the lowest energy band, and we can expand the atomic state in terms of a basis of states localised to each site [72]. An appropriate basis of states describing atoms localised at each site are Wannier functions $w(\boldsymbol{r})$ [99]. In this basis, we can expand the state $\psi(\boldsymbol{r})$ as

$$\psi(\boldsymbol{r}) = \sum_j w(\boldsymbol{r} - \boldsymbol{r}_j)b_j, \quad (2.44)$$

where b_j is the annihilation operator for an atom at lattice site j, which is located at $\boldsymbol{r}_j$. Inserting this into the Hamiltonian, we obtain

$$H = -\sum_{ij} J_{ij}b_i^\dagger b_j + \sum_{ijkl} U_{ijkl}b_i^\dagger b_j^\dagger b_k b_l, \quad (2.45)$$

where

$$J_{ij} = -\int d\boldsymbol{r}w(\boldsymbol{r} - \boldsymbol{r}_i)\left(-\frac{\nabla^2}{2m} + V_T(\boldsymbol{r})\right)w(\boldsymbol{r} - \boldsymbol{r}_j) \quad (2.46a)$$

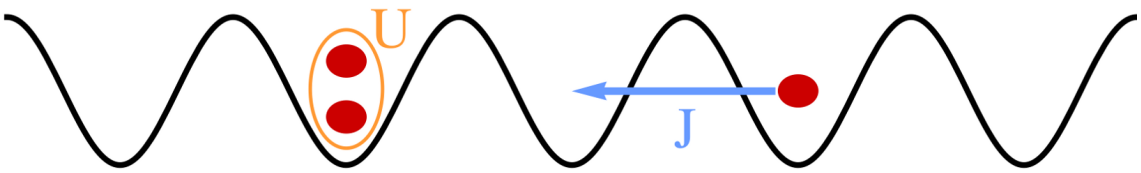

Figure 2.2: **Illustration of processes in the Bose-Hubbard Hamiltonian.** The tunnelling between nearest-neighbour sites is parameterised by a rate J, while there is an energy penalty U for multiple occupancy of sites due to repulsive contact interactions between the atoms.

and

$$U_{ijkl} = \frac{4\pi a_s}{m} \int d\boldsymbol{r} w(\boldsymbol{r} - \boldsymbol{r}_i) w(\boldsymbol{r} - \boldsymbol{r}_j) w(\boldsymbol{r} - \boldsymbol{r}_k) w(\boldsymbol{r} - \boldsymbol{r}_l). \tag{2.46b}$$

Thus, J_{ij} parameterises the motion of atoms between lattice sites, due to atomic tunnelling (or 'hopping'), while U_{ijkl} corresponds to the atom-atom repulsion. Typically, it is approximated that the Wannier functions are well-localised, such that only the dominant terms are kept, corresponding to nearest-neighbour tunnelling $J = J_{<ij>}$ ($< ij >$ denoting that i and j are nearest-neighbour sites) and on-site repulsion $U = U_{iiii}$ [Fig. 2.2]. In this approximation, we obtain the Bose-Hubbard Hamiltonian

$$H_{\mathrm{BHM}} = -J \sum_{<ij>} b_i^\dagger b_j + \frac{U}{2} \sum_i b_i^\dagger b_i^\dagger b_i b_i. \tag{2.47}$$

The neglected terms correspond to longer-range hopping (which are suppressed and hence occur much less frequently than the nearest-neighbour tunnelling events), and repulsion between atoms localised to different sites, such as nearest-neighbour density-density interactions, and density-dependent tunnelling. One may also consider the effects of an additional inhomogeneity in the trapping potential, by including chemical potential terms $\sum_j \epsilon_j b_j^\dagger b_j$, where the ϵ_j are the energy offsets for each site. As noted above, by including the effects of external fields, yet more phenomena can be incorporated.

Depending on the relative values of J and U, and the filling factor of the lattice ν, the system will exhibit drastically different behaviour [26, 72, 73, 100, 101]. At

small $U/J \ll 1$, the dynamics is dominated by the atomic tunnelling, and atoms are delocalised across the whole lattice. This is called the superfluid regime, and the ground state is composed of all atoms in the zero-momentum state, with phase coherence between all atoms. In contrast, at large $U/J \gg 1$, the on-site repulsion is the dominant effect, and at integer-filling the ground state of the system is the Mott insulating state, where atoms are highly localised, and each site contains ν atoms. There is an energy gap U between this ground state and the first excited state, where an atom moves to a neighbouring site leading to a population imbalance. Varying across the parameter range, there is a phase transition between these two regimes, with the exact transition point depending on the filling factor, the dimension, and the co-ordination number (the number of nearest-neighbour sites to each lattice site) of the lattice (for unit filling factor $\nu = 1$ in one-dimension, the critical value is found to be $(U/J)_c \approx 3.37$) [100, 101]. For non-integer filling at large U/J, a superfluid is formed on top of an insulating background of floor(ν) atoms per site.

2.3.3 Spin Systems

As a brief interlude, let us also discuss another common type of many-body system that we shall consider later in this thesis: spin systems. Physically, the spin of a system corresponds to an inherent angular momentum it possesses, not due to any form of orbital motion. More abstractly, we can consider spin as a mathematical concept describing a set of operators and states linked together by a particular relation [55].

A spin system has a total spin value s, which can take any positive integer or half-integer value. Associated with each spin is a vector operator $\boldsymbol{S}$, for which all states corresponding to the total spin value are eigenstates of the corresponding operator $\boldsymbol{S}^2$, with corresponding eigenvalues $s(s+1)$. The vector operator $\boldsymbol{S}$ has three components, which may be labelled as S^X, S^Y and S^Z. These operators mutually satisfy the commutation relation $[S^i, S^j] = i\epsilon_{ijk}S^k$. These operators have eigenstates which may

take eigenvalues in integer steps from $-s$ up to s. A common choice of basis is that of S^Z, in which we label the eigenvalues as m_s.

Consider the S^Z eigenstate $|s, m_s\rangle$, defined such that

$$\boldsymbol{S}^2|s, m_s\rangle = s(s+1)|s, m_s\rangle \tag{2.48a}$$

and

$$S^Z|s, m_s\rangle = m_s|s, m_s\rangle. \tag{2.48b}$$

Using the commutation relations, one can derive straightforwardly that

$$S^Z(S^X \pm iS^Y)|s, m_s\rangle = (m_s \pm 1)(S^X \pm iS^Y)|s, m_s\rangle. \tag{2.49}$$

Thus, the action of $S^X \pm iS^Y$ is to raise (lower) an S^Z eigenstate to the corresponding eigenstate with ± 1 eigenvalue. We thus label these operators as the spin raising (lowering) operators, denoted $S^\pm = S^X \pm iS^Y$. By also taking into consideration the maximum- and minimum-allowed S^Z eigenvalues, from a more detailed analysis it can be deduced that

$$S^\pm|s, m_s\rangle = \sqrt{s(s+1) - m_s(m_s \pm 1)}|s, m_s \pm 1\rangle. \tag{2.50}$$

The Pauli matrices Eqs. (2.36) are an appropriate set of operators to describe the first non-trivial spin, $s = 1/2$, when appended with a pre-factor of $1/2$.

Arrays of these spins can be put together to form many-body systems. Commonly-studied examples of this are spin chains [102]. Spin chains are one-dimensional arrays of spins, typically with nearest-neighbour interactions. Such Hamiltonians take the form

$$H_{\mathrm{SC}} = \sum_j (J_j^X S_j^X S_{j+1}^X + J_j^Y S_j^Y S_{j+1}^Y + J_j^Z S_j^Z S_{j+1}^Z + \boldsymbol{B}_j.\boldsymbol{S}_j), \tag{2.51}$$

and are known as Heisenberg models. The first set of terms describe the interaction between spins, while the last term describes biases due to effects such as external fields and anisotropies. A special case of this is the Heisenberg XXZ model, where $J_j^X = J_j^Y = J_{\mathrm{ex}}$. In this case, the S^X and S^Y terms can be gathered together, and rewritten as $J_{\mathrm{ex}}(S_j^+ S_{j+1}^- + S_j^- S_{j+1}^+)$, and thus mediate the transfer of spin quanta across neighbouring sites. This is referred to as an exchange interaction [103, 104].

2.4 Light-Matter Interactions

We will now review the treatment of interactions between light and matter. We will start by describing the interaction between a single atom and a classical light field (e.g. a laser). We then move on to the Jaynes-Cummings model, where the light field is quantised. This model can then be generalised to the case of many atoms, and multiple light modes, to form a fully-quantum many-body model of light-matter interactions.

2.4.1 Semi-Classical Model

A good starting point for studying light-matter interactions is to begin with a semi-classical picture, and consider an atom, described quantum mechanically, interacting with a classical light field [61,95,96,105]. We assume this light field to have a periodic profile, such that the associated electric field $\boldsymbol{\mathcal{E}} = \boldsymbol{\mathcal{E}}_0 \cos(\omega_0 t)$, where $\boldsymbol{\mathcal{E}}_0$ is the maximum field amplitude, and ω_0 is the frequency of the light. This is the sort of profile one would expect of a light source such as a laser. Note that in this description, it is implicitly assumed that the system with which the light interacts is much smaller than the wavelength of the light, such that the spatial profile of the beam may be neglected. We describe the atom as a two-level system, with ground state $|g\rangle$, excited state $|e\rangle$, and energy difference ω_a. The atom possesses a dipole moment $\boldsymbol{d}$, and thus the resulting interaction is given by $H_{\text{int}} = -\boldsymbol{d}.\boldsymbol{\mathcal{E}} = V_0 \cos(\omega_0 t)$, where $V_0 \equiv -\boldsymbol{d}.\boldsymbol{\mathcal{E}}_0$.

The state of the atom can be expressed generically as

$$|\psi(t)\rangle = c_g(t)|g\rangle + c_e(t)e^{-i\omega_a t}|e\rangle. \tag{2.52}$$

We say that the atom 'populates' a particular state, and refer to $|c_{g,e}|^2$ as the population of the states. Substituting this state into the Schrödinger equation Eq. (2.6) with the appropriate Hamiltonian $H = \omega_a|e\rangle\langle e| + H_{\text{int}}$, and using that the diagonal

dipole elements $\langle k|\boldsymbol{d}|k\rangle$ vanish due to a parity selection rule, we can obtain equations describing the time evolution of the amplitudes:

$$\frac{dc_g}{dt} = -i\mathcal{V}\cos(\omega_0 t)e^{-i\omega_a t}c_e \tag{2.53a}$$

$$\frac{dc_e}{dt} = -i\mathcal{V}\cos(\omega_0 t)e^{i\omega_a t}c_g, \tag{2.53b}$$

where we define $\mathcal{V} = \langle e|V_0|g\rangle$, assumed to be real. In the rotating wave approximation, we assume that the detuning $\Delta = \omega_a - \omega_0$ is much smaller than their sum $\omega_0 + \omega_a$, and thus that these rapidly-oscillating terms may be neglected as they average to zero on the timescales considered. Taking the initial state to be $|\psi(t=0)\rangle = |g\rangle$, we can solve these equations, to obtain

$$c_g(t) = e^{i\Delta\frac{t}{2}}\left(\cos\left(\Omega\frac{t}{2}\right) - i\frac{\Delta}{\Omega}\sin\left(\Omega\frac{t}{2}\right)\right) \tag{2.54a}$$

$$c_e(t) = ie^{i\delta\frac{t}{2}}\frac{\mathcal{V}}{\Omega}\sin\left(\Omega\frac{t}{2}\right), \tag{2.54b}$$

where the Rabi frequency

$$\Omega \equiv \sqrt{\Delta^2 + \mathcal{V}^2}. \tag{2.55}$$

Thus, the light drives transitions between the two levels, with a periodic oscillation in population. An interesting case is when the frequency of the light field is resonant with the transition energy ($\Delta = 0$); then, there is total oscillation of the population. For on-resonance illumination, after a time $\Omega t = \pi/2$ ('Rabi $\pi/2$ pulse'), the two states are in an equal-weight superposition, while at time $\Omega t = \pi$ ('Rabi π pulse'), there is total population transfer to the excited state.

2.4.2 Jaynes-Cummings Model

We can build upon this semi-classical model, and consider again the case of a single two-level atom, but now interacting with a quantised light field, to describe a fully-quantum model of light-matter interactions [61, 105, 106]. The electric field is quantised by replacing the above classical expression with one in terms of creation and

annihilation operators $a^\dagger$ and a for the light mode. Doing so results in a Hamiltonian of the form

$$H = \omega_0 a^\dagger a + \frac{\omega_a}{2}\sigma^Z + g(a + a^\dagger)(\sigma^+ + \sigma^-), \tag{2.56}$$

where the first term corresponds to the light field energy, the second the energy of the atomic states, and the third the light-matter interaction. We have expressed the atomic states in terms of the associated Pauli operators Eqs. (2.36), and parameterised the light-matter interaction by a coupling constant g. Considering the time-dependence of the operators, we can again make a rotating wave approximation to remove the rapidly-varying terms, resulting in the Jaynes-Cummings Hamiltonian:

$$H_{\text{JC}} = \omega_0 a^\dagger a + \frac{\omega_a}{2}\sigma^Z + g(a\sigma^+ + a^\dagger\sigma^-). \tag{2.57}$$

One sees that we can recover the semi-classical Hamiltonian when the light field is given by a coherent state $|\alpha\rangle$ with a large amplitude $\alpha \gg 1$. An interesting thing to note about this Hamiltonian is that it conserves the total number of excitations across the atoms and light field. Thus, the dynamics can be split into the dynamics of a series of two-state subspaces individually, the states in each subspace being $|n\rangle|e\rangle$ and $|n+1\rangle|g\rangle$, where $|n\rangle$ is the state where the light mode contains n photons. These pairs of states are called dressed states, and the light-matter term causes oscillations in the population between these two states.

2.4.3 Fully-Quantum Many-Body Model

Armed with the Jaynes-Cummings Hamiltonian, we are almost in a position to describe a fully-quantum many-body model of light-matter interactions [29, 31]. First though, we must consider the intermediate step, wherein we consider a further single-atom model, where we allow the atom to be mobile, with some non-negligible spatial profile, interacting with multiple light modes. Once we have such a model, it can readily be generalised to the many-atom case.

We take the Jaynes-Cummings Hamiltonian Eq. (2.57), and introduce multiple light modes for the atom to interact with, and now consider their spatial profile, described by modefunctions $u(\boldsymbol{r})$, which satisfy the normalisation $\int d\boldsymbol{r}|u(\boldsymbol{r})|^2 = 1$. We also allow the atoms to move within a trapping potential $V_T(\boldsymbol{r})$. The associated Hamiltonian is

$$H_{\mathrm{SP}} = \sum_m \omega_m a_m^\dagger a_m - \frac{\nabla^2}{2m} + V_T(\boldsymbol{r}) + \frac{\omega_a}{2}\sigma^Z + \sum_m g_m(a_m u_m(\boldsymbol{r})\sigma^+ + a_m^\dagger u_m^*(\boldsymbol{r})\sigma^-). \quad (2.58)$$

One can use this Hamiltonian to obtain the time dependence of the atomic operators σ^j from the Heisenberg equation Eq. (2.15). Moving to an interaction picture rotating at some reference frequency ω_p (we will later define this as being equal to one of the light mode frequencies), we can adiabatically eliminate the excited state of the atom. In doing so, we assume the light modes are sufficiently detuned from the atomic frequency that the excited state has negligible population, and so we can set the time dependence of the atomic operator in this frame to vanish. This corresponds to equating the atomic lowering operator $\sigma^- = (1/\Delta_a)\sum_m g_m u_m(\boldsymbol{r})a_m$, where $\Delta_a = \omega_p - \omega_a$ is the detuning between the reference frequency and the transition frequency. Inserting this back into our single-particle Hamiltonian Eq. (2.58), we obtain the effective Hamiltonian

$$H_{\mathrm{SP}} = \sum_m \omega_m a_m^\dagger a_m - \frac{\nabla^2}{2m} + V_T(\boldsymbol{r}) + \frac{1}{\Delta_a}\sum_{mn} g_m g_n u_m^*(\boldsymbol{r})u_n(\boldsymbol{r})a_m^\dagger a_n. \quad (2.59)$$

We now use this single particle Hamiltonian as a base for determining the many-body Hamiltonian. We consider the trapping potential to have a strong periodic component (specifically, here we consider an optical lattice), and proceed as we did for the Bose-Hubbard model, and express the state in terms of localised basis states $\psi(\boldsymbol{r}) = \sum_j w(\boldsymbol{r} - \boldsymbol{r}_j)b_j$. We can split the resulting Hamiltonian into three parts

$$\mathcal{H} = H_L + H_M + H_{LM}. \quad (2.60)$$

The first term $H_L = \sum_m \omega_m a_m^\dagger a_m$ describes the energy associated with occupation of the light modes. The second describes the behaviour of the atoms in the absence

of light interactions; that is, H_M is the Bose-Hubbard Hamiltonian Eq. (2.47). The final term describes the interaction between the light modes and the atoms, and we can write this fully-quantum interaction Hamiltonian

$$H_{LM} = \frac{1}{\Delta_a} \sum_{mn} g_m g_n a_m^\dagger a_n \sum_{ij} J_{ij}^{mn} b_i^\dagger b_j. \tag{2.61}$$

The coefficients

$$J_{ij}^{mn} = \int d\boldsymbol{r} w(\boldsymbol{r} - \boldsymbol{r}_i) u_m^*(\boldsymbol{r}) u_n(\boldsymbol{r}) w(\boldsymbol{r} - \boldsymbol{r}_j), \tag{2.62}$$

given by the overlap of the light modefunctions and the atomic wavefunctions, parameterise the strength of the light-matter interactions. Note that these coefficients may be complex, and due to the flexibility of the optical geometry, they have a great degree of tunability. We will exploit this asset later in this thesis, when we use the light-matter interaction to measure and control the atomic dynamics.

When we later consider this model, we use it as a model of light-scattering from a coherent pump beam, by the atoms in the lattice, into an optical cavity (or cavities). We label this pump mode 0, and assume it to be a coherent state with amplitude α_0, with an occupation much larger than the other modes (as noted earlier, we take the frequency of this pump ω_p as our reference frequency). Inserting this into the above Hamiltonian, and assuming that the light-scattering occurs on timescales much shorter than the atomic dynamics, we can use the Heisenberg equation Eq. (2.15) to find the steady states of the cavity modes in the interaction picture, at frames again rotating at the pump frequency. These steady states are given by

$$a_m = C_m \mathcal{J}_{m0} \equiv \frac{\Omega_{m0}\alpha_0}{i\kappa_m + \Delta_m} \mathcal{J}_{m0}, \tag{2.63}$$

where we define the light-matter coupling operators $\mathcal{J}_{mn} = \sum_{ij} J_{ij}^{mn} b_i^\dagger b_j$, $\Omega_{mn} = g_m g_n / \Delta_a$, the cavity mode detunings $\Delta_m = \omega_p - \omega_m$, κ_m is the rate of decay of photons from mode m, and we have assumed a small dispersive frequency shift of the light modes ($\Omega_{mm}\mathcal{J}_{mm} \ll \Delta_m$ for $m \neq 0$).

Chapter 3

Non-Destructive Probing of Ultracold Atomic Systems

Ultracold quantum gases have proved a highly suitable candidate for the implementation of quantum technologies, due to the impressive level of control and versatility achieved in experiments with such systems [22, 26, 70, 107]. A necessary component of these implementations is the ability to read out properties of the system state; that is, make a measurement. Typical methods for measuring ultracold gases include time-of-flight imaging of the momentum distribution [107–111] and in-situ density imaging [112–115]. Such methods bear the drawback that they necessitate destruction of the system, and since each measurement is essentially of a single-shot of the system state, to find averages one must repeatedly trap and cool the system multiple times.

An alternative method that has recently been proposed is to use a trapped atomic impurity that is immersed in the system [116–130]. The interaction between the impurity and the gas leads to their entanglement, and from the resultant dephasing of the internal impurity states, measurement of the impurity will reveal information about the gas. This dephasing relates to the system operator describing the interaction. When the impurity states can be modelled as a qubit, this probing can be considered analogous to Ramsey interferometry. We prescribe a scheme where this dephasing can be measured and used as a characteristic function, from which one can obtain

moments of the system operator, while being non-destructive of the target system. We describe how the protocol could be implemented for an atomic gas, and show how one can obtain means, variances, and correlations of the gas density. We simulate such an application for the one-dimensional Bose-Hubbard model, demonstrating that even in the presence of realistic experimental error, density-related properties can be recovered across a range of phases of the system. We then provide an outlook for further applications of the protocol. [1]

3.1 The Dephasing Function

We first develop the protocol generically, before specialising to the case of ultracold quantum gases. Thus, the results derived in this section are not contingent on the particular system, and can be applied to the study and characterisation of systems beyond ultracold atoms.

3.1.1 Extracting the Dephasing Function

Consider a probe qubit with Hamiltonian $H_q = \omega_q|1\rangle\langle 1|$ interacting with a system with Hamiltonian H_{sys}. Here, ω_q is the energy difference between the qubit states $\{|0\rangle, |1\rangle\}$. We consider the case where state $|1\rangle$ couples to a system operator H_{int} (which we refer to as the interaction Hamiltonian) with coupling strength κ, such that the combined system is described by the Hamiltonian

$$\mathcal{H} = \mathbb{I} \otimes H_{\text{sys}} + H_q \otimes \mathbb{I} + \kappa|1\rangle\langle 1| \otimes H_{\text{int}}. \tag{3.1}$$

We define the Hamiltonians describing the system evolution under each of the qubit states as $H_0 = H_{\text{sys}}$ and $H_1 = H_{\text{sys}} + \kappa H_{\text{int}}$. More generally, one can define $H_j = \langle j|\mathcal{H}|j\rangle$, and we remark that the crucial quantity in our analysis is actually $H_1 - H_0$, rather than the interaction Hamiltonian H_{int} itself, though the two are equivalent in our description. As such, it is not critical to the protocol that state $|0\rangle$

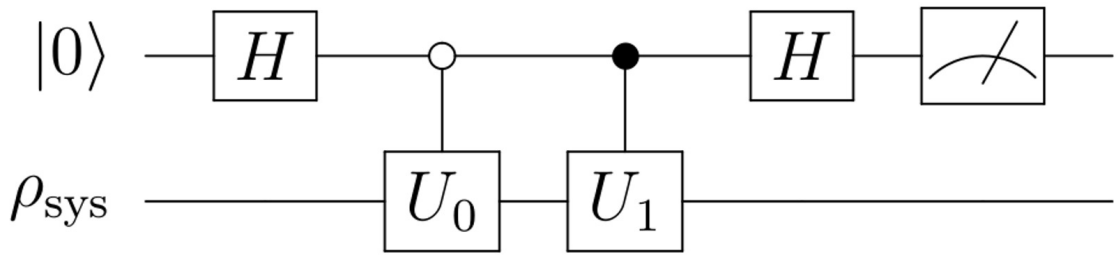

Figure 3.1: **Quantum circuit for measuring the dephasing function.** A qubit is used to control gates in a circuit that determines the dephasing due to the interaction Hamiltonian. Here, $H = (\sigma^X + \sigma^Z)\sqrt{2}$ is the Hadamard gate, and $U_j = \exp(-iH_j t)$ is the evolution of the system under the Hamiltonians H_j for a time t.

is non-interacting, provided the difference between the interaction Hamiltonians of the two states has the desired form.

Implementing a Ramsey interferometry-like scheme, using the qubit as the control for the system evolution [Fig. 3.1], we initialise the probe qubit at times $t < 0$ in the non-interacting state $|0\rangle$, and the system in the state ρ_{sys} of which we desire to determine the properties. At $t = 0$, the qubit is suddenly switched into the state $(|0\rangle + |1\rangle)/\sqrt{2}$. Equivalently, the qubit may be initialised in this state, with $\kappa = 0$ for $t < 0$, and then suddenly ramped up to its full value at $t = 0$.

For times $t \geq 0$, the system and qubit then evolve under the Hamiltonian Eq. (3.1), and we may trace out the system state to determine the qubit state at time t to be given by

$$\rho_q(t) = \frac{1}{2}\begin{pmatrix} 1 & e^{i\omega_q t}L(t) \\ e^{-i\omega_q t}L^*(t) & 1 \end{pmatrix}. \tag{3.2}$$

Here we define the dephasing function $L(t)$ (sometimes also referred to as the overlap function):

$$L(t) \equiv \text{Tr}(e^{-iH_0 t}\rho_{\text{sys}}e^{iH_1 t}) = \langle e^{iH_1 t}e^{-iH_0 t}\rangle, \tag{3.3}$$

where the expectation is taken over the initial system state ρ_{sys}. The values of the dephasing function are directly related to the expectation values of the Pauli operators Eqs. (2.36) for the qubit, with $\langle\sigma^X\rangle = \Re(\exp(i\omega_q t)L(t))$ and $\langle\sigma^Y\rangle = \Im(\exp(i\omega_q t)L(t))$.

Previously, this dephasing function has been investigated to study properties such as the orthogonality catastrophe in ultracold fermions [118, 119], the Luttinger parameter [116], and superfluid excitations [130], as well as a method of thermometry [117, 125, 128, 129], and to extract work distributions [120, 123, 127]. Some of these works consider different physical implementations of system and probe, such as trapped ions [120] and nuclear spins [127], suggesting further applicability of our results beyond ultracold gases. In this work, motivated by the similar structure it shares with characteristic functions of probability distributions [126], we will proceed by investigating its derivatives.

3.1.2 Derivatives of the Dephasing Function

In the strong-coupling limit, defined by the regime in which energies associated with the interaction κH_{int} are much larger than those of the system Hamiltonian H_{sys}, we may at sufficiently short times that $\langle \exp(iH_{\text{sys}}t)\rangle \approx 1$ approximate the dephasing function as $L_{\text{str}}(t) = \langle \exp(i\kappa H_{\text{int}}t)\rangle$. This is precisely the characteristic function of the interaction Hamiltonian, and thus, like such functions in probability theory, all of the moments can be obtained directly from the derivatives at $t = 0$:

$$\langle H_{\text{int}}^n \rangle = \frac{1}{(i\kappa)^n} \frac{d^n L_{\text{str}}(t)}{dt^n}\bigg|_{t=0}. \tag{3.4}$$

Though it provides access to all the moments, this limit carries the drawback that it may not easily be accessible in experiment for some systems, due to the requirement that a large coupling strength must be engineered between system and probe. In particular, for the specific implementation with ultracold gases that we shall consider later, the system-probe interaction is manifest by the same physical mechanism as interactions within the system (s-wave scattering), and so while this strongly interacting regime may be accessible when the gas is weakly interacting and very low temperature [131], for strongly interacting systems one may only consider weakly interacting probes [132], or where the two interactions are of similar magnitude

[133]. Increasing the coupling strength also decreases the timescales over which the evolution of $L(t)$ takes place, and hence also requires sufficiently quick switching of the qubit state (or ramping of κ), and a sufficiently fine time-resolution of the qubit measurements that the derivatives at $t = 0$ are accessible (for a typical strongly interacting ultracold gas, the system Hamiltonian contains interactions $\mathcal{O}(10^4\hbar\text{Hz})$ [72], which would then require measurements to be made on sub-μs timescales for a strongly interacting probe).

Positively, we find that it is possible for the first two moments of H_{int} to be extracted for an arbitrary non-zero κ. Indeed, considering the derivatives of $L(t)$ at $t = 0$ directly, we obtain

$$\langle H_{\text{int}} \rangle = \frac{1}{i\kappa} \left. \frac{dL(t)}{dt} \right|_{t=0}, \tag{3.5}$$

and

$$\langle H_{\text{int}}^2 \rangle = -\frac{1}{\kappa^2} \Re \left(\left. \frac{d^2 L(t)}{dt^2} \right|_{t=0} \right), \tag{3.6}$$

where we make use of the commutator of the two Hermitian operators $[H_0, H_1]$ being anti-Hermitian, and hence having purely imaginary expectation values. We now focus on these first two moments of the interaction Hamiltonian H_{int}, as they may be extracted from derivatives of the dephasing function $L(t)$ for any κ, allowing for more experimental flexibility.

3.1.3 An Estimation Protocol and Errors

For short times, the first and second derivatives Eqs. (3.5) and (3.6) dominate the imaginary and real parts of the dephasing function derivatives respectively, and thus the first two moments can be extracted by fitting linear and quadratic functions to the initial behaviour of $L(t)$, using that $L(0) = 1$.

Specifically, we first obtain estimates $\hat{L}(t)$ of the values $L(t)$, at the (discrete) measurement times. Whilst this in principle can be done for arbitrary time points,

we shall consider there to be equal spacing of measurements, such that they are made at times $n\Delta t$, for positive integer n up to a maximum N_ϵ corresponding to time $t_\epsilon = N_\epsilon \Delta t$. We then perform least-squares estimations, by minimising the functions

$$\sum_{n=1}^{N_\epsilon} (\Im(\hat{L}(n\Delta t)) - \alpha n\Delta t)^2 \tag{3.7}$$

and

$$\sum_{n=1}^{N_\epsilon} \left(\Re(\hat{L}(n\Delta t)) - 1 - \frac{\beta}{2}(n\Delta t)^2 \right)^2 \tag{3.8}$$

with respect to α and β. The minimising values $\hat{\alpha}$ and $\hat{\beta}$ then form our estimates for the moments $\kappa\langle H_{\text{int}}\rangle$ and $-\kappa^2\langle H_{\text{int}}^2\rangle$ respectively. In our simulations, we will take these values as our final estimates. However, one can use this estimate to apply a weighting to the terms in the least-squares fits, by estimating the magnitude of the error for that term (see below), and iteratively refitting, to obtain a better estimate.

The choice of t_ϵ should be such that it optimises the number of points used in the fit, without being so large that the imaginary and real parts of $L(t)$ cease to behave approximately linearly and quadratically respectively. Such deviations could be accounted for however, by including additional, higher-order terms in the fit, whose estimated coefficients are afterwards discarded.

The original estimates $\hat{L}(t)$ of $L(t)$ are obtained from the estimates of $\langle\sigma^X\rangle$ and $\langle\sigma^Y\rangle$, determined by averaging the outcomes of N repeated measurements made of the probe qubit. These estimates are unbiased, and for enough measurements can be modelled by a Gaussian distribution with a variance that can be calculated from $L(t)$. Specifically, the variance is given by $(1 + L(t))(1 - L(t))/4N$, and will hence attenuate to at most a few percent after a moderate number of measurements. In our simulations, we will treat this finite number of measurements as the main source of error in estimating $L(t)$, though other noise-based random errors (such as imprecision in the time at which measurements are made, and stochastic imperfections in the gate implementation) will behave in the same manner, and so can be considered

equivalently. Modelling such errors with zero mean as Gaussian noise, their variance will also scale inversely proportional to the number of measurements made, and with the errors adding in quadrature, we take the linear sum of the variance from all such errors as our total variance. Thus, the effect of such errors can be ameliorated by performing additional impurity measurements.

We will also implicitly account for the error that results from the discrete and finite nature of the timesteps at which measurements of the probe are made. Other errors, not directly accounted for in our treatement, are the finite time required to implement gates (which becomes negligible when gate operation timescales are much smaller than Δt), and systematic imperfections in the gate implementation. This latter error results in a deterministic multiplicative factor to the dephasing function (for a qubit probe initialised instead in the state $c_0|0\rangle + c_1|1\rangle$, this factor is given by $2c_0c_1^*$) [129], and may be detected and accounted for by determining the corrective factor needed to ensure $L(0) = 1$.

3.2 Implementation in Ultracold Atomic Systems

We now suggest a possible implementation of the protocol for use in probing ultracold (single species) atomic gases. We consider a probe qubit formed by two internal states of an impurity atom of a different species [119], trapped deeply in its own potential, such that its spatial wavefunction $\psi_q(\boldsymbol{r})$ is fixed, and may be considered as a c-number function (this approximation being valid when the trapping potential is much deeper than the interaction energy κ).

The necessary gates may be applied to the impurity by a Rabi laser pulse [61, 95, 96], and the measurements may be performed by using further gates and state-dependent fluorescing. With interparticle interactions suppressed within the impurity gas (or when the gas has sufficiently low density that they are anyway negligible), multiple impurity probes can be active simultaneously within the host gas, as illustrated in Fig. 3.2. Such mixtures of quantum gases have already been achieved and

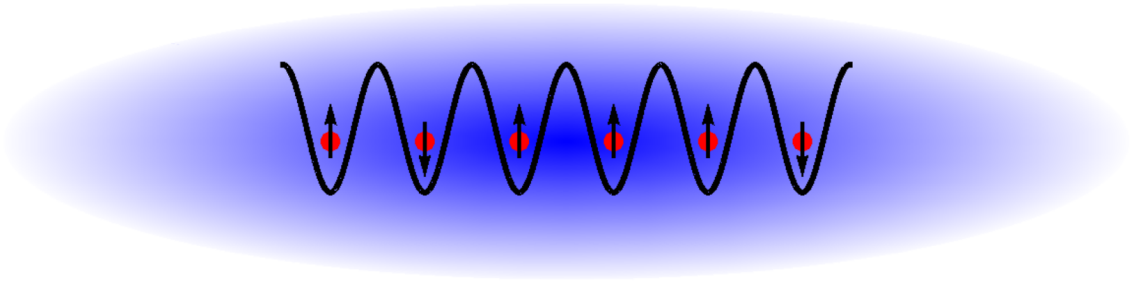

Figure 3.2: **Implementation of the scheme to probe ultracold atomic gases.** The quantum gas is represented by the blue cloud, with the immersed impurity probes signified by the red atoms. Measurement of the impurity internal states (represented by the arrows) reveals information about the dephasing due to the interaction Hamiltonian.

tuned experimentally [133–136]. Indeed, studies of the motion and decoherence of impurities in bosonic quantum gases have already been performed [131, 132]. Repeat measurements do not require the gas and impurities to be retrapped, and hence can be non-destructive, though the measurement of the impurity state will have a backaction that perturbs the system, and so the scheme is not non-demolition.

The impurity gas interacts with the atoms in the host gas through atomic s-wave scattering, which may be tuned through Feshbach resonances using external magnetic fields [97, 98, 111]. This leads to an interaction of the form

$$H_{\text{int}} = \int d\boldsymbol{r} n(\boldsymbol{r})|\psi_q(\boldsymbol{r})|^2 \equiv \tilde{n}(\boldsymbol{r}), \tag{3.9}$$

where $n(\boldsymbol{r})$ is the atomic density in the system, and $\tilde{n}(\boldsymbol{r})$ is the same density, coarse-grained over the impurity density $|\psi_q(\boldsymbol{r})|^2$. Our protocol thus allows for the probing of moments of this coarse-grained density. Focussing on the case where the impurity is highly-localised (on length scales defined by the variation in the system density) around the point $\boldsymbol{r}_q$, $\tilde{n}(\boldsymbol{r})$ is then given by the gas density at this point, $n(\boldsymbol{r}_q)$. In this case, our protocol allows for the estimation of the moments of the density at this point, $\langle n(\boldsymbol{r}_q)\rangle$ and $\langle n(\boldsymbol{r}_q)^2\rangle$, through Eqs. (3.5) and (3.6). Since the impurities can be localised to regions smaller than the wavelength of light, the spatial resolution can potentially be higher than for in-situ imaging.

This notion can be extended to consider the case where an impurity is in a superposition of being localised to two distinct locations $\boldsymbol{r}_{q_1}$ and $\boldsymbol{r}_{q_2}$ (by, for example, placing the impurity into a lattice potential, and using tunnelling as a beamsplitter operation [137]). In this setup, the coarse-grained density becomes $\tilde{n}(\boldsymbol{r}) = (n(\boldsymbol{r}_{q_1}) + n(\boldsymbol{r}_{q_2}))/2$, and the protocol can thus be used, in conjunction with the results for the case of an impurity localised to a single location, to obtain an estimate for the density correlation function $\langle n(\boldsymbol{r}_{q_1})n(\boldsymbol{r}_{q_2})\rangle$. Since for ultracold atoms typical tunnelling timescales are $\mathcal{O}$(ms) [72], one may not even need to quench the impurity trap after the beamsplitter tunnelling is performed, provided that measurements are made on at most $\mathcal{O}(100\mu\text{s})$ timescales. An alternative way this quantity can be measured is to use two impurities, each localised at one of the locations, and prepare their internal states in the entangled state $(|00\rangle + |11\rangle)/\sqrt{2}$, leading them to behave as a single effective qubit with a density equal to that of the individual probes.

3.3 Simulation for Ultracold Atoms in a Lattice

We now simulate an example application of the protocol to study density-based properties of a Bose gas. The particular system we shall consider is an ultracold gas trapped in an optical lattice, obeying the one-dimensional Bose-Hubbard Hamiltonian Eq. (2.47). Our simulated system will be composed of 101 lattice sites at unit filling factor, and we examine the system for U/J in the interval $0.1 : 6$, spanning the full phase diagram at this filling factor [26]. We shall concern ourselves with only the ground state of the system.

We adopt a choice of parameters selected to be realistic considering current experimental works. We use a coupling strength $\kappa = J$, and time-resolution $\Delta t J = 0.05$, allowing for $N_\epsilon \lesssim 20$ measurements to be used in the fit. For typical $J \sim 10^3\hbar$Hz [72], this corresponds to a measurement interval $\Delta t \sim 50\mu$s. Generically, the parameters are chosen such that the relationship between timescales obeys $t_L > t_\epsilon > \Delta t > t_s$,

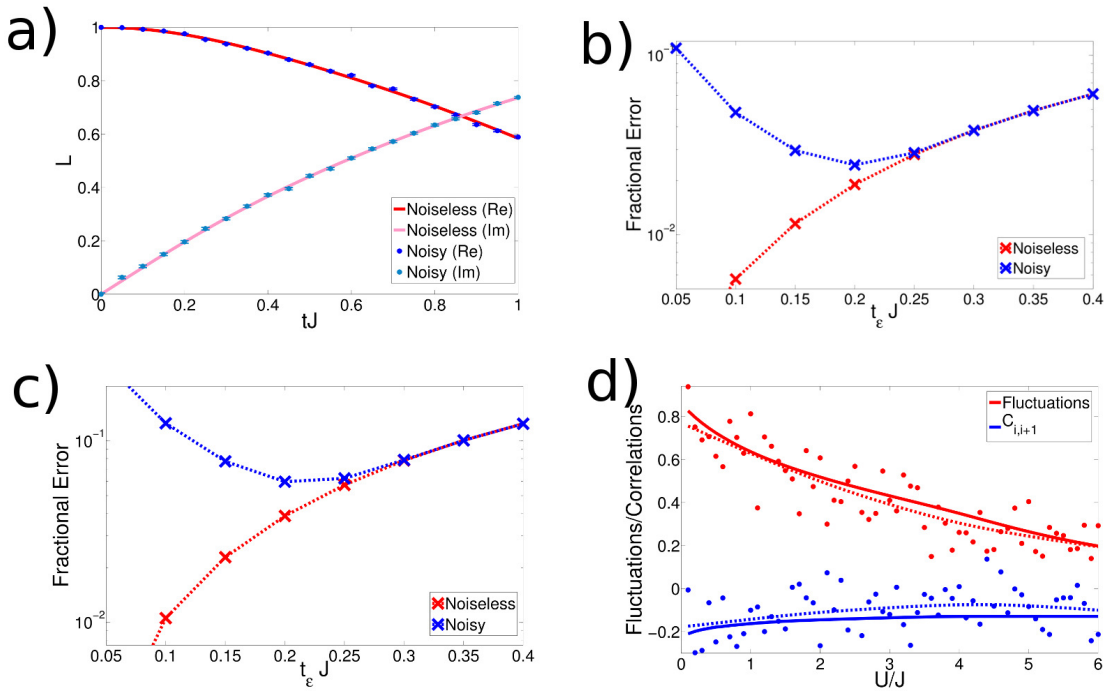

Figure 3.3: **Example application of the protocol.** (a) The effect of Gaussian white noise on the dephasing function, with error bars denoting the standard deviation. The fractional error in the calculated (b) density and (c) square of density with increasing length of time used for the fit. (d) Fluctuations and correlations; solid lines show exact values, markers show the calculated values, and dashed lines the fits to calculated values. Plots (a-c) simulate a system with $U = 3J$, and for all plots $\kappa = J$ with a measurement resolution $\Delta t J = 0.05$.

where $t_L \sim 1/\kappa$ is the timescale at which $L(t)$ begins to deviate significantly from its $t = 0$ behaviour, and t_s is the timescale on which measurements and gates can be performed.

Using these parameters, we simulate the application of our protocol by calculating $L(n\Delta t)$, adding stochastic noise to these values to simulate how estimates $\hat{L}(n\Delta t)$ would be obtained in a real experiment, and then estimate one- and two-site correlations from these simulated values. These estimated values are then compared to exactly calculated equivalents, to determine the efficacy of the protocol. For both parts, calculating the dephasing function $L(t)$ and the exact ground state expectation values, we use the time-evolving block decimation (TEBD) algorithm [138–140] (see Appendix 3.A for details).

We begin the analysis by considering a single impurity that is localised to a point $\boldsymbol{r}_i$ near the central site $i = 51$, such that the interaction Hamiltonian is given by $H_{\text{int}} = n_i$. In Fig. 3.3(a) we plot the real and imaginary parts of the dephasing function $L(t)$ for $U/J = 3$, together with the simulated noise estimates $\hat{L}(n\Delta t)$ as would be obtained from $N = 10^4$ measurements of the impurity internal state after interference. We then apply our fitting procedure in order to estimate the derivatives of the dephasing function, and thus the moments of the interaction Hamiltonian, which in turn correspond to our estimates of $\langle n_i \rangle$ and $\langle n_i^2 \rangle$.

We analyse the choice of fitting time $t_\epsilon = N_\epsilon \Delta t$ used to estimate the expected occupation $\langle n_i \rangle$ in Fig. 3.3(b), by averaging over many noisy trajectories. As one would expect, the accuracy initially increases with N_ϵ, benefitting from the increase in the number of data points used in the fit, and corresponding decrease in random error. However, for larger t_ϵ, the accuracy decreases, as at these larger times the higher-order terms in $L(t)$ beyond the linear fit play an increasingly significant role, and thus introduce a systematic error. A similar analysis is shown for $\langle n_i^2 \rangle$ in Fig. 3.3(c), with the slight decrease in accuracy compared to the first moment highlighting the increasing difficulty in estimating higher-order derivatives, and thus moments. We find $t_\epsilon = 0.2J$, corresponding to $N_\epsilon = 4$, to be an approximately optimal choice for estimating the moments for our system.

With this t_ϵ, we assume the protocol is repeated with impurities configured such that $H_{\text{int}} = n_j$ is probed, and also for the delocalised/twin-impurity case $H_{\text{int}} = n_i + n_j$. From this, we then estimate not only the variance $\langle n_i^2 \rangle - \langle n_i \rangle^2$ of the central site, but also the correlations $C_{ij} = \langle n_i n_j \rangle - \langle n_i \rangle \langle n_j \rangle$ between the central site and neighbouring site $j = i + 1$. The results for the simulation of this are shown in Fig. 3.3(d). The markers show the value calculated for each U/J for single runs of noisy trajectories, and the dashed lines a fit from a cubic smoothing spline (defined as the function $f(x)$ which for a set of data y_i minimises $\sum_i (y_i - f(x_i))^2 - \lambda \int (d^2 f/dx^2)^2 dx$ [141]) fit over varying interaction strength for these data, with smoothing parameter $\lambda = 10^4$.

The solid lines show the exact values. We observe that while the individual data points display a noticeable error, the fit over the whole parameter range recovers the quantitive values faithfully to a reasonable degree of accuracy.

3.4 Further Applications of the Protocol

In the above simulations, we applied the protocol to measure density properties of the Bose-Hubbard model in one dimension. We note that in this case, the occupation number fluctuations vary smoothly across the phase diagram. In contrast, mean-field treatments of the model, valid in higher dimensions, find that $\langle b_i \rangle$ serves as a suitable order parameter for the superfluid-Mott insulator transition [100, 101]. The fluctuations in the density reveal whether this quantity is non-zero, and hence would allow for one to map out the phase diagram. Since our protocol is valid independent of the number of dimensions, this suggests that it could be used as a method for non-destructively probing the phase transition.

The range of applicability of our protocol can extend beyond the system we currently consider; indeed, any system that can be coupled to a controllable, measurable two-state system could be studied, such as trapped ions [120] and nuclear spins [127]. Through a manipulation of the interaction between the probe and system, other quantities may be probed, not just those related to density. For example, in a gas with spin, a spin-sensitive interaction (e.g. $\kappa \propto S^Z$) will engender moments of the interaction Hamiltonian corresponding to moments of the magnetisation of the gas, enabling such properties to be measured. One can also consider the effect of altering the impurity wavefunction; when the impurity has a sinusoidal density (e.g. a matter wave), the coarse-grained density corresponds to a Fourier transform, and the resulting moments are those of the momentum density. From this, one may be able to probe thermodynamical properties of the gas.

Another set of quantities similar to density that would be interesting to consider are the single-particle correlations $\langle b_i^\dagger b_j \rangle$. Focussing on the nearest-neighbour

case, the bond density $\langle b_i^\dagger b_{i+1}\rangle$, this term depends on the overlap of the Wannier functions of neighbouring sites. However, because at any position $\boldsymbol{r}$ the inequality $w(\boldsymbol{r}-\boldsymbol{r}_i)^2 + w(\boldsymbol{r}-\boldsymbol{r}_j)^2 \geq 2w(\boldsymbol{r}-\boldsymbol{r}_i)w(\boldsymbol{r}-\boldsymbol{r}_j)$ holds true, one cannot eliminate the on-site density terms when the impurity and system interact through contact interactions, and as the coarse-graining is done over the impurity density (a positive-definite function), a cancellation of these terms is not possible through manipulation of the impurity wavefunction. A possibility would be to instead engineer a different interaction Hamiltonian, where there is an (impurity) density-dependent tunnelling term [142] induced in the gas, conditional on the impurity state. In this case, the interaction Hamiltonian becomes $\lambda b_i^\dagger b_{i+1} + h.c.$, thus allowing for a direct probing of the bond density. Determining the moments of this quantity for different values of λ (e.g. λ_0 and $i\lambda_0$), one can extract the single-particle correlations between neighbouring sites, corresponding to the moments of the particle current.

3.A Time-Evolving Block Decimation Algorithm

The TEBD algorithm allows for the efficient classical simulation of the dynamical evolution of a pure quantum state on a one-dimensional lattice [138–140]. It operates by storing the state of the system as a matrix product state (MPS) [143], where the state is expressed as a series of matrices, one for each site, with each matrix storing values corresponding to the correlations between local basis states. Exact representation of an arbitrary quantum state may require an exponential scaling in the size of these matrices, parameterised by the 'bond dimension' χ. However, one can truncate the state at some value of this bond dimension to approximate the state, and ground states and low-lying excited states (including short time quenches, as we consider here) of local one-dimensional Hamiltonians may be very accurately represented by an MPS with a small bond dimension (typically $\mathcal{O}(1-10^2)$) [144] due to entanglement area laws [145], resulting in a tractable representation of the state.

The MPS is then evolved for each discrete timestep δt according to a Hamiltonian H formed of single- and two-site nearest-neighbour operators, after performing a Suzuki-Trotter decomposition [146] of the evolution operator $\exp(-iH\delta t)$, such that the evolution operator is also expressed (approximately) as a product of single- and two-site operators. The algorithm can also be used to obtain ground states of Hamiltonians, by evolving the system in imaginary time. Expectation values of single- and two-site operators can be calculated for an MPS after they too are expressed in matrix product representation.

The one-dimensional Bose-Hubbard model is well-suited for simulation by TEBD, as the Hamiltonian Eq. (2.47) consists only of one- and two-site nearest neighbour operators. For our simulations, we used imaginary time evolution in TEBD to obtain the ground state MPS, and evolved the resulting state according to each of H_0 and H_1. The overlap of the final evolved states then gives an expression for the dephasing function. We also used the ground state MPS to calculate expectation values for n_i and $n_i n_j$, so that we had exact values against which to compare the results obtained from the protocol. In our simulations, we limit the maximum occupation per site to 4 bosons, with a bond dimension $\chi = 50$, and evolution timestep $\delta t J = 10^{-3}$.

The code for used for the simulations was written and provided by Stephen Clark and Dieter Jaksch, and was run on the Jaksch group cluster 'Bose'.

Chapter 4

Multimode Atomic State Engineering by Light Measurement

We now elevate the role of measurement from being merely a tool to read out properties of a system to a tool that is actively used to influence how the system behaves. We do this through use of an optical cavity, used to enhance the light scattered from a probe beam by the atoms in a lattice. We first show how the choice of the optical geometry affects the relationship between the cavity population and the atomic configuration, and how this leads to the generation of a matter mode structure, where multiple sites may be grouped together by their equivalent response to the light field. These matter modes can be delocalised, and have very non-trivial spatial properties and overlap, allowing for novel interactions between them. We employ this matter mode structure for the purpose of state engineering, by using the backaction on the state heralded by the detection of photons leaked from the cavity, here constituting the measurement process. Specifically, we show how multimode generalisations of parametric down-converted (PDC), Dicke, and squeezed states may be generated, and investigate their entanglement properties. We show how this measurement-mediated state engineering can be used as a method to deterministically generate atomic mode entanglement, and further, we propose a method for using the matter mode structure to detect and measure entanglement in quantum gases [2].

4.1 Generation of the Matter Mode Structure

We study the Hamiltonian Eq. (2.60), describing the generalised Bose-Hubbard model with fully-quantum light-matter interactions [29]. Specifically, we are considering a single species of bosonic atoms, in a classical optical lattice, scattering quantised light from a probe [Fig. 4.1]. In the typical case where the on-site terms $D_{mn} = \sum_j J_{jj}^{mn} n_j$ dominate the light-matter interactions $\mathcal{J}_{mn}$, each Fock state configuration of the atoms $|\boldsymbol{n}\rangle = |n_1, \ldots, n_M\rangle$, corresponding to different occupations n_j of each of the M sites in the lattice, will scatter light from a probe in a coherent state $|\alpha_0\rangle$ into a corresponding coherent state with amplitude $\alpha_{m\boldsymbol{n}} = C_m \langle \boldsymbol{n}|D_{m0}|\boldsymbol{n}\rangle$ [41, 147]. Here, C_m is the free space or cavity Rayleigh scattering coefficient [148], as defined in Eq. (2.63), and in this limit of dominant on-site light-matter interaction terms we can approximate $J_{jj}^{m0} = u_m^*(\boldsymbol{r}_j) u_0(\boldsymbol{r}_j)$.

Due to the linearity of quantum mechanics, and since the general atomic state is a superposition of such Fock state configurations, the light and matter become entangled, with joint state (dropping the mode index m)

$$|\psi\rangle = \sum_{\{\boldsymbol{n}\}} c_{\boldsymbol{n}}^0 |\boldsymbol{n}\rangle |\alpha_{\boldsymbol{n}}\rangle. \tag{4.1}$$

4.1.1 Backaction Due to Light Measurement

When the light is scattered into a cavity with decay rate κ, detection of the escaped photons alters the probability amplitudes $c_{\boldsymbol{n}}$ from their initial values, according to $c_{\boldsymbol{n}}(k,t) = \alpha_{\boldsymbol{n}}^k \exp(-|\alpha_{\boldsymbol{n}}|^2 \kappa t) c_{\boldsymbol{n}}^0 / \mathcal{N}$, where the first factor reflects quantum jumps from the detection of k photons, the second factor the non-Hermitian evolution during times of non-detection, and $\mathcal{N}$ is a normalisation factor [29]. The measurement thus changes the state of both the light and the matter, manifesting the measurement backaction. Note that we assume that we are in the regime where this backaction happens on timescales much faster than the atomic dynamics, such that they may be

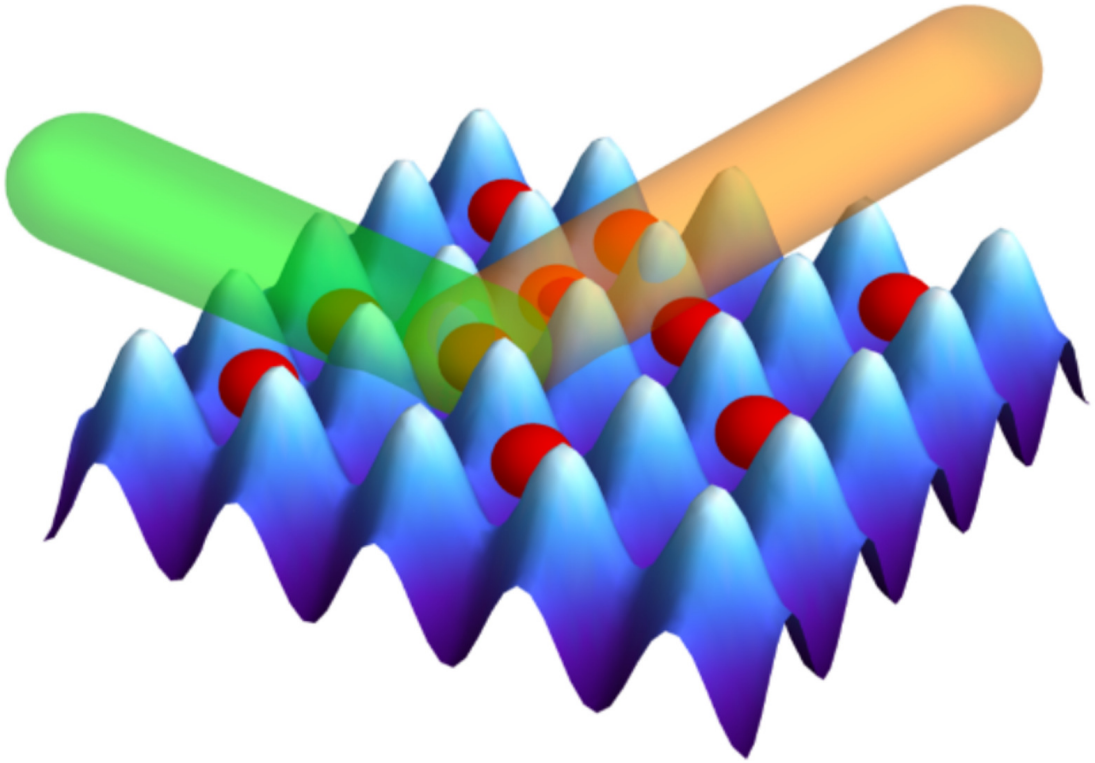

Figure 4.1: **Atomic scattering of quantised light.** Atoms in a classical optical lattice scatter quantum light from an incoming probe beam (green) into another mode (orange). The optical geometry generates a matter structure defined by the phase at which the atoms scatter light.

neglected. Light scattering into free space modes, rather than cavity modes, may also take place; we neglect such events however, as they occur with much less frequency due to the much lower light-matter coupling g_m for free space modes compared to cavities.

With the light field amplitude and phase measured in this way, the distribution of the $\alpha_{\boldsymbol{n}}$ is narrowed, and the state is gradually projected towards terms with a single particular $\alpha_{\boldsymbol{n}}$, as determined by the rate of photon detection. With continuous measurement, the light is subsequently pinned to this $\alpha_{\boldsymbol{n}}$ by the QZE [63–65], and the atoms will undergo QZD [66–68], whereby their evolution is constrained to evolve only within the region of Hilbert space with configurations $|\boldsymbol{n}\rangle$ corresponding to the measured $\alpha_{\boldsymbol{n}}$. This is in stark contrast to incoherent light scattering, where atoms are localised, and coherence is destroyed [149]. Strictly, it is not necessary to directly perform photodetection of the leaked photons, as the associated environmental decoherence due to such leakage will also manifest the locking to a Zeno subspace. However, measurement must be performed if we are to determine the subspace in which the system resides. For an imperfect detector of known efficiency, one may employ post-processing of the detection rate to estimate the true leakage rate, and hence the subspace. Once this subspace is determined it is not required to continue the measurement, as the Zeno-locking from decoherence will preserve the (now known) subspace. Such controlled dynamics can find application in quantum simulations, as we shall discuss in Chapter 5. For now, we shall focus on the possibilities for state engineering.

Current experiments have trapped Bose-Einstein condensates inside optical cavities, without an optical lattice [30, 32, 87], while other experiments have scattered light from quantum gases loaded in an optical lattice, into free space [115, 150]. Recently, state-of-the-art setups have united these two types of experiments, to realise a quantum gas loaded into an optical lattice potential, inside an optical cavity [34, 35]. Thus, the hybrid cavity-lattice system we consider has been achieved, albeit in a

simple form thus far. These hybrid systems currently do not achieve the requisite parameter regime for the light scattering to enforce Zeno dynamics ($|C|^2\kappa \gg J$, where J is the tunnelling rate from the standard Bose-Hubbard Hamiltonian); taking [34] as our example, the two rates are of similar magnitude $\mathcal{O}(10^3\text{Hz})$, and the former term may be feasibly increased by e.g. a modest reduction in the cavity detuning, or an increase in pump power, both of which have been achieved in previous incarnations of the setup [87].

4.1.2 Defining Matter Modes

When both the probe and cavity modefunctions are described by travelling waves with wave vector difference $\Delta\boldsymbol{k}$, we have that the cavity amplitude is proportional to

$$D = \sum_j e^{-ij\delta} n_j, \tag{4.2}$$

where $\delta = \Delta\boldsymbol{k}.\boldsymbol{d}$, with $\boldsymbol{d}$ the lattice vector. This is essentially Bragg diffraction [151]: depending on the choice of δ, the light can exhibit diffraction maxima ($\delta = 2n\pi$), and minima in-between. Thus, this choice determines the particular correspondence between atomic configurations $|\boldsymbol{n}\rangle$, and their respective cavity states $|\alpha_{\boldsymbol{n}}\rangle$. In turn, this choice defines the region of the atomic Hilbert space to which dynamics is constrained after the cavity state distribution is compressed and pinned to a single $\alpha_{\boldsymbol{n}}$ during the continuous light measurement.

A set of particular cases of interest are when we have $\delta = 2\pi/R$ for $R \in \mathbb{Z}$. In these cases, the atoms at all sites $j + nR$ scatter light with the same amplitude and phase, and are therefore indistinguishable in the cavity state. Crucially, this gives rise to R spatial atomic modes, whereby atoms at indistinguishable sites belong to the same mode, and different atomic modes scatter light with different phases.

Physically, these δ correspond to the angles of multiple diffraction minima, and a small number of maxima. For example, $\delta = 2\pi$ ($R = 1$) corresponds to the diffraction maximum with one mode (note, the case $\delta = 0$ is equivalent), as all illuminated

atoms scatter light in phase; $D = N_K$, where K is the set of illuminated sites, and $N_K = \sum_{j\in K} n_j$. The remaining $M - K$ non-illuminated sites can also be considered as an additional mode. The case $\delta = \pi$ ($R = 2$) represents the diffraction minimum for orthogonal light waves, and generates two modes, as atoms at neighbouring sites scatter light with opposite phase; $D = \sum_j (-1)^j n_j = N^{(\mathrm{even})} - N^{(\mathrm{odd})}$, the atom number difference between even and odd sites. For other diffraction minima, with larger R, more spatially-overlapping atomic modes are generated. Examples of indistinguishable configurations for $R = 3$ in one-dimension are shown in Fig. 4.2(a), while Fig. 4.2(b) shows the spatial structure of $R = 3$ matter modes in two dimensions.

With multiple cavities, it is possible to simultaneously measure multiple D operators. Indeed, measuring all of the D operators corresponding to $\delta = 2\pi n/R$ for $n \in [0, (R-1)/2] \cap \mathbb{Z}$ will allow for the full characterisation of R modes, where as before, we define the rth mode as being composed of all sites j satisfying $j \bmod R = r$. The measured operators can be written in the form of an invertible Vandermonde matrix [152], for which the inverse then reveals the occupation numbers of each mode (as the D operators form a system of linear equations describing mode occupation numbers). Ultimately, if $R = M$, this determines the occupation n_j of all lattice sites, without the need for single-site resolution [112–115], though for large numbers of lattice sites this may not be a practical limit to achieve experimentally due to the number of cavities required.

Although such effective single-site access would be useful for particular applications in quantum information processing, we will instead here focus on the many-body properties of the states. Importantly, for the typical $R < M$ cases, even after the atomic mode occupation numbers are determined, the modes are still described by superpositions of Fock state configurations with the same mode occupation numbers, and hence the dynamics is not completely frozen, even when the light state is frozen by the QZE. For example, the three configurations in Fig. 4.2(a) all correspond to the

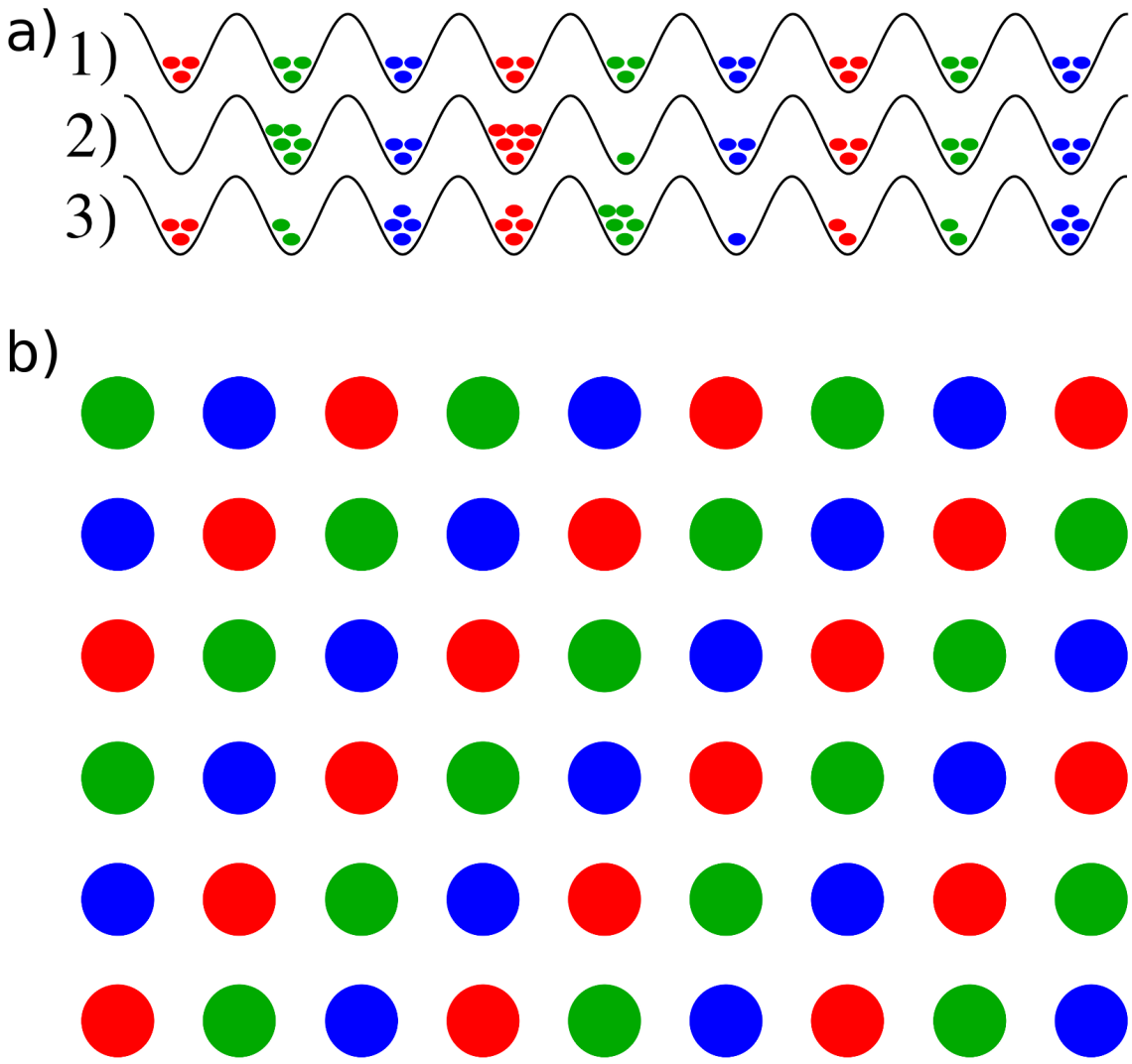

Figure 4.2: **Mode structure defined by light scattering.** (a) For $R = 3$, every third site scatters light with the same phase, and hence atoms on these sites belong to the same mode. The three configurations shown have equal total occupation of each mode, and are hence indistinguishable to light scattering, protecting superpositions of such states. (b) The corresponding mode structure for $R = 3$ in two dimensions.

same light state, and may hence still co-exist in a superposition after light measurement. Critically, though the total mode occupations are frozen, the same is not true of the constituent sites, and thus the motion of atoms within modes is still possible. This results in the generation of multiple 'virtual' lattices each formed by one of the modes, on a single physical lattice. It is also possible to allow a controlled subset of dynamics between modes by forgoing measurements for particular δ, as this reduces some of the constraints imposed on the modes by light measurement.

4.2 State Engineering of the Matter Modes

Here we shall focus on particular states of the matter modes that can be generated, and in Chapter 5 we shall discuss the dynamics within the modes. We shall assume here that the atoms are prepared initially in a superfluid state, delocalised over all the lattice sites. For a large lattice, this can be approximated by the Gutzwiller (mean-field) ansatz [26, 100, 101], in which the system is decribed by a product state of all sites in a coherent state, with amplitude dependent on the filling factor ν of the lattice:

$$|\psi\rangle_{\mathrm{GA}} = \bigotimes_{i=1}^{M} \sum_{n=0}^{\infty} \frac{e^{-\frac{\nu}{2}} \nu^{\frac{n}{2}}}{\sqrt{n!}} |n\rangle_i. \tag{4.3}$$

An external phase reference can be used to lock the phase of the state relative to the reference [153]. This can be done by e.g. releasing some of the atoms, and using a homodyne detection scheme, where the output statistics are dependent on the phase difference between the atomic state and the reference. This provides one way to escape constraints imposed by global atom number superselection rules; another would be to use an auxiliary part of the lattice as a particle reservoir.

4.2.1 Generalised Down-Conversion, Squeezed, and Dicke States

First consider the scenario where the amplitude and phase of the cavity state is determined by detection of the leaked light, for $\delta = \pi$. When using either post-

selection, or feedback methods (that is, conditional modification of the trapping potential [154–156]) to attain $\langle D \rangle = 0$ (such that the mode occupation number differences are also zero), the state is projected to

$$|\psi\rangle_{\mathrm{DC}} = \frac{1}{\mathcal{N}} \sum_{n=0}^{\infty} \frac{e^{-\lambda}}{n!} \lambda^n |n\rangle|n\rangle, \tag{4.4}$$

where $\lambda = \nu K/R$ is the average initial occupation number of each mode (here R=2, the two modes formed from the odd and even sites respectively). This state shows a great resemblance to the PDC states of quantum optics [61], which take the form $|\psi\rangle_{\mathrm{PDC}} = \sum_{n=0}^{\infty} c_n |n\rangle|n\rangle$, albeit with different coefficients c_n. Note that while either post-selection or feedback is needed to obtain equal mode occupation, the measurement will still always deterministically project to a state with a fixed occupation number difference ΔN between the two modes:

$$|\psi\rangle_{\mathrm{DC}} = \frac{1}{\mathcal{N}} \sum_{n=0}^{\infty} \frac{e^{-\lambda}}{\sqrt{n!(n+\Delta N)!}} \lambda^{n+\frac{\Delta N}{2}} |n\rangle|n+\Delta N\rangle. \tag{4.5}$$

For large N, this difference ΔN will become vanishingly small in comparison to the average mode occupation ($\Delta N \leq \mathcal{O}(\langle N \rangle^{1/2})$, and thus $\Delta N \ll \lambda$), hence the two states Eqs. (4.4) and (4.5) will exhibit many similar properties such as entanglement, and thus the use of post-selection or feedback is not strictly necessary, depending on the intended use of the state.

We can readily generalise this procedure to the case of several matter modes. By measuring all the D operators one would need to characterise R modes, except for $\delta = 0$ (which simply measures the total atom number), one obtains a state where the occupation number difference between all the matter modes are fixed. These thus form a class of multimode generalised down-converted states. A special case of this is when all $D = 0$, which corresponds to all modes having equal occupation numbers;

$$|\psi\rangle_{\mathrm{MDC}} = \frac{1}{\mathcal{N}} \sum_{n=0}^{\infty} \left(\frac{e^{-\lambda}\lambda^n}{n!} \right)^{\frac{R}{2}} |n\rangle^{\otimes R}. \tag{4.6}$$

For increasing λ, this particular state is obtained with exponentially vanishing probability, though essentially all the states that can be projected to in this manner share much the same properties as the 'ideal' case (and thus, this low probability to obtain the ideal case is irrelevant unless one desires that exact state). These multimode down-converted states show truly multimode properties, as they possesses genuine multipartite entanglement (whereby any choice of bipartitioning of the modes shows non-zero entanglement [90]). As the states are pure, we can calculate the amount of entanglement by using the entanglement entropy Eq. (2.41) [89]. Using $\lambda \gg 1$, and noting that the reduced density matrices are all diagonal, we can approximate the amplitudes (and hence probabilities) as a continuous function of n, and taking the central limit theorem, we find that for all possible bipartitionings the entanglement entropy of the ideal case Eq. (4.6) is

$$E = \frac{1}{2} \log \left(\frac{2\pi e \lambda}{R} \right), \tag{4.7}$$

with the more general states of this form also possessing a similar degree of entanglement.

This multimode state is in stark contrast to the simple 'multimode' PDC found in quantum optics, which do not have genuine multipartite entanglement (rather, they show entanglement between only pairs of modes) [157]. This is because in the quantum optical case photons are produced in pairs, and higher degrees of multipartite entanglement require larger numbers of photons to be produced simultaneously, which in turn relies on higher-order nonlinearities, which become increasingly difficult to achieve as they are generally suppressed with increasing order. Our scheme does not have any such drawback, and the only limit to the scaling is linear, in the number of measurement cavities required.

Taking the states that are output from this protocol, one can also create states that are analogous to generalised squeezed states [158], described by Hamiltonians of the form

$$H_{\mathrm{Sq}} = \varsigma a^k + h.c., \tag{4.8}$$

which, akin to down-conversion, would arise in quantum optical setups due to non-linear k-photon processes. Taking the multimode down-conversion state Eq. (4.6) (or one of the similar, less 'ideal' versions of the state), with the R matter modes taking the place of the k-photon process, and lowering the underlying classical lattice potential (though maintaining a global trap), the atoms will behave as a single mode, in the state

$$|\psi\rangle_{\mathrm{Sq}} = \sum_{n=0}^{\infty} c_n |N_0 + nR\rangle, \tag{4.9}$$

where N_0 and c_n depend on the particular multimode down-conversion state from which one started (for the case Eq. (4.6), $N_0 = 0$, and $c_n = (\exp(-\lambda)\lambda^n/n!)^{R/2}/\mathcal{N}$, and in general, one can determine N_0 from the sum of the occupation differences between modes, and c_n from the amplitudes of the original state). This state is a generalised form of a squeezed vacuum, from even number pairs, to triplets, quadruplets, and above, depending on R.

Further classes of states can be produced by varying the angles to perform different measurement schemes. The case $\delta = 0$, the diffraction maximum, reveals the total number of atoms illuminated, as noted above. This projects the state to a fixed atom number superfluid state [41]. By making several measurements of this form in different regions, or by measuring $\delta = 0$ in combination with other δ (such as those used in generating Eq. (4.6)) to then also fix the total atom number as well as differences, one obtains a product state of several superfluid states, with fixed atom number N_i:

$$|\psi\rangle_{\mathrm{Dicke}} = \bigotimes_{i=1}^{R} |N_i\rangle, \tag{4.10}$$

where the sites occupied by each superfluid depends on the particular matter mode structure of the measurement scheme. When converting from the mode basis back into the symmetrised particle basis, this state takes the form of a multimode generalisation of a Dicke state [159], formed from an equal superposition of all permutations of the form $|\psi_1\rangle^{\otimes N_1} \otimes \ldots \otimes |\psi_R\rangle^{\otimes N_R}$, where the $|\psi_i\rangle$ represent the single-particle basis states.

An intriguing feature of these superfluids is that because of the global nature of the light-scattering, the matter modes are typically delocalised in space (as shown in Fig. 4.2), and as a result, so are the superfluids. They thus have a non-trivial spatial overlap, and yet despite this overlap and their being the same species, their effective distinguishability imparted by the light (and the associated Zeno physics) ultimately prevents interactions between the superfluids.

Another interesting case of note is when $\delta = \pi$, the main diffraction minimum, is measured, but only for the amplitude, and not the phase. This results in two modes, where the magnitude of their difference in occupation number $|\Delta N|$ is determined, but not its sign. The resulting state is a superposition of cat states of light and matter.

$$|\psi\rangle_{\text{Cat}} = \frac{1}{\mathcal{N}} \sum_{n=0}^{\infty} \frac{e^{-\lambda} \lambda^{n+\frac{\Delta N}{2}}}{\sqrt{n!(n+\Delta N)!}} (|n\rangle|n+\Delta N\rangle|\alpha_{\Delta N}\rangle \pm |n+\Delta N\rangle|n\rangle|-\alpha_{\Delta N}\rangle). \quad (4.11)$$

If the probe light is then turned off, the cat state is purely between the atomic modes, which could then be maintained in the absence of freezing by light measurement by other means such as a quench to ramp up the lattice depth.

4.2.2 Measurement-Induced Growth of Entanglement

We have seen already how an initially disentangled state (the Gutzwiller superfluid ansatz) can be transformed into an entangled state solely through the backaction of light measurement. This occurs because the measurement has degeneracies in its outcomes, such that multiple states can coexist in a superposition after the measurement. For a simple example of this concept, consider the initially separable state $|+\rangle|+\rangle$ of two qubits, and perform a measurement of the total parity of the two qubits ($\sigma_z \otimes \sigma_z$). This will project to one of the Bell states (the particular one depending on the outcome of the measurement), which has entanglement entropy $E = 1$. Unlike this example though, the measurement performed here due to the light scattering is not

an instantaneous projective measurement, and so we can investigate the dynamical growth of the entanglement as the scattered light is detected.

We simulate the dynamics of the evolution under light scattering by use of the quantum trajectories technique [160]. The trajectories use a Monte Carlo method to determine the times at which a photon is detected, and at these times the appropriate jump operator is applied to the state, while the rest of the time it is subject to the non-Hermitian evolution as described above. We do this for three cases: (a) phase-sensitive measurement at the diffraction minimum ($\delta = \pi$); (b) diffraction maximum ($\delta = 0$); and (c) phase-insensitive measurement at the diffraction minimum ($\delta = \pi$), and plot the dynamical evolution of the entanglement in Fig. 4.3.

We see that during the measurement, though the light-matter entanglement must clearly be degrading as the light is channelled towards a definite state, matter-matter entanglement between initally separable matter modes is established, and grows towards some stable finite value as the light state becomes fixed, the final value depending on the particular light state to which the system converges. While the final entanglements converge to a small number of different values, as they are a function of the final light state, during the evolution the stochastic nature of the detection events are apparent. All three cases considered show similar values for the final average entanglement, though the distributions are different (see Fig. 4.3 insets).

For typical $\Delta N \ll \langle N \rangle$ in the diffraction minimum, the amplitudes of the resulting Fock states in Eq. (4.5) exhibit only a weak dependence on ΔN, and hence in this case [Fig. 4.3(a)] the width of the distribution of the final entanglements is small. Contrastingly, for the diffraction maximum [Fig. 4.3(b)], the distribution is broad, as the measurement projects to a superfluid with non-deterministic atom number N, and as the entanglement in such a state scales as $\log(N^{1/2})$ [161], E depends on the particular measured N. The final case, phase-insensitive diffraction minimum [Fig. 4.3(c)], the distribution is yet broader, due to the additional element of the state being composed of a superposition of individual cat states. This case has the

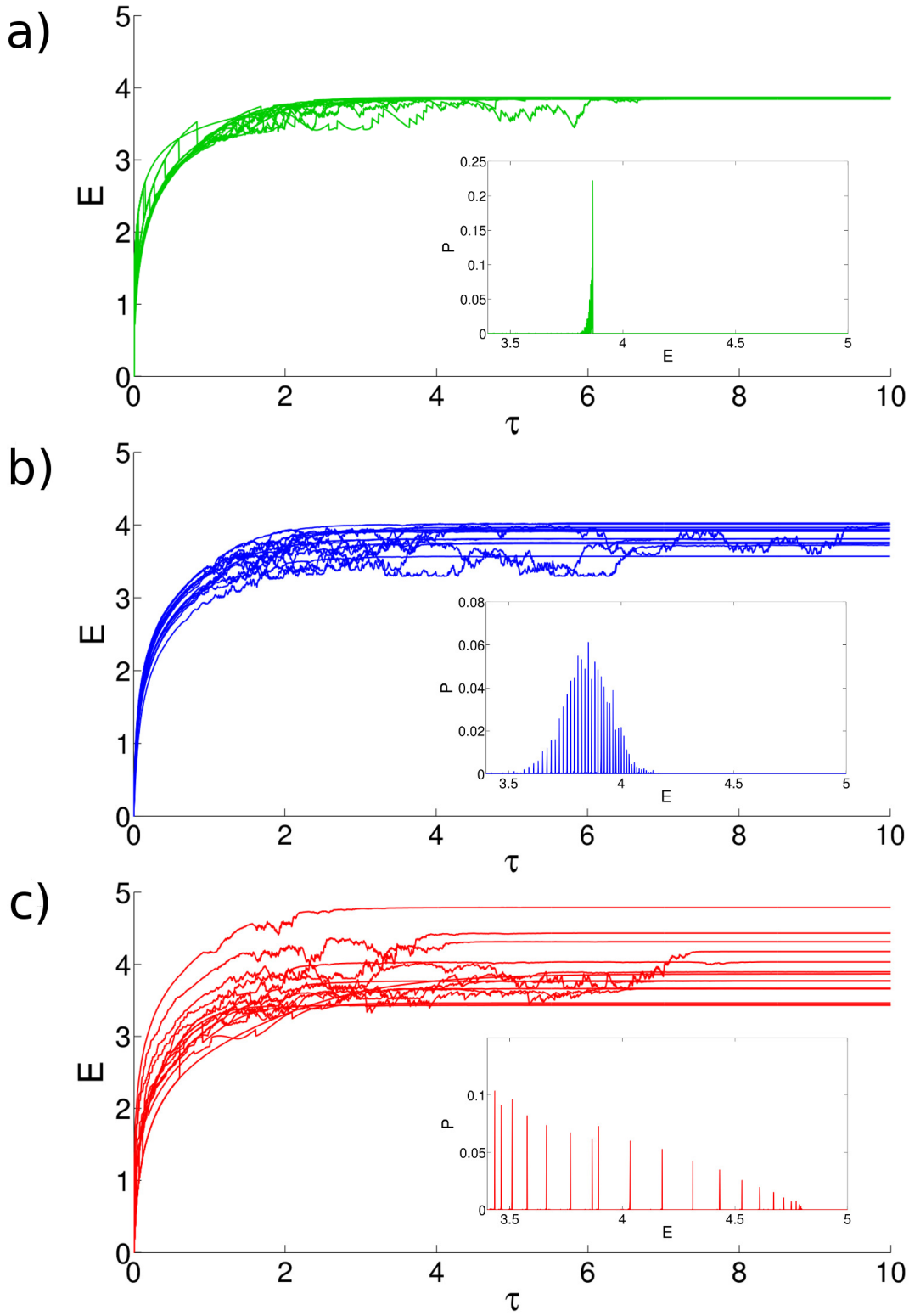

Figure 4.3: **Quantum trajectories showing dynamical growth of entanglement.** Measurement can increase entanglement between two matter modes. Different detection schemes project to different states: (a) phase-sensitive diffraction minimum; (b) diffraction maximum; and (c) phase-insensitive diffraction minimum. Insets show distributions of entanglement for final states. $\langle N \rangle = 50$, $\tau = 2|C|^2\kappa t$.

highest probability to be projected to a state with particularly large entanglement, though the average for all the cases are essentially the same. Interestingly, because of the logarithmic scaling, for large N all three widths become vanishing, and thus for large systems the entanglement effectively converges towards a deterministic value, and hence the outcome of one trajectory would typically be sufficient to study.

4.2.3 Deterministic Generation of Long-Range Entanglement

The non-local nature of the multimode matter structure enables entanglement to be established between several spatially-separated many-body systems, even if they are initially individually in separable Fock states, with no phase coherence between them, through the global nature of the light-matter interactions. In contrast to previous proposals to achieve this, in this scheme it can be done without needing to resort to particle subtraction or particle exchange between systems [162, 163]. Instead, the entanglement is here generated by the introduction of additional sub-modes that span across the individual systems from the global light interactions.

We illustrate this with an example with two subsystems. Begin with two non-overlapping superfluids of fixed atom number N_A and N_B respectively (which may be produced and determined by measuring the $\delta = 0$ light scattering for each of the subsystems). We can define two sub-modes within each subsystem, composed each of the odd and even lattice sites in that superfluid, and hence write the system state in the basis of states labelled by $|N_{(A)}^{(\mathrm{even})}, N_{(A)}^{(\mathrm{odd})}, N_{(B)}^{(\mathrm{even})}, N_{(B)}^{(\mathrm{odd})}\rangle$. A measurement at $\delta = \pi$ across both subsystems then projects to a state with a fixed atom number difference between odd and even sites across both subsystems $(N_{(A)}^{(\mathrm{even})} + N_{(B)}^{(\mathrm{even})}) - (N_{(A)}^{(\mathrm{odd})} + N_{(B)}^{(\mathrm{odd})}) = \Delta N$. The resulting state can be written

$$|\psi\rangle = \frac{1}{\mathcal{N}} \sum_{k=0}^{N_A} \binom{N_A}{k}^{\frac{1}{2}} \binom{N_B}{l(k)}^{\frac{1}{2}} |k, N_A - k, l(k), N_B - l(k)\rangle, \tag{4.12}$$

where $l(k) = (N_A + N_B + \Delta N)/2 - k$.

The state of subsystem A can thus be written

$$\rho_A = \frac{1}{\mathcal{N}^2} \sum_{k=0}^{N_A} \binom{N_A}{k} \binom{N_B}{l(k)} |k, N_A - k\rangle\langle k, N_A - k|. \tag{4.13}$$

As the total state is pure, there is thus entanglement between A and B whenever this reduced state has non-zero entropy, which, because of it being diagonal, occurs whenever there are at least two values of k for which $\binom{N_A}{k}\binom{N_B}{l(k)} \neq 0$. This occurs whenever $|\Delta N| \neq (N_A + N_B)$. As the probability of achieving such an imbalance between odd and even sites quickly becomes vanishing with increasing total number of atoms, this scheme is essentially deterministic in generating entanglement between the two modes. Indeed, this measurement scheme is highly analogous to that of Fig. 4.3(a), but with a different initial state due to the fixed $N_{A,B}$. For the case of $N_A \approx N_B \gg 1$, the initial state has strong overlap with that considered in Fig. 4.3, and so both schemes should produce similar final states. Further, for this $N_A \approx N_B \gg 1$ case, we have typical $\Delta N \leq \mathcal{O}((N_A + N_B)^{1/2}) \ll N_A + N_B$, and hence there will be little spread in the final amount of entanglement, which as before will scale as $\log((N_A + N_B)^{1/2})$. One can see that the scheme also readily generalises to multiple initially disentangled subsystems, by considering the above case, but where one of the subsystems (say B) is a composite of multiple physical subsystems.

4.3 Using the Matter Mode Structure for the Measurement of Entanglement

The nature of the non-trivial spatial overlap of the matter modes may be exploited as a key component in measuring non-linear functions of quantum states. Such functions include purities (and higher moments) of the state, from which properties such as entanglement may be determined. This is done by using the modes as individual non-interacting systems, that can be prepared in identical copies of the same state, this state being some state of interest for measurement. The overlap of modes provides

a straightforward way to implement SWAP and generalised SWAP (permutations) between states, as one need only shift the system along by one site to achieve this.

Moments $\mathrm{Tr}(\rho^m)$ of the density matrix of a state can be determined by acting such generalised SWAP operations on m copies of the state, conditional on the state of an external control qubit [Fig. 4.4(a)], and reading out the average final state of the qubit [164, 165]. Unlike other proposals based on this circuit [166], or other similar schemes involving permutations of multiple copies [137, 167, 168], our scheme readily generalises to arbitrary numbers of dimensions. These moments can be used to measure purities ($m = 2$), as well as the Rényi entropies $H_m(\rho) = \log(\mathrm{Tr}(\rho^m))/(1-m)$. By expanding the appropriate logarithm into a Taylor series of such moments, they can also be used to determine the von Neumann entropy Eq. (2.38), and hence also entanglement entropies Eq. (2.41).

We now provide an example scheme to achieve this. Each virtual lattice supports a copy of the system, prepared in the appropriate many-body state of interest. Two internal states $\{|0\rangle, |1\rangle\}$ of an impurity atom are used as the qubit. We allow one of these states to couple to an incident coherent light source, such that light scatters off the atom and populates a cavity, conditional on the qubit state, and the combined impurity-cavity state may be written $(|0\rangle|0\rangle + |1\rangle|\alpha\rangle)/\sqrt{2}$. The cavity is positioned such that it has spatial overlap with, and thus illuminates, one of the sets of subsystems in the lattice [Fig. 4.4(b)]. The cavity light is then used to drive Rabi transitions in the atoms in this region, such that these atoms are in another internal state. The lattice is chosen such that it is formed from two potentials with equal lattice spacing, one coupling to each of the internal states of the atoms. Akin to the collision gate in optical lattice quantum computing [169] , these potentials are then each shifted by half a site, in opposite directions. This transposition of the atoms effects the desired generalised SWAP gate, and thus the probability of detecting the impurity atom in the state $|1\rangle$ (after performing another Rabi $\pi/2$ pulse on it) then reveals the desired

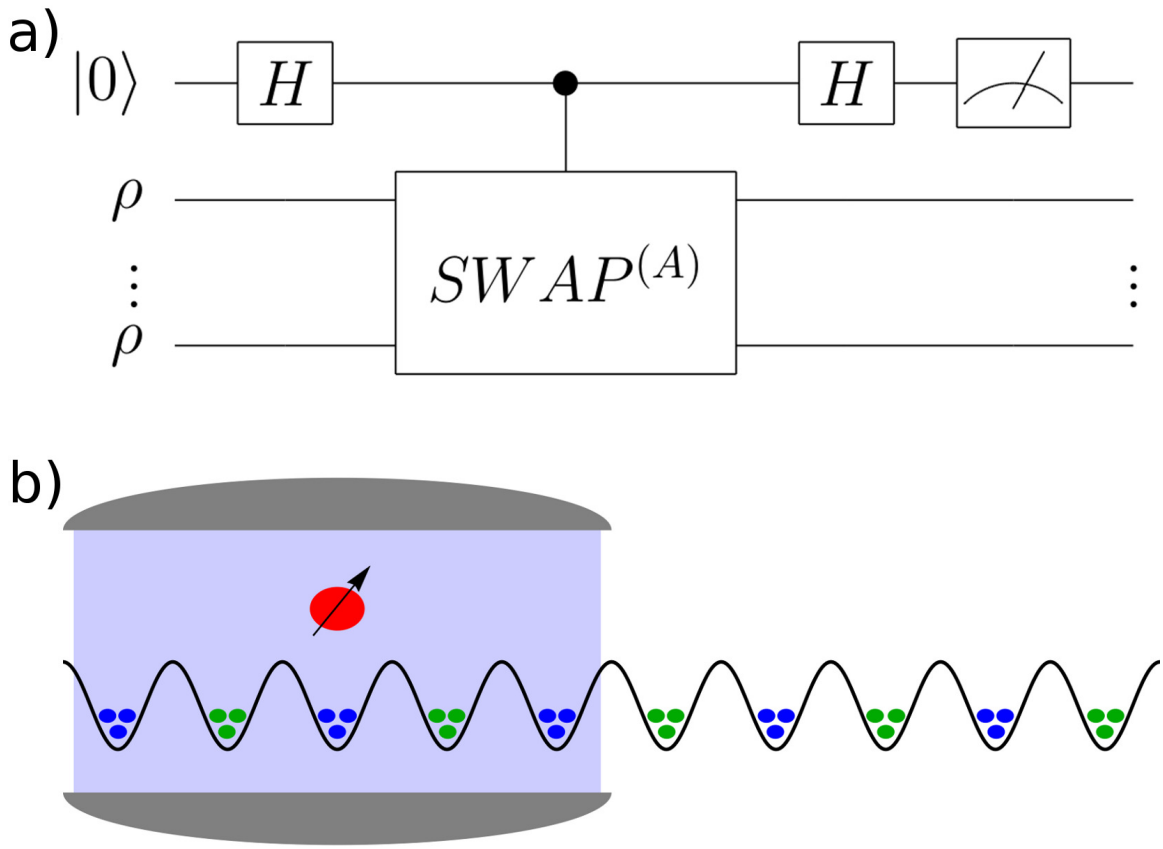

Figure 4.4: **Quantum circuit and scheme for measuring density matrix moments using the matter mode structure.** (a) Generalised SWAP gates of multiple copies of a state, performed conditional on a control qubit state, may be used to extract moments of the density matrix. (b) The matter mode structure, due to the spatial overlap of the modes, provides a suitable arena for performing this circuit. Here, we suggest using an impurity atom as the control qubit. This reveals the entanglement between the illuminated and non-illuminated subsystems.

$\mathrm{Tr}(\rho_A^m)$. From this, we can then hence determine the amount of entanglement between the illuminated and non-illuminated subsystems.

We note that while a full set of moments is needed to precisely determine the entanglement entropy, one can still set lower bounds from the first few moments, and the purity of the reduced density matrix ($m = 2$) is sufficient to verify that entanglement is present, given that the overall state is pure (which can itself be verified by using the scheme to find the purity of the full system) [91]. A similar circuit has also been proposed for the measurement of traces of partially transposed matrices, in which both subsystems undergo the permutations, but in opposite directions [170]. Using these moments one can reconstruct the partially tranposed state, and hence obtain the logarithmic negativity, allowing for the measurement of entanglement in mixed states also. This may be possible using an extension to our scheme, where both subsystems are shifted, in opposite directions.

Chapter 5

Engineering Atomic Dynamics with Quantum Light

The interactions between many-body atomic systems in optical lattices and light in optical cavities induce long-range, correlated atomic processes beyond the standard Bose-Hubbard model, due to the global nature of the light modes. We characterise these processes, which may be tuned by the particular optical geometry, and show that they include effects such as long-range density-density interactions, perfectly-correlated tunnelling, pair exchange, and effective pair creation and annihilation. When united with the dynamical constraints that can be imposed by a strong, projective light measurement backaction through quantum Zeno physics, these novel processes may be selectively tailored, exploiting the additional structure imparted by the quantum light field.

This thus extends the treatment in the previous chapter to also encompass control of the atomic dynamics. We show that this in turn can be exploited to provide a framework for enhancing quantum simulations, where such processes are used to engineer Hamiltonians with long-range and correlated dynamics. We provide building block components for this purpose, including reservoir models such as generalised Dicke models, and dynamical global gauge fields [3].

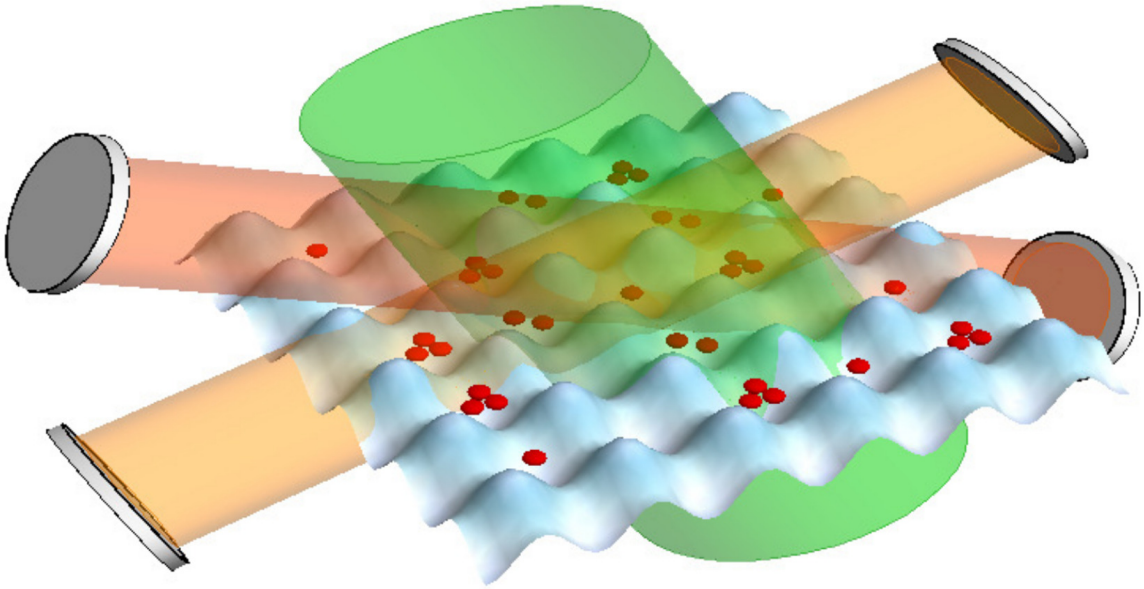

Figure 5.1: **Atomic processes induced and controlled by quantum light.** Ultracold atoms trapped in an optical lattice scatter incident light into optical cavities. The cavity-mediated interactions introduce correlated atomic dynamics that are tunable via the optical geometry. Detection of leaked photons enables a selective suppression of processes, through the measurement backaction effect, allowing for versatile engineering of the atomic dynamics.

5.1 Cavity-Mediated Dynamics

5.1.1 The Model

Our starting point is the generalised Bose-Hubbard Eq. (2.60), describing the interactions due to light scattering from atoms in an optical lattice [Fig. 5.1]. As noted previously, the key component of this Hamiltonian is that both light and atoms are dynamical quantum fields, and it forms the cornerstone of works in the field of fully-quantum many-body light-matter interactions [29, 31].

As explained in Chapter 2, with a single pump mode 0 described by a coherent state of amplitude α_0, with occupation much larger than the cavity modes, we can also describe the cavity modes by coherent states $a_m = C_m \mathcal{J}_{m0}$, where $\mathcal{J}_{mn} = \sum_{ij} J_{ij}^{mn} b_i^\dagger b_j$, and J_{ij}^{mn} and C_m are defined as in Eqs. (2.62) and (2.63) respectively. Using this, a further adiabatic elimination may be performed, to remove the cavity modes. This

approximation requires a cavity decay rate κ_m large compared to the timescales of atomic dynamics, such that the cavity mode rapidly reaches its steady state for the particular atomic configuration. The resulting effective Hamiltonian, describing the atomic dynamics, can thence be written [38]

$$\mathcal{H} = H_{\mathrm{BHM}} + \Omega_{00}|\alpha_0|^2\mathcal{J}_{00} + \sum_{m\neq 0}\frac{\Delta_m|C_m|^2}{2}(\mathcal{J}_{m0}^\dagger\mathcal{J}_{m0} + \mathcal{J}_{m0}\mathcal{J}_{m0}^\dagger), \tag{5.1}$$

where H_{BHM} is the standard Bose-Hubbard Hamiltonian Eq. (2.47), and other symbols are as defined in Chapter 2. The required parameter regime for this cavity backaction to manifest ($\kappa_m \gg J_{ij}^T$) has been achieved in current state-of-the-art experiments [34], where the cavity decay rates κ_m are $\mathcal{O}(10^6\mathrm{Hz})$, compared to the standard Bose-Hubbard tunnelling rate J_{ij}^T $\mathcal{O}(10^3\mathrm{Hz})$ for nearest-neighbour sites.

The additional terms induced by occupation of the cavity modes introduce long-range correlations and interactions between lattice sites. The inclusion of additional pump modes will contribute to the cavity mode populations linearly with the pump 0, and ultimately leads to dynamics of the same form, where instead of the effective Hamiltonian being solely in terms of pump 0, there is instead a sum over all of the pump modes. The choice in the form of the light modefunctions leads to a host of different dynamical setups, and can be tuned by a variety of methods, including changing the wavelength and angle of the lasers, and the angle and size of the cavities. We can see that the presence of a multimode, or even multiple cavities provides even further flexibility beyond a single cavity mode.

We now characterise certain of the cavity-induced processes, focussing on the two dominant contributions, from the on-site and nearest-neighbour inter-site terms. This characterisation is in contrast to previous works that have studied the cavity-mediated processes, which consider them generically as a collective whole, as four-point correlations [50]. However, our characterisation becomes meaningful when we later introduce the measurement backaction as a method to imprint further structure to the lattice that distinguishes between the different processes, and allows them to be selectively tailored.

5.1.2 On-site Terms

Typically, the on-site terms dominate the $\mathcal{J}_{mn}$, due to their having the largest overlap in Wannier functions [29]. When this is the case, one can approximate with the replacement of the light-matter interactions by solely these on-site terms $D_{mn} = \sum_j J_{jj}^{mn} b_j^\dagger b_j$. The coefficients J_{jj}^{m0} appearing in these terms in the effective Hamiltonian Eq. (5.1) may be imprinted with complex phases, through the phase difference of the incoming and outgoing light modefunctions, generating a matter mode structure, as described in Chapter 4, partitioning the lattice into sets of sites scattering light with the same phase [2]. A further level of structure can also be imparted by varying the light intensity across different sites.

We focus first on the special case of illumination at the diffraction maximum ($J_{jj} = 1$), which gives $D_{m0} = N_m$, where N_m is the number of atoms occupying sites illuminated by both the pump and cavity mode m. In this case, the light-induced dynamics is given by

$$\Omega_{00}|\alpha_0|^2 N_0 + \sum_{m\neq 0} \Delta_m |C_m|^2 N_m^2, \tag{5.2}$$

where the first term forms an effective chemical potential, while the second mediates density-density interactions between all of the illuminated sites. These latter interactions occur irrespective of the separation between the lattice sites, and thus exemplify the long-range nature of the cavity-mediated interactions.

With the inclusion of multiple cavity modes, the tunability of these interactions increases, and is enhanced beyond what is possible with merely a single cavity. It allows for short- and long-range interaction strengths to be tuned independently, and is achieved by utilising the relationship between the sign of the cavity detuning and the interaction strength. Chiefly, the sign of the detuning determines whether the interaction is repulsive or attractive, and hence different cavities can have non-equal contributions to the total interaction strength, and can each illuminate different sets of sites.

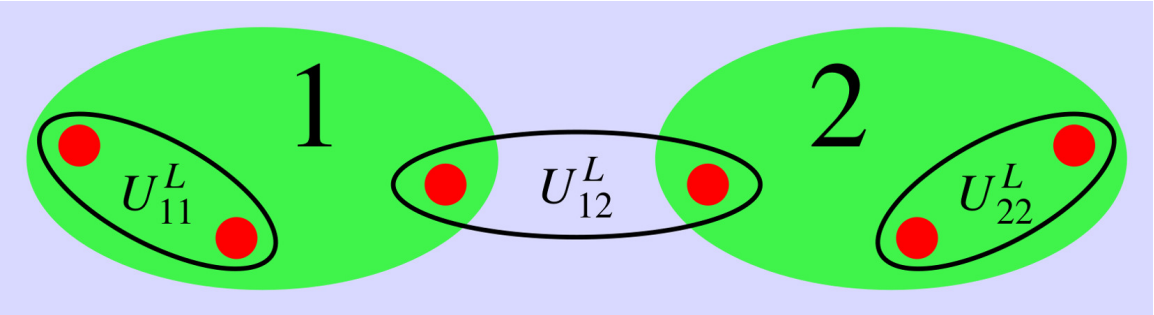

Figure 5.2: **Tunable cavity-mediated density-density interactions.** The strength of the long- and short-range density-density interactions induced by the cavity modes can be tuned independently by use of multiple cavities with different detunings and regions of illumination.

We illustrate this with an example of a system with two illuminated regions [Fig. 5.2], with three cavity modes, labelled X, Y, and Z, that illuminate regions 1, 2, and both respectively, at the diffraction maximum. Denoting the light-mediated density-density interaction strength between particles in regions i and j as U_{ij}^L, we have

$$U_{11}^L = \Delta_X |C_X|^2 + \Delta_Z |C_Z|^2, \tag{5.3a}$$

$$U_{22}^L = \Delta_Y |C_Y|^2 + \Delta_Z |C_Z|^2, \tag{5.3b}$$

$$U_{12}^L = \Delta_Z |C_Z|^2. \tag{5.3c}$$

Thus, each of the three interaction strengths, where the first two govern short-range interactions, and the latter the long-range interactions, may be tuned entirely independently by varying the parameters of each of the three cavities. We note also that in general the regions are defined by the matter mode structure, in turn defined by the J_{jj}^{m0}, and hence need not be spatially contiguous, but rather, may instead have non-trivial spatial structure. In this sense, it perhaps makes more sense in general to consider the interaction strengths as being characterised as intra- and inter-mode, rather than short- and long-range.

For arbitrary illumination patterns, all sites in the illuminated region are part of the resulting density-density interactions, with the general light-induced interaction

strength (due to cavity mode c) between two particular sites or modes A and B given by

$$U_{AB}^{L} = \Delta_c |C_c|^2 \cos(\phi_{AB}^{c}), \tag{5.4}$$

where ϕ_{AB}^{c} is the phase difference between the J_{jj}^{m0} for the two sites/modes. For multiple cavity modes, one simply sums up the contributions from each cavity mode individually, while with multiple pumps one must sum over the C_c generated by each pump, and also consider cross-pump terms in the effective chemical potential.

The effective atomic interactions resulting from such cavity-induced processes have already been demonstrated experimentally for the special case of illumination at the main diffraction minimum [34]. In these experiments, the resulting interactions were of the form $\Delta_c |C_c|^2 (N_c^{(\mathrm{even})} - N_c^{(\mathrm{odd})})$, with the detuning chosen such that this term favours a population imbalance between even and odd states, leading to cavity-induced atomic self-organisation for sufficiently large light-matter interaction strengths. The experiment demonstrated that this interaction strength can be made comparable to, and even stronger than the tunnelling from the standard Bose-Hubbard model by one or two orders of magnitude (i.e. up to $\mathcal{O}(10^4 - 10^5 \mathrm{Hz})$) [34]. As the other more general schemes based on using the on-site terms in the light-matter interaction operator typically involve only changing the phase of the J_{ii}^{mn} through adjustment of the optical geometry, the size of such interaction strengths can be expected to remain of a similar size.

5.1.3 Inter-site Terms

In contrast to the above considerations of on-site terms, when the light modes are arranged to be concentrated between lattice sites the nearest-neighbour inter-site terms in $\mathcal{J}_{mn}$ can become the most significant contribution, with the on-site terms arranged to vanish through symmetry [148]. In this case, the light-matter interactions can be approximated by $B_{mn} = \sum_{\langle ij \rangle} J_{ij}^{mn} b_i^{\dagger} b_j$, which describe light-induced atomic

tunnelling between neighbouring sites. In general, as with the on-site light-induced interaction coefficients, the J_{ij}^{mn} are different for each pair of sites, leading to spatially-dependent tunnelling rates which may be tuned by the optical geometry. However, for the case where the pump intensity $|\alpha_0 u_0(\boldsymbol{r})|^2$ and the lattice sites are commensurate, B_{00} has equal coupling for each nearest-neighbour pair. This allows for the the one-body tunnelling terms to be suppressed or enhanced by the probe light, or potentially even eliminated. In the latter case, one is left with only the two-body interaction terms in the effective Hamiltonian, which themselves can be tuned semi-independently of the one-body terms here used to suppress the tunnelling J_{ij}^T from the standard Bose-Hubbard Hamiltonian.

These two-body processes are of the form

$$\sum_{m\neq 0} \frac{\Delta_m |C_m|^2}{2} \sum_{\langle ij\rangle\langle kl\rangle} (J_{ij}^{m0} J_{kl}^{m0*} b_i^\dagger b_j b_k^\dagger b_l + h.c.), \tag{5.5}$$

where $\{i, j\}$ and $\{k, l\}$ must each be nearest-neighbour site pairs, though the two pairs may be distributed anywhere within the illuminated regions. Each pair corresponds to an atomic tunnelling process, and hence the complete two-body processes correspond to correlated tunnelling events. These events can be characterised according to the relationship between the two site pairs [Fig. 5.3], giving rise to pair tunnelling, pair exchange, effective nearest-neighbour tunnelling, effective pair creation and annihilation, and general long-range correlated tunnelling.

Due to the smaller inter-site overlap of Wannier functions compared to on-site overlaps, the inter-site light-matter coupling coefficients will necessarily be smaller than the on-site coefficients at their respective maxima. Their relative magnitude has previously been studied in [50], where they are shown to typically be separated by approximately an order of magnitude. Thus, the complete two-body correlated tunnelling terms can have a strength approximately two orders of magnitude less than that which may be achieved for the light-induced density-density interactions, and hence can occur at rates comparable to the classical tunnelling J_{ij}^T (i.e. $\mathcal{O}(10^3\text{Hz})$).

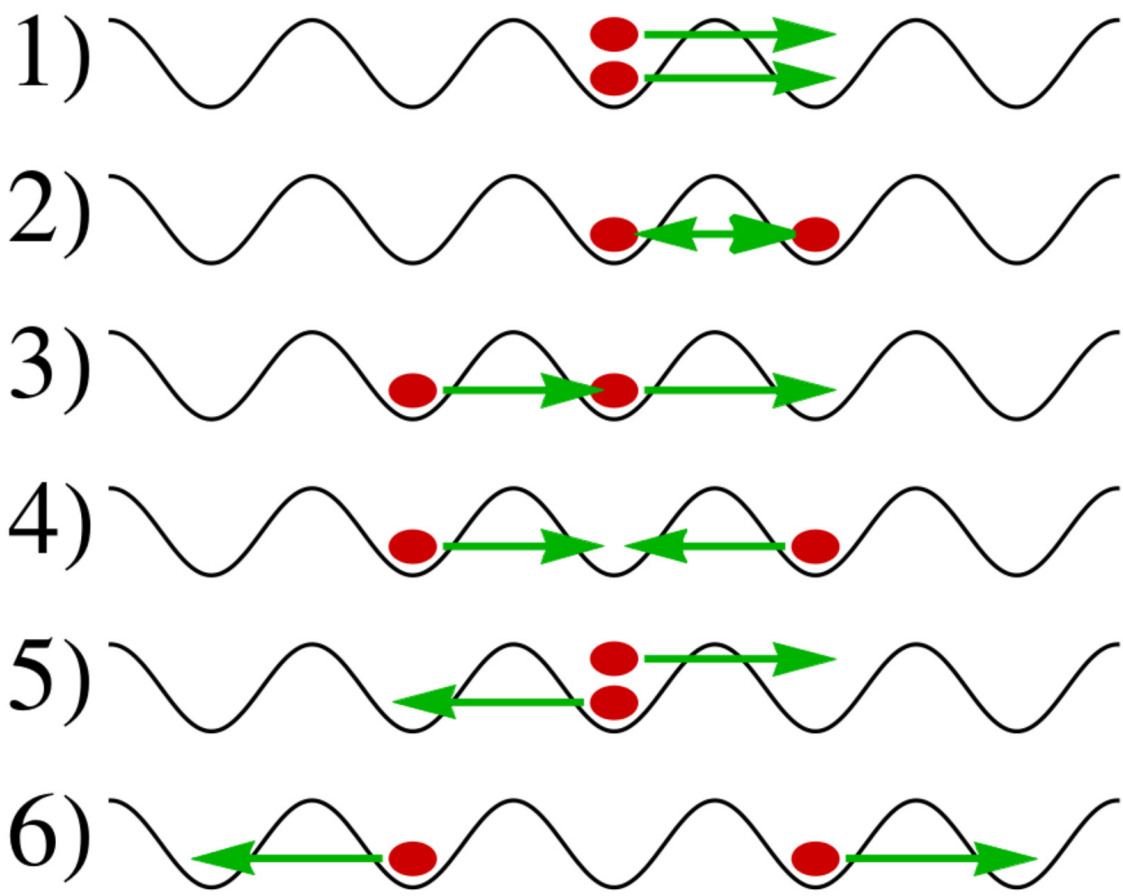

Figure 5.3: **Cavity-induced correlated atomic tunnelling.** The cavities can be used to induce correlated tunnelling processes, which can be classified as: (1) pair tunnelling; (2) pair exchange; (3) effective next-nearest-neighbour tunnelling; (4,5) effective pair creation and annihilation; and (6) general long-range correlated tunnelling.

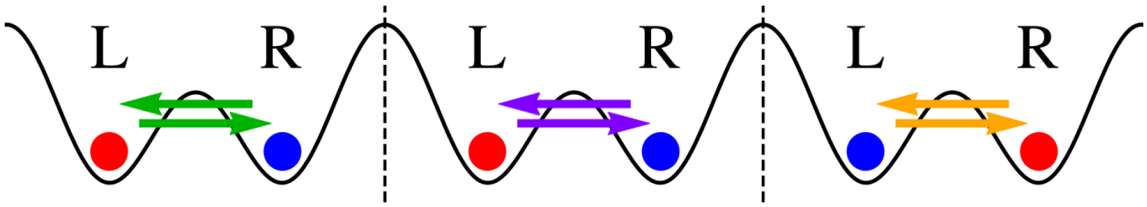

Figure 5.4: **Simulation of superexchange interactions.** A superlattice is used to divide the system into a series of double well potentials, each containing an atom of each of two spin species (denoted by their colour). The superlattice potential and strong repulsive interactions allow only pair exchange processes to take place, between atoms in the same double well, mimicking superexchange dynamics. These correlated tunnellings are indicated by arrows of the same colour.

Even without invoking measurement backaction, it is possible to imprint a further structure to the lattice, and use these processes for quantum simulation purposes. This additional structure can be imparted by shaping the underlying lattice potential to be non-homogeneous, by, for example using a superlattice potential. Previously, two-body atomic tunnelling processes have been used as a way to simulate superexchange interactions in spin models [171]. However, in the original proposal and implementation, the superexchange occurs as a second-order perturbative process. In contrast, the cavity-induced pair exchange processes here, which can be used for the same purpose, are first-order.

Our proposal follows the original by dividing the lattice into pairs of sites with a superlattice potential, such that it is formed of a series of disconnected double wells, with each site pair containing two atoms of different (pseudo)spin species, and a strong repulsive interparticle interaction enforcing a one-particle-per-site constraint. Introducing the correlated tunnelling as above, through use of a single cavity mode c, the resulting dynamics (after imposing the constraints from the superlattice potential and repulsive interactions) permits only the pair exchange processes between atoms in each site pair [Fig. 5.4].

The resulting Hamiltonian describing each double well is thence

$$H_{\mathrm{SE}} = 2\Delta_c |C_c J_{\mathrm{nn}}^{c0}|^2 (b_{L\uparrow}^\dagger b_{R\uparrow} b_{R\downarrow}^\dagger b_{L\downarrow} + h.c.), \tag{5.6}$$

where nn denotes that the sites are nearest-neighbours. This can equivalently be expressed in terms of spin operators, through the mapping $2S_j^Z = b_{j\uparrow}^\dagger b_{j\uparrow} - b_{j\downarrow}^\dagger b_{j\downarrow}$, to give

$$H_{\mathrm{SE}} = J_{\mathrm{ex}}(S_L^+ S_R^- + S_L^- S_R^+), \tag{5.7}$$

where $J_{\mathrm{ex}} = 2\Delta_c |C_c J_{\mathrm{nn}}^{c0}|^2$. Importantly, in contrast to the second-order process in the original proposal, the exchange term here does not suffer a $1/U$ dependence, and hence the interparticle interactions necessary for imposing the constraint on site occupancy can here be implemented without suffering a suppression of the exchange interaction. Indeed, as noted above, these correlated tunnelling processes can occur at rates comparable to the standard tunnelling J_{nn}^T from the classical optical lattice potential.

5.2 Inclusion of Measurement Backaction

A drawback of imparting structure through disruption of the underlying lattice geometry is that it carries the adverse consequence that if a tunnelling event is suppressed as a single event, it is also suppressed when it would otherwise have taken place as part of a correlated event. Instead, measurement can be used to imprint the further structure onto the atoms, without having to suffer this penalty, using the matter mode structure introduced in Chapter 4. The measurement backaction responsible for this structure imposes constraints, and by tuning these constraints, a selective suppression of atomic dynamics can be achieved.

We now apply this formalism to the cavity-induced processes, uniting the cavity and measurement backaction effects, and evince the potential of such a tool for enhancing methods of quantum simulation. Crucially, it allows for a process to be forbidden when taking place as a single event, but permitted when correlated with another particular event (or events), as the suppression is achieved by constraints on the matter mode occupations.

The measurement backaction is realised by using an additional cavity (and possibly pump), for which the scattered light leaked by the cavity is detected. Following the methods discussed in Chapter 4, for an intense continuous measurement of the light state, the freezing by the QZE [63–65] enforces that the atoms are restricted to evolve within a particular subspace of their full Hilbert space, leading to QZD [2,66–68]. The resulting atomic evolution is described by the appropriate Zeno Hamiltonian, obtained by application of Eq. (2.35), using the projectors defining the measurement subspace and the effective atomic Hamiltonian Eq. (5.1).

Thus, light measurement can be used to selectively eliminate particular atomic dynamics, as determined by the measurement cavity geometry. As with the proposal for simulating superexchange interactions, in contrast to earlier work that has used measurement to tailor dynamics of two-body terms [8], in which they occur as second-order processes, such terms here now arise as first-order terms in the evolution, as they are directly induced by the cavity backaction, and are hence perfectly correlated. The two cases are fundamentally different: here, increasing the pump strength increases the two-body tunnelling rates, rather than suppressing them. As noted in Chapter 4, the necessary parameter regime $|C_m|^2\kappa_m \gg J^T_{\mathrm{nn}}$ has not quite yet been achieved in current experiments, but should be feasible in the near future.

As a straightforward example of using Zeno physics with light to engineer atomic dynamics, consider measurement at the diffraction minimum ($J^{m0}_{jj} = (-1)^j$; $D_{m0} = N^{(\mathrm{even})}_m - N^{(\mathrm{odd})}_m$). This freezes the occupation number difference between odd and even sites, preventing nearest-neighbour tunnelling. In the absence of a further cavity driving dynamics, this would leave the next-nearest-neighbour tunnelling as the leading process, which, though it is typically ignored due to it occuring at a much slower rate than the nearest-neighbour tunnelling, is now no longer negligible. With the addition of a cavity driving dynamics, this process can be further augmented with the two-body correlated terms introduced above. Events in which two atoms tunnel into the same site (and the reverse) are forbidden, as are certain long-range

pair tunnelling events, with the allowed processes of the latter form leading to effective long-range tunnelling events within each mode. The pair exchange processes and the effective nearest-neighbour processes are both still permitted by this measurement scheme. The flexibility of the light modes allows for a range of such schemes to be implemented, allowing for different configurations of the two-body processes to be engineered. For example, when light measurement fixes occupation numbers for multiple matter modes [2], the only allowed correlated tunnelling events are pair exchange, and the particular long-range correlated tunnellings that preserve the total mode occupations.

5.3 Framework for Quantum Simulations

This architecture that we have developed naturally lends itself to application in quantum simulations. In particular, it offers opportunities for synthesising correlated processes and long-range interactions that would be difficult (or even impossible) to realise in systems with finite-range interactions. We now provide a framework for this, by introducing and describing some 'building block' components that may be used in the construction of reservoir and dynamical global gauge field models, which can be used to enhance methods of optical lattice quantum simulation.

5.3.1 Reservoir Models

The matter mode structure defined by the light allows the lattice to be partitioned into sites corresponding to each mode. We can assign a subset of these as reservoirs, and investigate the dynamics of the remaining sites. Consider the conceptual three-site model shown in Fig. 5.5(a). In this scenario, a cavity is used to drive dynamics that generate correlated tunnelling events between the sites, such that the system is initially described by

$$\mathcal{H} = H_{\mathrm{BHM}} + \Omega_{00}|\alpha_0|^2 B_{00} + \frac{\Delta_c |C_c|^2}{2}(B_{c0}^\dagger B_{c0} + B_{c0} B_{c0}^\dagger). \tag{5.8}$$

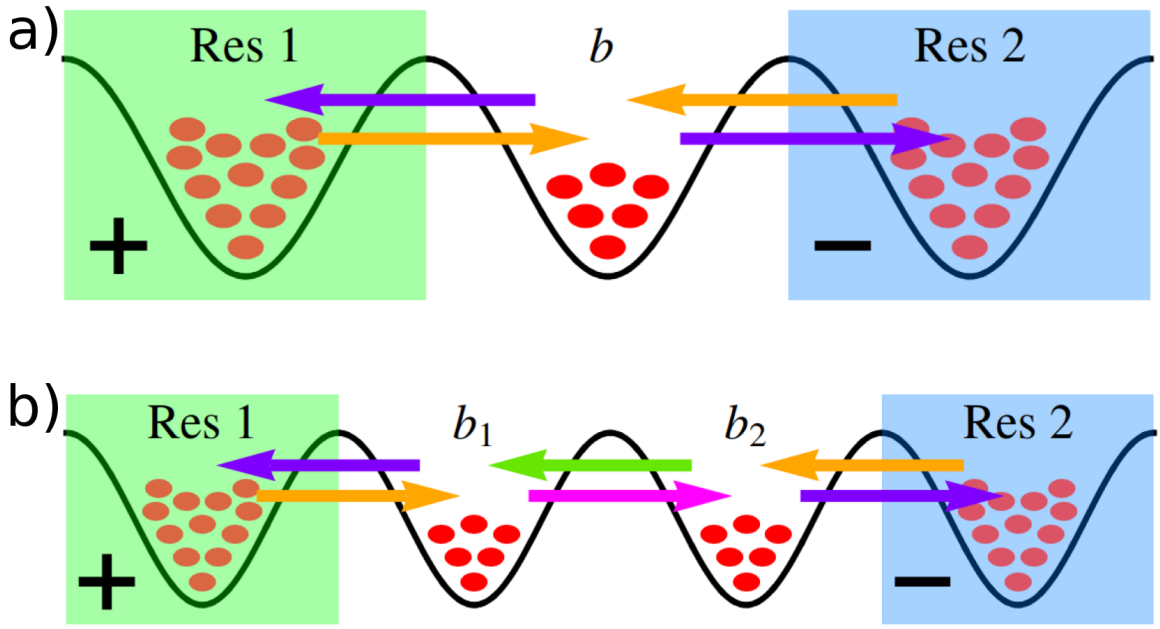

Figure 5.5: **Quantum simulation of reservoir models.** The combination of cavity and measurement backaction can be used to engineer dynamics corresponding to reservoir models for use in quantum simulations. This makes it possible to realise (a) effective pair processes and (b) generalised Dicke models. The highlighting of sites indicates their contribution to the light measurement value (green positive, blue negative; $D = N_{\mathrm{Res1}} - N_{\mathrm{Res2}}$). Tunnelling events that are constrained to only occur together as correlated events are indicated by identically-coloured arrows.

We designate the outer two sites as the reservoirs, taken to be prepared in coherent states $|\beta_{1,2}\rangle$, with light measurement used to fix their occupation number difference $N_{\mathrm{Res1}} - N_{\mathrm{Res2}}$. Such a mode structure for the measurement can be achieved by, for example, illuminating the lattice with two pumps, coherent in antiphase, arranged antisymmetrically about the central site. In this scheme, they then thus interfere fully destructively at this central site, and have opposing contributions at the corresponding site pairs about the central site, resulting in a total pump modefunction $u_0(\boldsymbol{r}) = u_p(\boldsymbol{r}) - u_p(-\boldsymbol{r})$, where u_p are the individual pump modefunctions.

Applying the appropriate projection operators for this measurement scheme (i.e. sets of states with invariant $N_{\mathrm{Res1}} - N_{\mathrm{Res2}}$) to the effective Hamiltonian Eq. (5.8), the dynamics of the central site is thus described by

$$H_{\mathrm{PP}} = (\lambda b^\dagger b^\dagger + h.c.), \tag{5.9}$$

where $\lambda = 2\Delta_c\beta_1\beta_2|C_cJ^{c0}_{\rm nn}|^2$. Note that terms relating to (effective) chemical potentials and on-site interactions have been omitted, as they can be tuned independently by driving additional on-site dynamics. Thus, the two-body terms have here been used to mimic pair creation and annihilation type dynamics for the central site. With the experimental parameters considered above, and for typical occupations $|\beta|^2 \sim \mathcal{O}(1-10)$, these processes can be of a comparable size to the classical tunnelling rate $J^T_{\rm nn}$ (or even slightly larger depending on $|\beta|^2$).

Consider now extending this to include an additional site between the reservoirs, as depicted in Fig. 5.5(b). Again, the measurement is used to fix the occupation number difference of the two reservoirs. This mode structure can be achieved by again interfering coherent pump beams, at different angles such that the total pump modefunction is shaped to be fully destructive at the central two sites, and hence provide a measurement indifferent to their occupation. For such a setup, when the reservoirs have a larger occupation than the central sites, the non-reservoir modes obey a generalised Dicke Hamiltonian [32, 159]:

$$H_{\rm GD} = \mu_1 b_1^\dagger b_1 + \mu_2 b_2^\dagger b_2 + (\lambda_1 b_1^\dagger b_2 + \lambda_2 b_1^\dagger b_2^\dagger + h.c.), \tag{5.10}$$

where, as above, the chemical potentials $\mu_{1,2}$ can be tuned by driving on-site dynamics, and the coupling coefficients

$$\lambda_1 = J^T_{\rm nn} + \Omega_{00}|\alpha_0|^2 J^{00}_{\rm nn}, \tag{5.11a}$$

$$\lambda_2 = 2\beta_1\beta_2\Delta_c|C_cJ^{c0}_{\rm nn}|^2. \tag{5.11b}$$

In contrast to the original model and its corresponding realisation using optical cavities, the parameters $\lambda_{1,2}$, representing co- and counter-rotating terms respectively, can be tuned independently of each other, through the optical geometry. Their magnitude is controlled by e.g. the pump strength and the reservoir populations $\beta_{1,2}$, and complex phases can be induced with additional pump beams driving the dynamics.

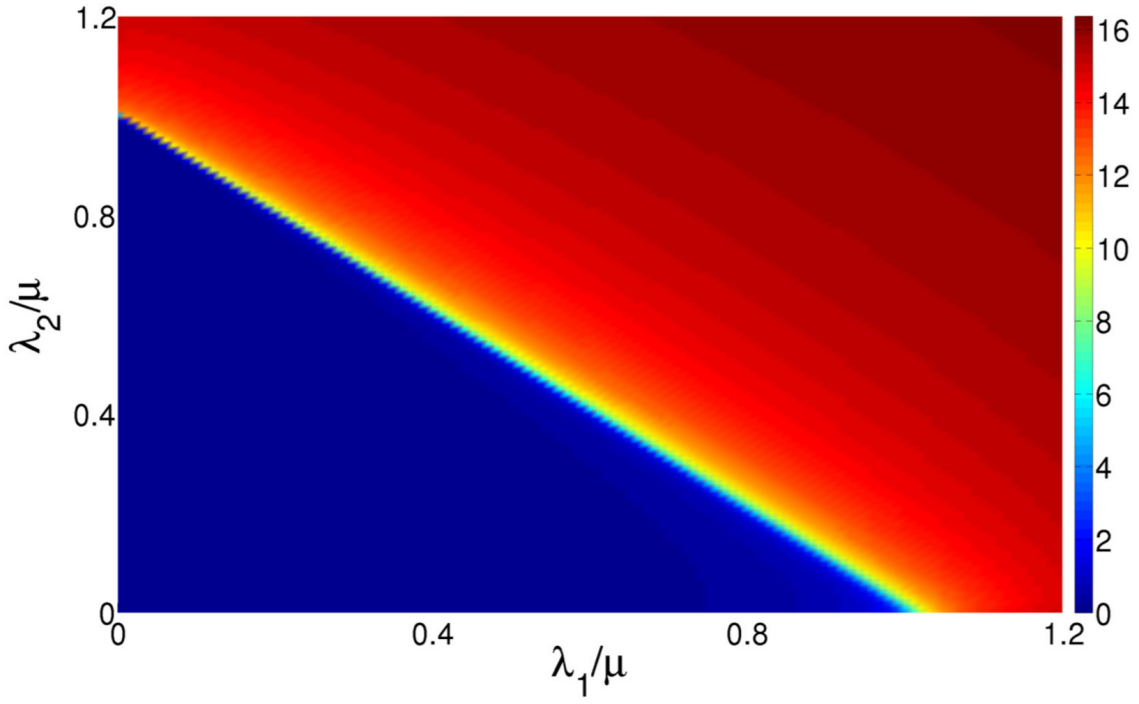

Figure 5.6: **Phase diagram of the generalised Dicke model.** The ground state occupation $\langle b_1^\dagger b_1 \rangle$ for the generalised Dicke model shows a shift in the superradiant phase transition point when varying λ_1/λ_2. Here we find that a general phase boundary is located at $\lambda_1 + \lambda_2 \approx \mu$. Phase diagram is calculated for $\mu_1 = \mu_2 = \mu$, and a maximum occupation of 20 is imposed for each mode.

In addition to the well-known phase diagrams for $\lambda_1 = \lambda_2$ (standard Dicke) and $\lambda_2 = 0$ (Tavis-Cummings) [172], which show superradiance transitions in the quantum case, classical treatments show bifurcations when varying the relative values of $\lambda_{1,2}$ [173], suggesting further novel phase behaviour. Indeed, by using exact diagonalisation to investigate part of the extended parameter space, we see that the phase boundary depends on the values of both parameters (see Fig. 5.6).

This can be further extended by using the light measurement to fix occupation number differences between larger numbers of modes [2], allowing for additional reservoir modes to be generated. These can be used to increase the number of sites coupled to reservoirs, and increase the number of simulated modes in our model (for example, to have multiple synthetic atomic species in our generalised Dicke model). To illustrate a concrete example of how our building block components can be put together to form more complex systems, we now propose how to realise a generalised Dicke model with two synthetic atomic species, and one synthetic light mode.

Consider an amalgamation of two copies of the above setup for the one-species generalised Dicke model Eq. (5.10), crossed perpendicularly such that both sites share a common site for the synthetic light mode [Fig. 5.7]. As before, cavities are used to induce the correlated tunnelling dynamics, one for each of the constituent setups. Using also two measurement cavities, each fixing the difference in occupation of the reservoir modes in one of the setups, the resulting Zeno Hamiltonian is

$$H_{2-\mathrm{GD}} = \sum_{j=A,B,L} \mu_j b_j^\dagger b_j + \sum_{j=A,B} (\lambda_1^{(j)} b_j^\dagger b_L + \lambda_2^{(j)} b_j^\dagger b_L^\dagger + h.c.), \tag{5.12}$$

where L indicates the synthetic light mode, A and B are the synthetic atomic species, and the $\lambda_{1,2}^{(j)}$ are of the same form as for the one-species setup Eqs. (5.11) with the appropriate coefficients $\beta_{1,2}$, Δ_c, C_c and J_{nn}^{c0} as defined for each of the individual setups.

Yet more exotic setups can be envisaged with this framework, through the use of additional reservoirs, or with multiple sites connecting to common reservoirs. In

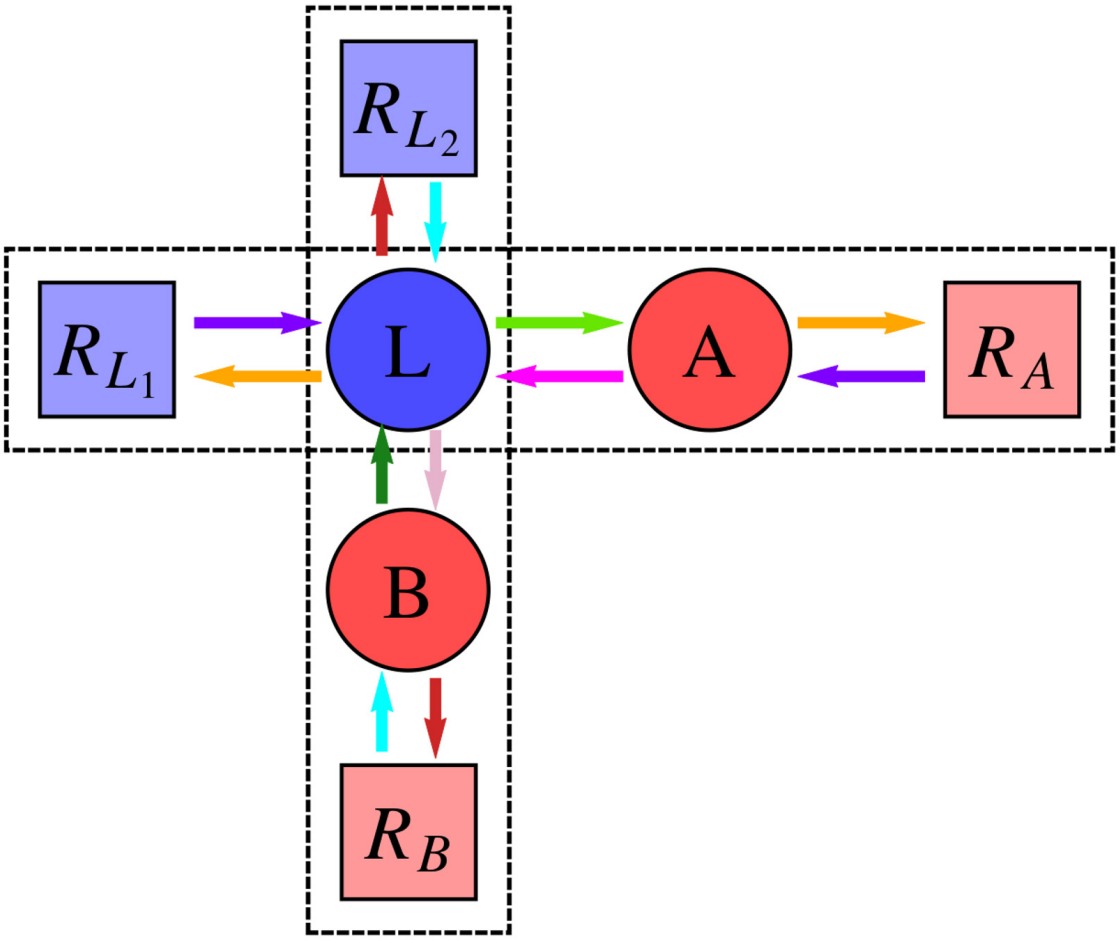

Figure 5.7: **Schematic for the two-species generalised Dicke model.** Combining two copies of the setup for the one-species generalised Dicke model with a mutual synthetic light mode enables the introduction of another atomic species. Circles represent the synthetic modes, and squares the reservoirs. Measurements of the occupation differences $R_{L_1} - R_A$ and $R_{L_2} - R_B$ correlate certain tunnelling events, as indicated by arrows of the same colour.

the extreme case of each site in a simulated system being coupled to two reservoirs (i.e. a lattice of copies of the setup in Fig. 5.5(a)), one would obtain a Bose-Hubbard model with additional pair creation/annihilation effects. Beyond this, and perhaps more straightforward to realise experimentally, one can consider when every site is connected to the same two reservoir modes, with fixed occupation number difference, which results in a Hamiltonian with global pair creation/annihilation:

$$H_{\mathrm{PP-BHM}} = -J\sum_{\langle ij\rangle} b_i^\dagger b_j + \frac{U}{2}\sum_i b_i^\dagger b_i^\dagger b_i b_i + \sum_{ij}(\lambda b_i^\dagger b_j^\dagger + h.c.). \tag{5.13}$$

5.3.2 Dynamical Global Gauge Fields

Another application of this framework for quantum simulations is in the synthesis of artificial dynamical gauge fields. Current proposals to this end also typically employ ultracold atoms in optical lattices, focussing on local gauge fields based on quantum link models [174–176], with changes in the gauge field due to the motion of matter simulated by the motion of another particle species that plays the role of the gauge field [79,177,178]. In addition to the possibility of extending the variety of such models by incorporating the long-range interactions, the introduction of cavity-mediated dynamics presents a further opportunity: the long-range nature of the interactions allows for the correlated atomic motion to itself be long-range, and hence the links need not be local. As such, this paves the way for realising global dynamical gauge fields, where motion across all sites is controlled by a common link.

For example, consider a one-dimensional lattice, with light measurement of a site-dependent strength. Specifically, (by e.g. using a gradiated intensity of the measurement pump), the measured light state has an amplitude that is proportional to $\sum_j j\Upsilon N_j$, for some constant Υ. We consider two auxiliary sites L and R between which atoms can tunnel (and with tunnelling out of this pair suppressed), which are also measured in the same fashion, contributing an effective ΥN_R (plus constant) to the measurement value due to the conserved total value of $N_L + N_R$. In this case,

sites L and R can be seen to form a link that mediates the dynamics in the rest of the lattice, as the Zeno Hamiltonian will then only contain the dynamics from the cavity-mediated correlated tunnelling events, where an atom tunnels in the main lattice simultaneously with a tunnelling event either in the link, or in the opposite direction in the main lattice.

The resulting Hamiltonian is

$$H_{\mathrm{DGGF}} = \sum_j (\lambda b_j^\dagger b_{j+1} (\sum_k b_{k+1}^\dagger b_k + \vartheta b_L^\dagger b_R) + h.c.) + (\lambda \vartheta^2 b_L^\dagger b_R b_R^\dagger b_L + h.c.), \quad (5.14)$$

where $\lambda = \Delta_c |C_c J_{\mathrm{nn}}^{c0}|^2$, and ϑ^2 is the ratio of the intensity of the pump used to drive the dynamics at the link sites compared to the rest of the lattice. Equivalently, by mapping the link to a spin with $2S^Z = N_L - N_R$, this can be written

$$H_{\mathrm{DGGF}} = \sum_j (\lambda b_j^\dagger b_{j+1} (\sum_k b_{k+1}^\dagger b_k + \vartheta S^+) + h.c.) - 2\lambda \vartheta^2 (S^Z)^2. \quad (5.15)$$

This forms a global-link dynamical matter-gauge field interaction, in contrast to the current proposals that are restricted to local-links by their finite-range interactions. Strictly, we note that pair-correlated tunnelling events are allowed within the main lattice independent of the link, provided that they occur in opposite directions, though the particle current across the lattice is wholly dependent on the link. These terms bypassing the link can also be made less significant by adjustment of ϑ, which also provides one route for tuning the gauge field energy terms $(S^Z)^2$. These gauge field energy terms can also be further engineered through tuning of the density-density interactions and effective chemical potentials as discussed above. Unlike the local-link models ubiquitous in high-energy physics, the common global-link here leads to the peculiar effect where the motion of a particle at any site can significantly affect the field experienced by all other particles, at all sites.

Chapter 6

Quantum quasi-Zeno Dynamics

Frequent observation of a quantum system leads to Zeno physics, where the system is constrained to evolve within the subspace of states consistent with the measurement outcome [63–68]. Such effects have been demonstrated experimentally [179–185], and there has been a great deal of interest in studying their use in state engineering, measurement-based control of a system, and the related field of designed dissipation [2, 3, 8, 45, 147, 178, 186–201]. It has been shown that even when consecutive measurements are finitely spaced in time, the locking to a measurement subspace can still occur [202]. However, in this case, the description of the system evolution solely in terms of this subspace is incomplete [203]; the finite time between measurements allows higher-order processes to occur, where the system first transitions away from the measurement subspace, and then subsequently back in to it before the next measurement occurs, thus preserving the value of the measured observable.

We demonstrate how these higher-order processes, which we term quantum quasi-Zeno dynamics (QqZD), arise from perturbative considerations of standard QZD. We derive effective Hamiltonians to describe the evolution of the system in this regime, and suggest that such processes should be interpreted as virtual transitions, and draw visual analogy with Feynman diagrams. We provide a simple illustrative example using a three-level system, which could form the basis of a future experimental verification of the work. We then extend the formalism to encompass time-dependent

Hamiltonians, non-equally and stochastically spaced measurements, and discuss how transitions to different measurement subspaces may be incorporated. We then demonstrate application of this phenomenon to two archetypal examples of many-body systems, spin chains and atoms in optical lattices, where we show that the higher-order processes may facilitate the manifestation of correlated dynamics in the system [4].

6.1 Fundamentals of Quantum quasi-Zeno Dynamics

To study the consequences of short but finite time between measurements, we consider the effects of the terms higher-order in δt that were neglected in the derivation of standard QZD in Eqs. (2.33)-(2.35). Consider a system with Hamiltonian H, thus undergoing an associated evolution $U(t) = \exp(-iHt)$. When subjected to a measurement of observable A, with associated operator $A = \sum_m A_m \mathcal{P}_m$, we can describe the associated evolution of an initial state ρ due to two measurements a time δt apart as (neglecting normalisation)

$$\rho \to \mathcal{P}_f U(\delta t)\mathcal{P}_i \rho \mathcal{P}_i U^\dagger(\delta t)\mathcal{P}_f, \tag{6.1}$$

where the projectors correspond to initial and final measurement outcomes A_i and A_f respectively.

When $A_i = A_f$, the normalisation of Eq. (6.1) corresponds to Eq.(2.33), the probability of the measurement value being unchanged. For small times (i.e. $H\delta t \ll 1$), we can expand $U(\delta t)$, to obtain the probability of the measurement outcome changing. The probability of a transition from outcome A_i to A_f is given by

$$P(A_f|A_i) = \frac{\mathrm{Tr}(\mathcal{P}_f H \mathcal{P}_i \rho \mathcal{P}_i H)\delta t^2}{\mathrm{Tr}(\mathcal{P}_i \rho)} + \mathcal{O}(\delta t^3). \tag{6.2}$$

By defining for a subspace $\mathcal{P}$ the associated complement $\mathcal{Q} = \mathbb{I} - \mathcal{P}$, we can thus write the total probability of a system transitioning out of a given state ρ in initial measurement subspace $\mathcal{P}$:

$$P_{\mathrm{trans}} = \mathrm{Tr}(\mathcal{Q}H\rho H)\delta t^2 + \mathcal{O}(\delta t^3). \tag{6.3}$$

The 'Zeno-locking' condition, that the measurement subspace should have negligible probability of changing, can be used with this expression to set an upper limit on the timescales on which we can say we are near the Zeno regime. Specifically, we require that $P_{\text{trans}} \ll 1$ for any state ρ in subspace $\mathcal{P}$. From here, we assume that this condition is met. Note that unlike the strong measurement backaction case considered in the previous two chapters, it is here important that the result of each measurement is known, as there is now a finite probability of transitioning out of the measurement subspace, and we will need to know when this occurs.

Before deriving the corrections to the effective evolution beyond standard QZD, we first clarify and justify some assumptions and approximations made. Firstly, we model the system as evolving under unitary evolution between measurements. Such evolution is true in general for an isolated, closed quantum system. Appealing to the so-called church of higher Hilbert space (CHHS) [16], an ancilla may be appended to a system to account for the effect of an environment, such that the total system-ancilla is closed, and hence has unitary evolution, even if the system dynamics alone does not. If the measurement outcome depends only on the system state, and is independent of the ancilla, then the inclusion of the ancilla does not affect the QqZD result: one simply has to trace out the ancilla from the QqZD evolution in the same manner as usual for recovering the system dynamics from a CHHS treatment. A second simplification made is that we treat the measurements as von Neumann projective measurements. This is in keeping with the standard simple derivations of the QZE and QZD [63, 68], which have subsequently been extended to more generally account for the coupling to external 'measurement devices' [204]. These treatments recover the standard results when the time taken for the measurement device to operate is much shorter than the system dynamics. It has also been shown that Zeno physics can still persist even when measurements are not perfectly projective [202]. Thus, we expect that even when such realistic concerns are incorporated into our treatment, the results should be preserved.

We can write the combined evolution of the system evolving under its Hamiltonian H for time δt followed by a projective measurement to subspace $\mathcal{P}$ as (ignoring normalisation)

$$\rho \to U_1(\delta t)\rho U_1^\dagger(\delta t), \tag{6.4}$$

where we define $U_1(\delta t) = \mathcal{P}U(\delta t)$. Following N such sets of evolution and measurement taking place in a time $\tau = N\delta t$, with each measurement outcome in the same subspace $\mathcal{P}$, the system evolution (again neglecting normalisation) is given by

$$\rho \to U_N(\delta t)\rho U_N^\dagger(\delta t), \tag{6.5}$$

where $U_N(\delta t) = U_1(\delta t)^N$. Expanding the $U(\delta t)$ as a power series, we arrive at Eq.(2.34), except we now preserve higher-order terms. We focus on the leading correction:

$$U_N(\delta t) = \left(\mathcal{P}\left(1 - iH\delta t - H^2\frac{\delta t^2}{2} + \mathcal{O}(\delta t^3)\right)\right)^N \tag{6.6}$$

In the full QZD limit, taking $\delta t \to 0$ and $N \to \infty$, this becomes exactly the evolution under the Zeno Hamiltonian, which we will now denote $H_Z^{(1)} = \mathcal{P}H\mathcal{P}$. Close to, but outside of this limit, we can still approximately describe the evolution by an exponential. The corrections can be found by examining the difference between the exact evolution and the evolution under $H_Z^{(1)}$. Specifically, focussing on the δt^2 term in the expansion, we see that in the exact evolution we have $-\mathcal{P}H^2\mathcal{P}\delta t^2/2$, whereas the Zeno Hamiltonian gives $-{H_Z^{(1)}}^2\delta t^2/2$. We use the difference between these two as our definition of the second-order quasi-Zeno Hamiltonian $H_Z^{(2)} = \mathcal{P}H\mathcal{Q}H\mathcal{P}$. Moreover, we define the general quasi-Zeno Hamiltonian as:

$$H_Z^{(k)} = \mathcal{P}H(\mathcal{Q}H)^{k-1}\mathcal{P}. \tag{6.7}$$

We see that the first-order quasi-Zeno Hamiltonian is then exactly the Zeno Hamiltonian of QZD. Further, we construct an approximate effective Hamiltonian accounting for these higher-order corrections:

$$H_{\text{eff}} = \sum_{k=1}^{\infty} \frac{(-i\delta t)^{k-1}}{k!} H_Z^{(k)}, \tag{6.8}$$

with an associated effective evolution operator and equation

$$U_{\text{eff}}(\tau) = e^{-iH_{\text{eff}}\tau} \tag{6.9a}$$

$$\rho \to U_{\text{eff}}(\tau)\rho U_{\text{eff}}^{\dagger}(\tau). \tag{6.9b}$$

Thus, the kth-order quasi-Zeno Hamiltonian mediates kth-order transitions, where the initial and final states are in the measurement subspace $\mathcal{P}$, but the intermediate states are not. Because of the dependence of each quasi-Zeno Hamiltonian's contribution to the effective Hamiltonian on increasing powers of δt, each one is less significant than that of the previous order, and the intimate dependence of QqZD on the measurement timestep is evident. Indeed, given that the probability of the measurement outcome belonging to a different subspace scales as δt^2, the second-order quasi-Zeno Hamiltonian is likely to be the only significant correction in practice.

Heuristically, we can see that since both the transition probability and the second-order quasi-Zeno Hamiltonian have similar magnitude $\sim \text{Tr}(\mathcal{P}H\mathcal{Q}H\mathcal{P}\rho)\delta t^2$, the QqZD correction within a given subspace is of the same order as the probability to transition out of the subspace Thus, provided we are in the regime for which QqZD is valid (i.e. this quantity is much less than unity), the relative magnitude of the correction to the state at the time at which a transition ultimately occurs is approximately independent of δt. The size of δt is still relevant however, as it governs the accuracy of the approximate effective evolution operator (more accurate for smaller δt), the size of the correction due to the higher-order quasi-Zeno Hamiltonians (decreasing with δt), and the total timescales over which the QqZD evolution takes place (longer for smaller δt). Note that the standard Zeno dynamics takes place on timescales independent of δt. Because the QqZD correction is of a similar magnitude to the transition probability, the quasi-Zeno deviation can become very non-neglible especially when one considers long experimental runs, such as those where the measurement subspace changes during the trajectory (see Section 6.3).

In the standard QZD regime, the effective Hamiltonian is simply the Zeno Hamiltonian $H_Z^{(1)}$, which, being Hermitian, leads to unitary dynamics. Contrastingly, the quasi-Zeno Hamiltonians are alternatively Hermitian and anti-Hermitian, and thus due to the second-order quasi-Zeno Hamiltonian $H_Z^{(2)}$ being non-vanishing for any non-trivial Hamiltonian and measurement operator when δt is finite, in the quasi-Zeno regime the dynamics is non-unitary. Instead, the dynamics of the system will tend towards the eigenstate(s) of $H_Z^{(2)}$ with lowest eigenvalue that can be accessed by the dynamics from the (quasi-)Zeno Hamiltonians, and the decay in the norm of the state corresponds to the survival probability of remaining in the measurement subspace.

From the above, we have that the probability of a transition out of the measurement subspace between times t and $t + \delta t$ is given by

$$\begin{aligned} P(\bar{\mathcal{P}}, t) &= \mathrm{Tr}(H\rho(t)H(\mathbb{I} - \mathcal{P}))\delta t^2 + \mathcal{O}(\delta t^3) \\ &\approx \mathrm{Tr}(H_Z^{(2)}\rho(t))\delta t^2. \end{aligned} \tag{6.10}$$

Thus, the total survival probability of remaining in the initial measurement subspace after N measurements is given by $\prod_{n=1}^{N}(1 - P(\bar{\mathcal{P}}, n\delta t)$. For long times, the survival probability will tend to zero, unless there is a state space which satisfies $\mathrm{Tr}(H_Z^{(2)}\rho) = 0$. The second-order quasi-Zeno evolution causes the system to tend towards this state, effecting a 'natural selection' of states, removing those for which the survival probability is lower, tending towards a steady state space. More generally, the evolution tends towards effective steady states which minimise the rate of higher-order processes the system undergoes, and hence those with the largest survival probability. Such effective steady states are fragile, as they have a non-zero transition probability, and so for longer times will eventually transition out of the measurement subspace.

6.2 Interpretation and Example

Physically, the QqZD second-order terms involve a small but finite occupation of an intermediate state between measurements, which is then removed by the projection of the subsequent measurement, provided that the locking of the measurement eigenvalue is maintained. While there is an occupation of this intermediate state between measurements, it can transition to other states that are accessible to it in the non-measurement case. These transitions can either be to states also outside of the measurement subspace (occupation of which is then removed by the next measurement), or back into the original measurement subspace, though not necessarily the original state, in which it may remain after the next measurement. Higher-order terms involve transitions with additional intermediate states. When the time between measurements decreases, the maximum amplitude for occupation of the intermediate states is also lessened, and hence the rate of transitions out of these states will be attenuated. This is reflected in the form of the effective Hamiltonians and their dependence on δt. In the infinitely-frequent measurement limit of QZD, there is no occupation of the intermediate states, and thus there are no transitions beyond first-order.

Because of the locking to the measurement subspace, occupation of the intermediate states is never directly observed. However, through the occurence of transitions that take place via these states, their temporary occupation may be indirectly inferred. As a result of this, and because the dynamics can be described by effective Hamiltonians acting only on the measurement subspace (allowing a description of the intermediate states to be omitted), intermediate states outside of the measurement subspace can be viewed as virtual states, and consequently, transitions between states in the measurement subspace that take place via such virtual states can be seen as virtual processes. Similar effects occuring with continuous non-projective measurement have been compared with Raman-like processes [8, 205].

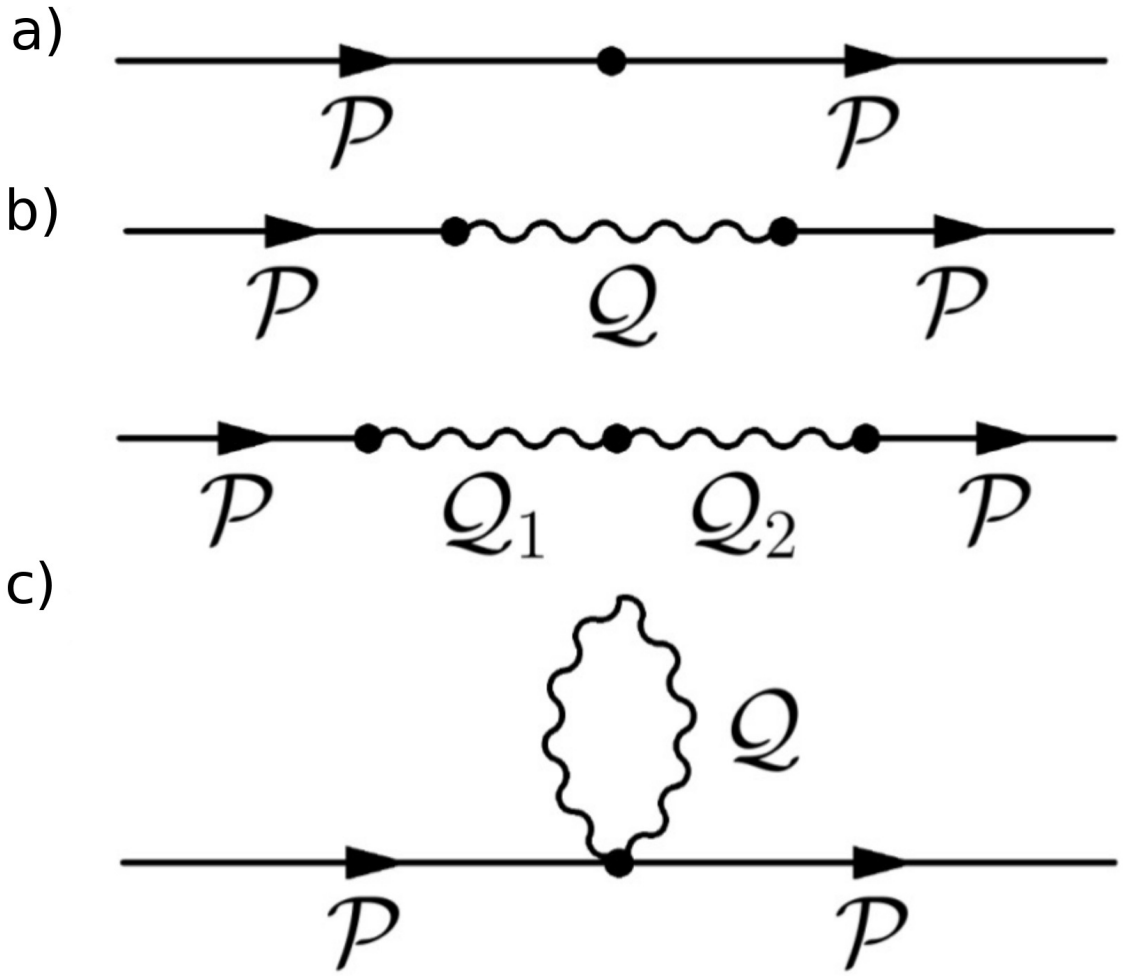

Figure 6.1: **Transitions via virtual processes.** The quasi-Zeno Hamiltonians mediate transitions that occur via states outside of the measurement subspace, which can be viewed as virtual processes. These can be compared with Feynman diagrams, where instead of interactions occuring via virtual particles, we instead represent transitions occuring via the occupation of intermediate virtual states. Single vertex processes (a) are described by the standard Zeno Hamiltonian $H_Z^{(1)}$, while higher-order processes (b) with n vertices and $n-1$ virtual states are mediated by the quasi-Zeno Hamiltonian $H_Z^{(n)}$. Transitions to a virtual state and back into the initial state can be represented by loop diagrams (c), akin to the representation of self-interaction with Feynman diagrams.

We can draw a visual analogy between these virtual processes and Feynman diagrams [Fig. 6.1]. Feynman diagrams [15], used as pictorial representations of interactions in high-energy physics, depict interactions as being mediated by virtual particles. We can construct a similar picture for the virtual processes of QqZD, where the incoming and outgoing lines are the initial and final states in the measurement subspace, the vertices are the transitions between states, and the internal lines correspond to occupation of the intermediate states. In this representation, the number of vertices corresponds to the number of transitions, and hence the order of the quasi-Zeno process; transitions described by the Zeno Hamiltonian $H_Z^{(1)}$ have one vertex and no virtual states (as they do not require occupation of the intermediate states), whilst transitions from the second-order quasi-Zeno Hamiltonian $H_Z^{(2)}$ are represented by two vertices and one virtual state. Second-order processes that return back to the same initial state can be considered akin to self-interacting processes, giving rise to self-energy type contributions in the effective Hamiltonian. We note that this analogy is purely intended as a graphical aid to interpret the transitions within the QqZD framework, and we do not propose that the mathematics of the processes typically represented by Feynman diagrams be directly mapped onto QqZD.

To further illustrate these virtual processes, we present a very basic toy model consisting of the simplest system that can exhibit non-trivial QqZD: a three-state system where two states possess a degenerate measurement eigenvalue. Consider such a three-state system (such as a spin-1 particle), where we label the states $\{|1\rangle, |2\rangle, |3\rangle\}$. The system Hamiltonian is such that there are transitions with strength J_{12} between states $|1\rangle$ and $|2\rangle$, and with strength J_{23} between states $|2\rangle$ and $|3\rangle$:

$$H = J_{12}|2\rangle\langle 1| + J_{23}|3\rangle\langle 2| + h.c. = \begin{pmatrix} 0 & J_{12}^* & 0 \\ J_{12} & 0 & J_{23}^* \\ 0 & J_{23} & 0 \end{pmatrix}. \tag{6.11}$$

Using our spin analogy, in the case where $J_{12} = J_{23}$ this would correspond to the application of a transverse field. A frequent measurement is made, which interrogates

whether the system is in state $|2\rangle$, and thus the corresponding projectors are $|2\rangle\langle 2|$ and $|1\rangle\langle 1|+|3\rangle\langle 3|$. The Hamiltonian contains no direct transitions between states $|1\rangle$ and $|3\rangle$, and thus in such a setup in the standard QZD scenario the Zeno Hamiltonian vanishes: $H_Z^{(1)} = 0$ and there is no dynamics. However, for measurements that are finitely frequently spaced, as in the QqZD regime presented here, the second-order quasi-Zeno Hamiltonian for the latter measurement subspace takes the form

$$\begin{aligned} H_Z^{(2)} &= |J_{12}|^2|1\rangle\langle 1| + J_{12}J_{23}|3\rangle\langle 1| + J_{12}^*J_{23}^*|1\rangle\langle 3| + |J_{23}|^2|3\rangle\langle 3| \\ &= \begin{pmatrix} |J_{12}|^2 & J_{12}^*J_{23}^* \\ J_{12}J_{23} & |J_{23}|^2 \end{pmatrix}, \end{aligned} \tag{6.12}$$

and hence allows transitions between states $|1\rangle$ and $|3\rangle$, by sequentially undergoing two transitions, to and from state $|2\rangle$, while this intermediate state is never observed to be occupied, and thus the transition appears as a virtual process. We see also the occurence of effective self-energy terms, from the $|1\rangle \to |2\rangle \to |1\rangle$ and $|3\rangle \to |2\rangle \to |3\rangle$ transitions.

This simple example can be straightforwardly solved to find the steady state to which QqZD drives the system. For $J_{12} = J_{23} = J = J^*$, the eigenvalues of Eq. (6.12) are 0 and $2\lambda^2$, with associated eigenstates $|-\rangle = (|1\rangle - |3\rangle)/\sqrt{2}$ and $|+\rangle = (|1\rangle + |3\rangle)/\sqrt{2}$ respectively. Thus, according to standard QZD, a system initialised in the state $|1\rangle = (|+\rangle + |-\rangle)/\sqrt{2}$ subject to such a measurement will remain in this state, while in contrast QqZD predicts the system evolution to be $(\exp(-\lambda^2 t\delta t)|+\rangle + |-\rangle)/\sqrt{2}$, the decay in the norm representing the probability to remain in the measurement subspace. Thus, according to QqZD, the long-term evolution of the system is towards the state $|-\rangle$, provided the system remains in the same measurement subspace, which occurs with probability 1/2. Interestingly, this final state is a dark state of the original Hamiltonian ($H|-\rangle = 0$), and hence once this steady state is reached, the system will remain in it even if the measurement is no longer performed.

As three-level systems are routinely realised in a variety of experimental setups, this example may also provide a useful schematic for an initial experimental demonstration of QqZD. Standard QZE and QZD have been tested and observed in a wide range of different experimental setups, including ions [179], photons [180], nuclear spins [181], atoms in microwave cavities [183], Bose-Einstein condensates [182, 184], and ultracold gases in an optical lattice [185]. Thus, there are a wealth of possible candidate systems one could consider for an experimental verification of QqZD. An experimental realisation of this regime would potentially be less taxing than similar experiments of standard QZE and QZD, as the requirement on the time between measurements is less stringent. Possible obstacles for such an experiment are the need to maintain the coherence of the system for sufficiently long times to witness the higher-order effects, and that for verification of these effects, a second observable must be measured at the start and end of the protocol that can distinguish between states in the measurement subspace.

6.3 Further Generalisations

In the above, we took the time between measurements to be equal for simplicity. The generalisation to non-equal timesteps between measurements is straightforward. The form of the quasi-Zeno Hamiltonians are unchanged, but the dependence on δt now leads to varying strengths of their contribution to the evolution between each measurement. We can modify the effective evolution to account for this by including a product over effective evolutions for all the different measurement timesteps. Taking δt_j as the time between measurements $j-1$ and j, with $\sum_{j=1}^{N} \delta t_j = \tau$, this can be written

$$U_{\text{eff}}(\tau) = \prod_{j=1}^{N} e^{\sum_{k=1}^{\infty} \frac{(-i\delta t_j)^k}{k!} H_Z^{(k)}}. \tag{6.13}$$

Considering only the terms up to $\mathcal{O}(\delta t)$ in the total evolution, we can neglect those arising from the non-commutativity of the effective Hamiltonians for different

timesteps as they occur at higher-order, suppressed by a factor $\delta t_j - \delta t_{j'}$, and hence approximate

$$U_{\text{eff}} = e^{-iH_Z^{(1)}\tau - \sum_{j=1}^{N} H_Z^{(2)} \frac{\delta t_j^2}{2}}. \tag{6.14}$$

With the evolution written explicitly in terms of each measurement timestep, we can also clearly see how time-dependent Hamiltonians may be incorporated into the formalism, in the case where they are approximately piecewise constant between subsequent measurements. To do so, we generalise the definition of the quasi-Zeno Hamiltonians to be $H_Z^{(k)}(t) = \mathcal{P}H(t)(\mathcal{Q}H(t))^{k-1}\mathcal{P}$ in the above effective evolution, and impose appropriate time-ordering. This generalisation also allows for systems where the measurement timestep depends on a stochastic process (for example, the decay of a particle) to be described. If the variance in the timesteps for such a process is sufficiently narrow, an 'average' trajectory may be considered by calculating the moments $\langle \delta t^k \rangle$, with an average number of measurements $\langle N \rangle = \tau / \langle \delta t \rangle$.

Thus far, we have taken the measurement outcomes to be constant. However, it is possible to relax this condition, while still in the limit where measurement occurs much more frequently than changes in the measurement outcome, and describe the system evolution by a straightforward extension to the QqZD formalism. Between changes in the measurement value, the system is described by the appropriate QqZD effective evolution operator for the subspace. When the measurement eigenvalue changes, from a value corresponding to the subspace with projector $\mathcal{P}$ to that of the subspace with projector $\mathcal{P}'$, the change in the state is

$$\rho \to \mathcal{P}' H \mathcal{P} \rho \mathcal{P} H \mathcal{P}', \tag{6.15}$$

from the leading term $\mathcal{O}(\delta t)$ allowing transitions out of the measurement subspace. After the measurement, the system is again described by a QqZD effective evolution operator, but now that corresponding to the new subspace. In an experimental run, one can simply determine when such a change in subspace occurs by observing when the measurement outcome changes.

6.4 Application to Many-Body Systems

Many-body systems often possess interesting properties that are described by observables dependant on the collective state of multiple particles. Different configurations of particles can still result in the same system-wide measurement value for this observable, and such configurations hence correspond to the same measurement subspace. This makes many-body systems a suitable arena for QqZD, and we shall here provide examples of QqZD in many-body systems, along with the associated observables, and show how this can lead to correlated dynamics.

6.4.1 Spin Chains

For the first example, we consider an array of spins in a chain [102], where each pair of neighbouring spins is coupled by an exchange interaction $S_j^+ S_{j+1}^-$, such that the full system Hamiltonian is

$$H = -J \sum_{\langle ij \rangle} S_i^+ S_j^- \tag{6.16}$$

where J is the coupling strength of the interaction and $\langle ij \rangle$ again indicates that i and j are neighbouring sites. We take the total magnetisation (the sum of S^Z values) of a set of sites as our measurement, such that the subspaces are defined by sets of states with the same magnetisation in this region (see Fig. 6.2(a)). Dynamics changing this magnetisation are forbidden by the Zeno-locking, and thus the standard Zeno Hamiltonian contains only spin-exchange between neighbouring spins with either both, or neither, in the measured regions.

However, the higher-order quasi-Zeno Hamiltonians mediate correlated spin-exchange events, where multiple pairs of spins flip approximately simultaneously between measurements, conserving the total magnetisation measured. The second-order quasi-Zeno Hamiltonian can be written

$$H_Z^{(2)} = J^2 \sum_{\substack{\langle i \in \mathcal{A}, j \in \mathcal{B} \rangle \\ \langle k \in \mathcal{A}, l \in \mathcal{B} \rangle}} (S_i^+ S_j^- S_k^- S_l^+ + S_i^- S_j^+ S_k^+ S_l^-). \tag{6.17}$$

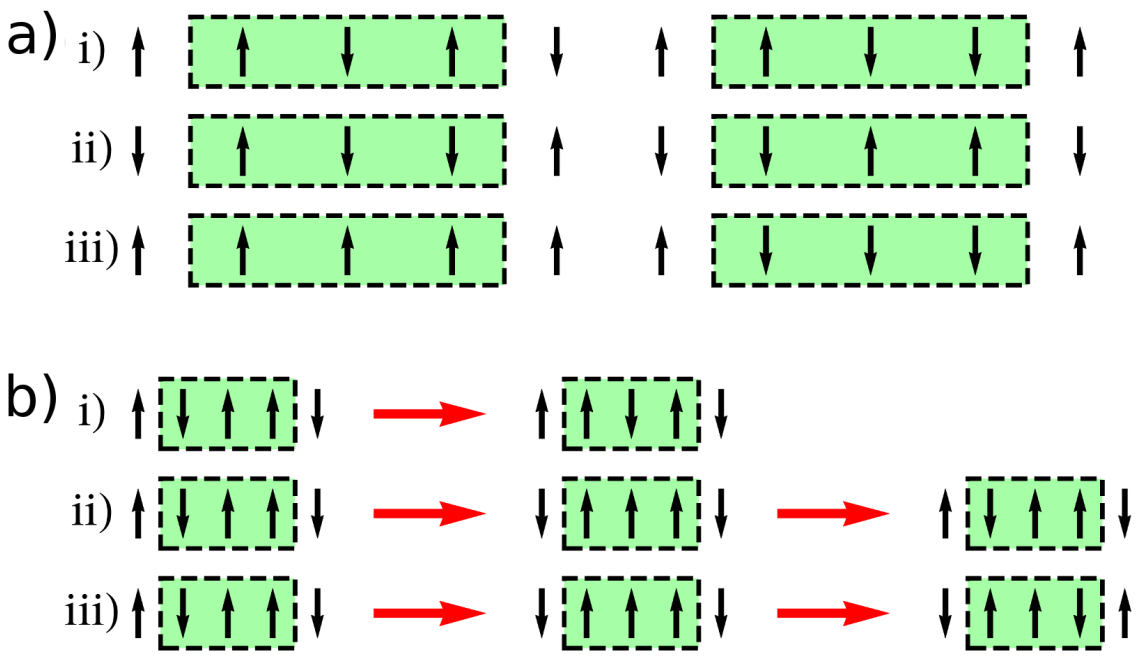

Figure 6.2: **Correlated processes in spin chains.** Multiple configurations of spins (a) belong to the same measurement subspace. Processes that ultimately preserve the measurement value can take place, at (b*i*) first- or (b*ii,iii*)higher-order. Here, the measurement value is given by the total magnetisation of the green regions.

This mediates two such correlated exchanges, involving only pairs that straddle the boundaries of the measured $\mathcal{A}$ and unmeasured $\mathcal{B}$ regions. These processes can be classed in two forms: in the first, both exchanges happen between the same pair, but in opposite directions, thus leaving the individual spins unchanged; in the second, the two pairs are distinct, with one exchange increasing the total magnetisation of the measured region, while the other decreases it. These processes are illustrated in Fig. 6.2(b). In the latter case, there is no restriction on the spatial separation of the two pairs, and hence these processes can be correlated over long distances; this then resembles a superexchange interaction [103, 104], but with the potential for a larger separation between the pairs.

6.4.2 Atoms in Optical Lattices

Analogous processes can be mediated for atoms in an optical lattice. Consider the state-of-the-art systems we earlier studied, where optical cavities are introduced to

the system, which allow for linear functions of the site occupation numbers to be measured. We investigate the scenario where atoms behaving according to the Bose-Hubbard model Eq. (2.47) are subject to such measurement. This measurement will restrict the allowed tunnelling events, forbidding those that change the measurement value, and correlating sets of tunnelling events that together preserve it. In Fig. 6.3(a) we illustrate how measuring the total occupation of a central region mediates long-range correlated tunnelling events across the boundaries of the region. The Zeno Hamiltonian is given by

$$H_Z^{(1)} = -J(\sum_{\langle i\in\mathcal{A},j\in\mathcal{A}\rangle} b_i^\dagger b_j + \sum_{\langle i\in\mathcal{B},j\in\mathcal{B}\rangle} b_i^\dagger b_j) + U\sum_i b_i^\dagger b_i^\dagger b_i b_i, \tag{6.18}$$

while the second-order quasi-Zeno Hamiltonian is given by

$$H_Z^{(2)} = J^2 \sum_{\substack{\langle i\in\mathcal{A},j\in\mathcal{B}\rangle \\ \langle k\in\mathcal{B},l\in\mathcal{A}\rangle}} (b_i^\dagger b_j b_k^\dagger b_l + b_j^\dagger b_i b_l^\dagger b_k), \tag{6.19}$$

where $\mathcal{A}$ and $\mathcal{B}$ again represent the measured and unmeasured regions respectively. Terms where $\{i,j\}$ and $\{l,k\}$ are identical can be re-expressed as chemical potential and density-density interaction terms $J^2(2n_in_j + n_i + n_j)$.

We can also consider a scenario where the difference in occupation numbers of particular sites is measured. This is illustrated in Fig. 6.3(b). In this case, we define three regions: $\mathcal{A}$ measured, with a positive contribution; $\mathcal{B}$ unmeasured; and $\mathcal{C}$ measured, with a negative contribution. The Zeno Hamiltonian is then

$$H_Z^{(1)} = -J(\sum_{\langle i\in\mathcal{A},j\in\mathcal{A}\rangle} b_i^\dagger b_j + \sum_{\langle i\in\mathcal{B},j\in\mathcal{B}\rangle} b_i^\dagger b_j + \sum_{\langle i\in\mathcal{C},j\in\mathcal{C}\rangle} b_i^\dagger b_j) + U\sum_i b_i^\dagger b_i^\dagger b_i b_i, \tag{6.20}$$

and the second-order quasi-Zeno Hamiltonian

$$H_Z^{(2)} = J^2(\sum_{\substack{\langle i\in\mathcal{A},j\in\mathcal{B}\rangle \\ \langle k\in\mathcal{C},l\in\mathcal{B}\rangle}} b_i^\dagger b_j b_k^\dagger b_l + \sum_{\substack{\langle i\in\mathcal{A},j\in\mathcal{B}\rangle \\ \langle k\in\mathcal{B},l\in\mathcal{A}\rangle}} b_i^\dagger b_j b_k^\dagger b_l + \sum_{\substack{\langle i\in\mathcal{B},j\in\mathcal{C}\rangle \\ \langle k\in\mathcal{C},l\in\mathcal{B}\rangle}} b_i^\dagger b_j b_k^\dagger b_l + \sum_{\substack{\langle i\in\mathcal{A},j\in\mathcal{C}\rangle \\ \langle k\in\mathcal{C},l\in\mathcal{A}\rangle}} b_i^\dagger b_j b_k^\dagger b_l + h.c.). \tag{6.21}$$

In $H_Z^{(2)}$, the first term mediates pair-process like effects, where two particles either enter or leave the unmeasured region approximately simultaneously. The other terms

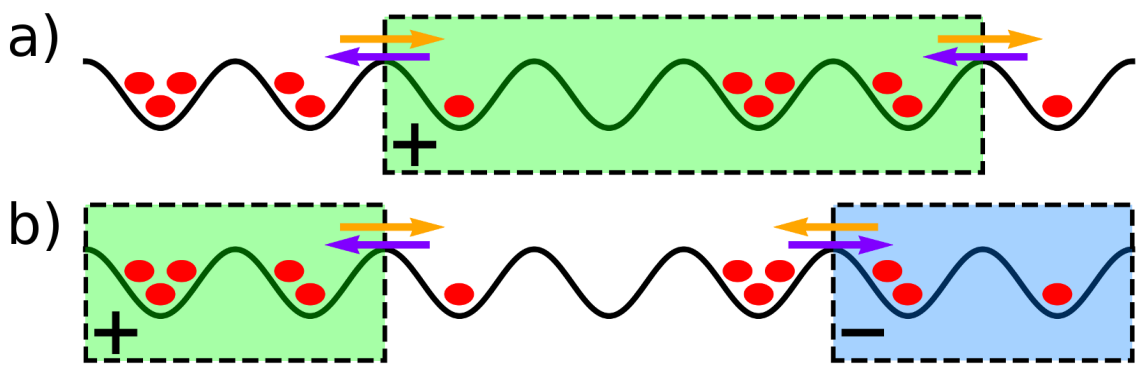

Figure 6.3: **Correlated atomic processes.** (a) Frequent, consistent measurement of the occupation of a set of sites facilitates correlated tunnelling of atoms over the boundaries of the measured region, while (b) measuring occupation number differences gives rise to pair process-like effects. Coloured boxes indicated the measured regions and their contributions (green positive, blue negative), and arrows the same colour indicate correlated tunnelling events.

correspond to the simultaneous crossing in opposite directions of two particles across the boundaries of each pairing of regions.

We use a small-scale simulation to demonstrate these effects, with the scheme of Eqs. (6.18) and (6.19). This simulation is for two atoms distributed across four lattice sites, with the total occupation of the two central sites measured, and fixed at $N_2 + N_3 = 1$. We take a measurement timestep $\delta t J = 10^{-2}$, well within the Zeno-locking regime, and consider no direct interparticle interactions: $U = 0$. We calculate the evolution of the system for the QqZD effective Hamiltonian, the exact evolution, and the standard QZD evolution on a trajectory where the measurement outcome is unchanging [Fig. 6.4]. We see that there is a very close agreement between the effective (a) and exact evolution (c), as shown by their difference (d). They exhibit the tunnelling between the central sites (as per standard QZD), as well as the transfer of atoms mediated by the quasi-Zeno dynamics between the two outer sites due to correlated tunnelling, and the convergence to a (set of) steady state(s). In contrast, the standard QZD evolution (e) completely fails to capture the correlated tunnelling and convergence to a steady state, showing only the tunnelling between the central sites. We also show (b) the survival probability for the system to remain in the

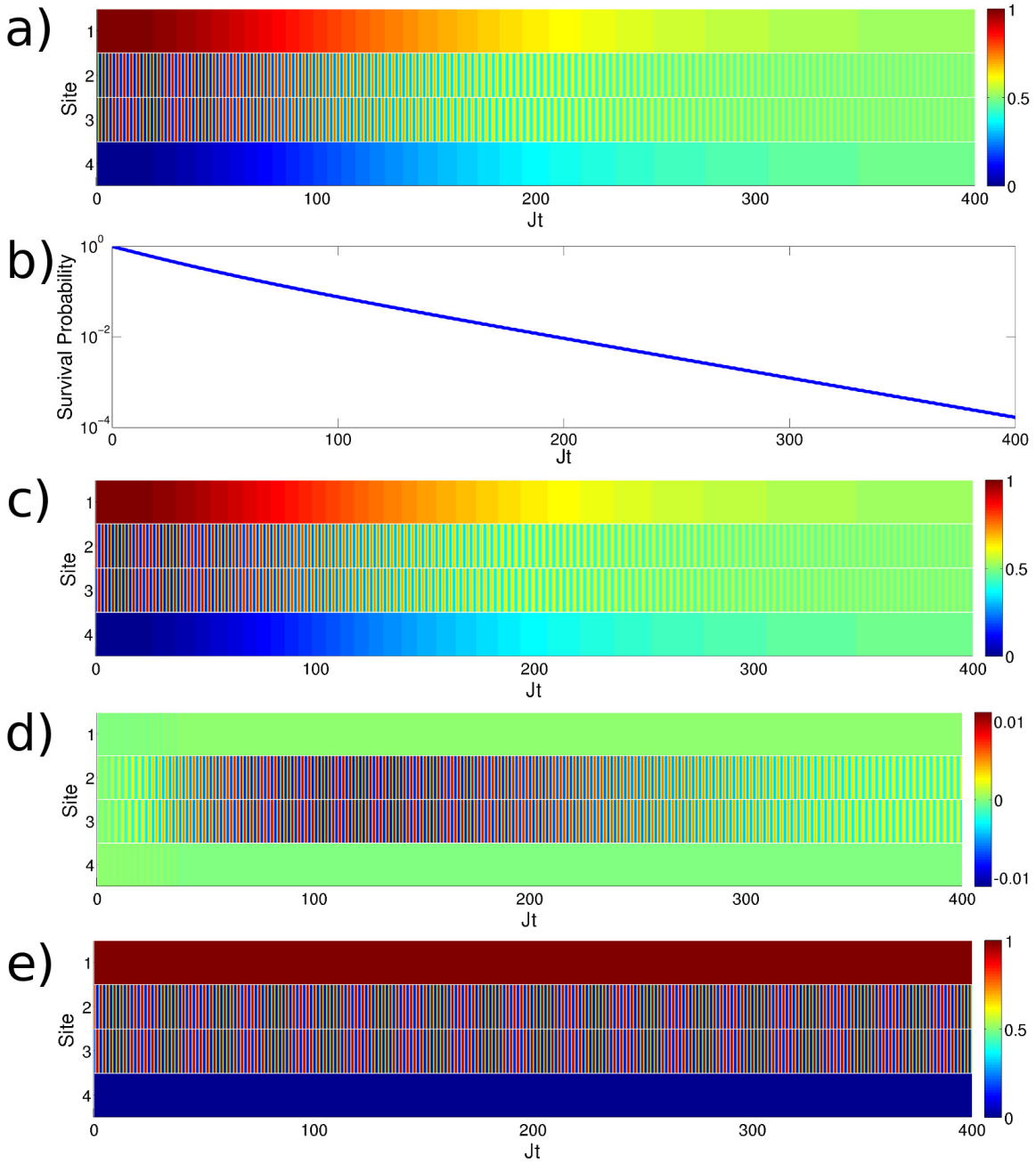

Figure 6.4: **Simulation of correlated many-body dynamics**: (a) Simulation of an effective Hamiltonian for atoms in an optical lattice, for the scheme of Eqs. (6.18) and (6.19) and Fig. 6.3(a), showing first- and second-order processes. Colour map shows average site occupation. (b) Survival probability for the system to remain in the same Zeno subspace. (c) Exact evolution of the same system. (d) Difference between results for exact and effective evolution; the primary error is in capturing the first-order dynamics, and scales linearly with δt (see main text). (e) Evolution under the Zeno Hamiltonian of QZD for the same system fails to capture the correlated processes. Simulations use 4 sites, 2 atoms, $\delta t J = 10^{-2}$, $U = 0$, with measurement imposing the constraint $N_2 + N_3 = 1$. Initial state $|1, 1, 0, 0\rangle$.

Zeno subspace; we see that while the full convergence to the steady state takes a long time (with such trajectories occuring with low probability), the additional quasi-Zeno dynamics can still take place on timescales for which Zeno-locking is maintained with a high probability. The lower probability to reach the steady state (in comparison to the three-state example given in Section 6.2) is in part because of the competition between the first- and second-order dynamics, as the system can be in states for which (second-order) quasi-Zeno dynamics do not take place (e.g. $|1,1,0,0\rangle$), but leakage from the measurement subspace still can; the standard Zeno dynamics causes transitions between such states and the states for which the quasi-Zeno dynamics do take place (e.g. $|1,0,1,0\rangle$).

The primary quantitative disagreement between the exact and approximate effective evolution is in capturing the first-order processes. This is because of the discrepancy between the exact binomial series, and the approximate effective exponential power series. Naively, one can argue this error to be $\mathcal{O}({H_Z^{(1)}}^2 t\delta t)$ (up to a maximum of the largest occupation of the site), because for each quasi-Zeno Hamiltonian the discrepancy is in its associated second-order term in the evolution, thus making the Zeno Hamiltonian $H_Z^{(1)}$ responsible for the primary level of error. However, the convergence to a steady-state supresses the dynamics, and so curtails this error to some maximum value due to the damping of the accessible state space in time by $H_Z^{(2)}$.

Chapter 7

Conclusion

We conclude this thesis with a summary of the main results found, and provide an outlook for future work building upon them. We also comment on the prospects for experimental implementations of the protocols discussed.

- In Chapter 3 we introduced a new protocol for measuring moments of an operator that describes the coupling between two systems. This protocol enables properties of one system to be inferred by measurements solely on the other. We provided a specific system in which this protocol would find use, wherein the system of interest is an ultracold quantum gas, the ancillary measured system is an impurity atom, and the moments determined are of the system density (and corresponding variances and correlations), as unlike current methods, the protocol can be non-destructive. We demonstrated the feasibility of the protocol for this application by simulating such an experiment using realistic parameters.

  As discussed in the chapter itself, the most obvious extension to this work would be to find further system-probe interactions that can be implemented with the protocol, and we suggested some such specific examples, namely, spin-sensitive density coupling to determine magnetisations, probes with periodic density to measure momentum densities, and density-dependent tunnelling to measure currents. Other possible routes for extension include finding applications of the protocol to other systems, and considering ancilliary measurement systems

beyond qubits; with regards to the latter point, a recent proposal [206] that may find promising use here has considered replacing the control qubit with a continuous-variable quantum mode, which may lead to yet further properties of the system that may be measured.

- In Chapter 4 we demonstrated how light modes can be used to imprint a multimode structure onto atomic systems, beyond simple lattice trapping potentials. We showed that when these light modes are quantum fields, for instance when in a cavity, then detection of these light fields can be used to mould the state of the atoms according to this structure. We presented as particular examples of this state engineering how multimode analogues of down-conversion, squeezing, and Dicke states could be produced, in addition to showing how long-range atomic entanglement could be generated deterministically by light measurement. We also proposed how the multimode matter structure could be purposed to detect and measure entanglement between atomic modes.

  As we only covered a subset of the possible measurement schemes that can be implemented by adjusting the highly flexible optical geometry, this treatment can be extended further, to consider other light modefunctions, and engineer additional types of states. The use of the matter mode structure to partition the physical lattice into multiple non-interacting systems might also potentially be used further, for example, to measure other non-linear functions of a state beyond entanglement and entropies. Beyond this, an evident further application of the matter mode structure is for engineering the atomic dynamics, as we introduced in Chapter 5.

- In Chapter 5 we investigated the effective dynamical processes induced in the atoms by their interaction with the light in optical cavities. We characterised the processes, which include long-range density-density interactions and correlated tunnelling events. We exploited the matter mode structure as a way to control

and tune these dynamical processes, and thus proposed how the cavity-induced processes may be used to synthesise desirable atomic dynamics for quantum simulation. We provided a series of building block components using these ideas, such as reservoir models and dynamical gauge fields, that can be pieced together to form increasingly complex Hamiltonians.

Further work building on this could go down several routes. The first would be to investigate other dynamical processes that can be induced by the cavity backaction. Thus far we have not considered the interplay between the on-site and inter-site terms, in the case where both such terms are non-neglible. Such cross-terms may be expected to lead to long-range density-dependent tunnelling type interactions. Another route would be to expand the building block bestiary to include additional effects that can be incorporated. Alternatively, one could proceed further by putting the building blocks together to form exotic Hamiltonians of interest to study. Finally, the synthetic Hamiltonians that can be generated in this way should be solved, at least in tractable limits, in order to provide direct experimental predictions for novel phenomena.

As the fully-quantum light-matter interaction Hamiltonian considered in this and the previous chapter is essentially mediated by off-resonant scattering type processes, other systems based on a similar transition structure between states may prove a fertile test-bed for these ideas and protocols, or similar suitably adapted analogues. Such systems include molecules [207], fermions [208], spins [209], ions [25], and semiconductor [210] and superconducting qubits [211].

- In Chapter 6 we generalised Zeno physics to the regime where the measurements, though still very frequent, are finitely spaced in time. We showed that this leads to additional dynamics, where between measurements, the system temporarily violates the frozen measurement value, then returns to the original

subspace, before the subsequent measurement. We derived effective Hamiltonians to describe this evolution, and showed that in many-body systems these dynamics correspond to correlated processes.

An obvious next step would be to experimentally verify the predictions of QqZD. As outlined in the chapter, a three-state system with a degenerate measurement operator is sufficient for this purpose, and there are thus many systems appropriate for this, as we will discuss below. On the theoretical side, possible avenues for future investigation include studying the effect of variable measurement timesteps, how this may be used to 'steer' the system evolution towards particular states, and increase the robustness of the preservation of the measurement outcome, and also to find applications of the correlated processes generated in this regime.

As a final thought, it is perhaps worth noting the rapid advancement in experimental techniques and quantum technologies. Consider the example of ultracold gases, in which 25 years ago Bose-Einstein condensation had not yet been realised. Since then, not only has this been achieved [212,213], but it has even become commonplace in many laboratories, which have vastly built upon this to incorporate additional aspects, such as optical lattices and optical cavities, and even their union. With this in mind, it is not unreasonable to suggest that we have entered a golden age of quantum technologies, making this work a timely contribution to a burgeoning field. Gleefully, one can look forward with much anticipation to the discoveries and wonders yet to emerge in the field in the coming years and decades, as the power of quantum mechanics is harnessed.

References

[1] Elliott, T. J. & Johnson, T. H. Nondestructive probing of means, variances, and correlations of ultracold-atomic-system densities via qubit impurities. *Physical Review A* **93**, 043612 (2016).

[2] Elliott, T. J., Kozlowski, W., Caballero-Benitez, S. F. & Mekhov, I. B. Multipartite entangled spatial modes of ultracold atoms generated and controlled by quantum measurement. *Physical Review Letters* **114**, 113604 (2015).

[3] Elliott, T. J. & Mekhov, I. B. Engineering many-body dynamics with quantum light potentials and measurements. *Physical Review A* **94**, 013614 (2016).

[4] Elliott, T. J. & Vedral, V. Quantum quasi-Zeno dynamics: Transitions mediated by frequent projective measurements near the Zeno regime. *Physical Review A* **94**, 012118 (2016).

[5] Couto Jr, O. D. D. *et al.* Effect of a GaAsP shell on the optical properties of self-catalyzed GaAs nanowires grown on silicon. *Nano Letters* **12**, 5269–5274 (2012).

[6] Johnson, T. H., Elliott, T. J., Clark, S. R. & Jaksch, D. Capturing exponential variance using polynomial resources: Applying tensor networks to nonequilibrium stochastic processes. *Physical Review Letters* **114**, 090602 (2015).

[7] Elliott, T. J., Mazzucchi, G., Kozlowski, W., Caballero-Benitez, S. F. & Mekhov, I. B. Probing and manipulating fermionic and bosonic quantum gases with quantum light. *Atoms* **3**, 392 (2015).

[8] Mazzucchi, G., Kozlowski, W., Caballero-Benitez, S. F., Elliott, T. J. & Mekhov, I. B. Quantum measurement-induced dynamics of many-body ultracold bosonic and fermionic systems in optical lattices. *Physical Review A* **93**, 023632 (2016).

[9] Planck, M. Zur Theorie des Gesetzes der Energieverteilung im Normalspektrum. *Verhandlungen der Deutschen Physikalischen Gesellschaft* **2**, 237 (1900).

[10] Schrödinger, E. An undulatory theory of the mechanics of atoms and molecules. *Phys. Rev.* **28**, 1049–1070 (1926).

[11] Heisenberg, W. Über quantentheoretische Umdeutung kinematischer und mechanischer Beziehungen. *Zeitschrift für Physik* **33**, 879–893 (1925).

[12] Dirac, P. A. M. The fundamental equations of quantum mechanics. *Proceedings of the Royal Society of London A* **109**, 642–653 (1925).

[13] Peskin, M. E. & Schroeder, D. V. *An Introduction To Quantum Field Theory* (Westview Press, 1995).

[14] Aitchison, I. J. R. & Hey, A. J. G. *Gauge Theories in Particle Physics* (CRC Press, 2002).

[15] Zee, A. *Quantum Field Theory in a Nutshell* (Princeton University Press, 2010).

[16] Vedral, V. *Introduction to Quantum Information Science* (Oxford University Press, 2006).

[17] Nielsen, M. A. & Chuang, I. L. *Quantum Computation and Quantum Information* (Cambridge University Press, 2010).

[18] Jones, J. A. & Jaksch, D. *Quantum Information, Computation and Communication* (Cambridge University Press, 2012).

[19] Haroche, S. & Raimond, J. M. *Exploring the Quantum: Atoms, Cavities, and Photons* (OUP Oxford, 2013).

[20] Feynman, R. P. Simulating physics with computers. *International Journal of Theoretical Physics* **21**, 467–488 (1982).

[21] Deutsch, D. Quantum theory, the Church-Turing principle and the universal quantum computer. *Proceedings of the Royal Society of London A* **400**, 97–117 (1985).

[22] Monroe, C. Quantum information processing with atoms and photons. *Nature* **416**, 238–246 (2002).

[23] Lloyd, S. Universal quantum simulators. *Science* **273**, 1073–1078 (1996).

[24] Bloch, I., Dalibard, J. & Nascimbène, S. Quantum simulations with ultracold quantum gases. *Nature Physics* **8**, 267–276 (2012).

[25] Blatt, R. & Roos, C. F. Quantum simulations with trapped ions. *Nature Physics* **8**, 277–284 (2012).

[26] Lewenstein, M., Sanpera, A. & Ahufinger, V. *Ultracold Atoms in Optical Lattices: Simulating Quantum Many-Body Systems* (Oxford University Press, Oxford, England, 2012).

[27] Bennett, C. H. *et al.* Teleporting an unknown quantum state via dual classical and Einstein-Podolsky-Rosen channels. *Physical Review Letters* **70**, 1895 (1993).

[28] Gu, M., Wiesner, K., Rieper, E. & Vedral, V. Quantum mechanics can reduce the complexity of classical models. *Nature Communications* **3**, 762 (2012).

[29] Mekhov, I. B. & Ritsch, H. Quantum optics with ultracold quantum gases: towards the full quantum regime of the light–matter interaction. *Journal of Physics B* **45**, 102001 (2012).

[30] Wolke, M., Klinner, J., Kessler, H. & Hemmerich, A. Cavity cooling below the recoil limit. *Science* **337**, 75–87 (2012).

[31] Ritsch, H., Domokos, P., Brennecke, F. & Esslinger, T. Cold atoms in cavity-generated dynamical optical potentials. *Reviews of Modern Physics* **85**, 553 (2013).

[32] Schmidt, D., Tomczyk, H., Slama, S. & Zimmermann, C. Dynamical instability of a Bose-Einstein condensate in an optical ring resonator. *Physical Review Letters* **112**, 115302 (2014).

[33] Landig, R., Brennecke, F., Mottl, R., Donner, T. & Esslinger, T. Measuring the dynamic structure factor of a quantum gas undergoing a structural phase transition. *Nature Communications* **6**, 7046 (2015).

[34] Landig, R. *et al.* Quantum phases from competing short-and long-range interactions in an optical lattice. *Nature* **532**, 476 (2016).

[35] Klinder, J., Keßler, H., Bakhtiari, M. R., Thorwart, M. & Hemmerich, A. Observation of a superradiant Mott insulator in the Dicke-Hubbard model. *Physical Review Letters* **115**, 230403 (2015).

[36] Mekhov, I. B., Maschler, C. & Ritsch, H. Probing quantum phases of ultracold atoms in optical lattices by transmission spectra in cavity quantum electrodynamics. *Nature Physics* **3**, 319–323 (2007).

[37] Larson, J., Damski, B., Morigi, G. & Lewenstein, M. Mott-insulator states of ultracold atoms in optical resonators. *Physical Review Letters* **100**, 050401 (2008).

[38] Maschler, C., Mekhov, I. B. & Ritsch, H. Ultracold atoms in optical lattices generated by quantized light fields. *European Physics Journal D* **46**, 545–560 (2008).

[39] Chen, W. & Meystre, P. Cavity QED characterization of many-body atomic states in double-well potentials: Role of dissipation. *Physical Review A* **79**, 043801 (2009).

[40] Gopalakrishnan, S., Lev, B. L. & Goldbart, P. M. Emergent crystallinity and frustration with Bose-Einstein condensates in multimode cavities. *Nature Physics* **5**, 845–850 (2009).

[41] Mekhov, I. B. & Ritsch, H. Quantum nondemolition measurements and state preparation in quantum gases by light detection. *Physical Review Letters* **102**, 020403 (2009).

[42] Strack, P. & Sachdev, S. Dicke quantum spin glass of atoms and photons. *Physical Review Letters* **107**, 277202 (2011).

[43] Habibian, H., Winter, A., Paganelli, S., Rieger, H. & Morigi, G. Bose-glass phases of ultracold atoms due to cavity backaction. *Physical Review Letters* **110**, 075304 (2013).

[44] Piazza, F., Strack, P. & Zwerger, W. Bose-Einstein condensation versus Dicke–Hepp–Lieb transition in an optical cavity. *Annals of Physics* **339**, 135–159 (2013).

[45] Pedersen, M. K., Sørensen, J. J. W. H., Tichy, M. C. & Sherson, J. F. Many-body state engineering using measurements and fixed unitary dynamics. *New Journal of Physics* **16**, 113038 (2014).

[46] Padhi, B. & Ghosh, S. Spin-orbit-coupled Bose-Einstein condensates in a cavity: Route to magnetic phases through cavity transmission. *Physical Review A* **90**, 023627 (2014).

[47] Lee, M. D. & Ruostekoski, J. Classical stochastic measurement trajectories: Bosonic atomic gases in an optical cavity and quantum measurement backaction. *Physical Review A* **90**, 023628 (2014).

[48] Ostermann, S., Grießer, T. & Ritsch, H. Atomic self-ordering in a ring cavity with counterpropagating pump fields. *European Physics Letters* **109**, 43001 (2015).

[49] Kollath, C., Sheikhan, A., Wolff, S. & Brennecke, F. Ultracold fermions in a cavity-induced artificial magnetic field. *Physical Review Letters* **116**, 060401 (2016).

[50] Caballero-Benitez, S. F. & Mekhov, I. B. Quantum optical lattices for emergent many-body phases of ultracold atoms. *Physical Review Letters* **115**, 243604 (2015).

[51] Bakhtiari, M. R., Hemmerich, A., Ritsch, H. & Thorwart, M. Nonequilibrium phase transition of interacting bosons in an intra-cavity optical lattice. *Physical Review Letters* **114**, 123601 (2015).

[52] Dirac, P. A. M. *The Principles of Quantum Mechanics* (Oxford University Press, 1981).

[53] Feynman, L., Leighton, R. B. & Sands, M. *The Feynman Lectures on Physics Vol. 3* (Addison-Wesley, 1964).

[54] Sakurai, J. J. & Napolitano, J. *Modern Quantum Mechanics* (Addison-Wesley, 2011).

[55] Binney, J. & Skinner, D. *The Physics of Quantum Mechanics* (Oxford University Press, 2013).

[56] Glazer, M. & Wark, J. *Statistical Mechanics* (Oxford University Press, 2002).

[57] Sakurai, J. J. *Advanced Quantum Mechanics* (Pearson Education India, 1967).

[58] Schwabl, F. *Advanced Quantum Mechanics* (Springer, 2005).

[59] Altland, A. & Simons, B. D. *Condensed Matter Field Theory* (Cambridge University Press, 2010).

[60] Pachos, J. K. *Introduction to Topological Quantum Computation* (Cambridge University Press, 2012).

[61] Gerry, C. & Knight, P. *Introductory Quantum Optics* (Cambridge University Press, 2005).

[62] Wiseman, H. M. & Milburn, G. J. *Quantum Measurement and Control* (Cambridge University Press, 2009).

[63] Misra, B. & Sudarshan, E. C. G. The Zeno's paradox in quantum theory. *Journal of Mathematical Physics* **18**, 756–763 (1977).

[64] von Neumann, J. *Mathematical Foundations of Quantum Mechanics* (Princeton University Press, 1955).

[65] Teuscher, C. *Alan Turing: Life and Legacy of a Great Thinker* (Springer, 2004).

[66] Facchi, P., Gorini, V., Marmo, G., Pascazio, S. & Sudarshan, E. C. G. Quantum Zeno dynamics. *Physics Letters A* **275**, 12–19 (2000).

[67] Facchi, P. & Pascazio, S. Quantum Zeno subspaces. *Physical Review Letters* **89**, 080401 (2002).

[68] Facchi, P. & Pascazio, S. Quantum Zeno dynamics: mathematical and physical aspects. *Journal of Physics A* **41**, 493001 (2008).

[69] Smelyanskiy, M., Sawaya, N. P. D. & Aspuru-Guzik, A. qHiPSTER: the quantum high performance software testing environment. *arXiv:1601.07195* (2016).

[70] Johnson, T. H., Clark, S. R. & Jaksch, D. What is a quantum simulator? *EPJ Quantum Technology* **1**, 1–12 (2014).

[71] Barz, S., Fitzsimons, J. F., Kashefi, E. & Walther, P. Experimental verification of quantum computation. *Nature Physics* **9**, 727–731 (2013).

[72] Jaksch, D., Bruder, C., Cirac, J. I., Gardiner, C. W. & Zoller, P. Cold bosonic atoms in optical lattices. *Physical Review Letters* **81**, 3108–3111 (1998).

[73] Greiner, M., Mandel, O., Esslinger, T., Hänsch, T. W. & Bloch, I. Quantum phase transition from a superfluid to a Mott insulator in a gas of ultracold atoms. *Nature* **415**, 39–44 (2002).

[74] Ray, M. W., Ruokokoski, E., Kandel, S., Möttönen, M. & Hall, D. S. Observation of Dirac monopoles in a synthetic magnetic field. *Nature* **505**, 657–660 (2014).

[75] Jaksch, D. & Zoller, P. Creation of effective magnetic fields in optical lattices: the Hofstadter butterfly for cold neutral atoms. *New Journal of Physics* **5**, 56 (2003).

[76] Osterloh, K., Baig, M., Santos, L., Zoller, P. & Lewenstein, M. Cold atoms in non-Abelian gauge potentials: from the Hofstadter "moth" to lattice gauge theory. *Physical Review Letters* **95**, 010403 (2005).

[77] Dalibard, J., Gerbier, F., Juzeliūnas, G. & Öhberg, P. Colloquium: Artificial gauge potentials for neutral atoms. *Reviews of Modern Physics* **83**, 1523 (2011).

[78] Aidelsburger, M. *et al.* Experimental realization of strong effective magnetic fields in an optical lattice. *Physical Review Letters* **107**, 255301 (2011).

[79] Banerjee, D. *et al.* Atomic quantum simulation of dynamical gauge fields coupled to fermionic matter: from string breaking to evolution after a quench. *Physical Review Letters* **109**, 175302 (2012).

[80] Zohar, E., Cirac, J. I. & Reznik, B. Simulating compact quantum electrodynamics with ultracold atoms: probing confinement and nonperturbative effects. *Physical Review Letters* **109**, 125302 (2012).

[81] Marcos, D., Rabl, P., Rico, E. & Zoller, P. Superconducting circuits for quantum simulation of dynamical gauge fields. *Physical Review Letters* **111**, 110504 (2013).

[82] Tagliacozzo, L., Celi, A., Orland, P., Mitchell, M. & Lewenstein, M. Simulation of non-Abelian gauge theories with optical lattices. *Nature Communications* **4** (2013).

[83] Aidelsburger, M. *et al.* Realization of the Hofstadter Hamiltonian with ultracold atoms in optical lattices. *Physical Review Letters* **111**, 185301 (2013).

[84] Miyake, H., Siviloglou, G. A., Kennedy, C. J., Burton, W. C. & Ketterle, W. Realizing the Harper Hamiltonian with laser-assisted tunneling in optical lattices. *Physical Review Letters* **111**, 185302 (2013).

[85] Hauke, P., Marcos, D., Dalmonte, M. & Zoller, P. Quantum simulation of a lattice Schwinger model in a chain of trapped ions. *Physical Review X* **3**, 041018 (2013).

[86] Goldman, N., Juzeliūnas, G., Öhberg, P. & Spielman, I. Light-induced gauge fields for ultracold atoms. *Reports on Progress in Physics* **77**, 126401–126460 (2014).

[87] Baumann, K., Guerlin, C., Brennecke, F. & Esslinger, T. Dicke quantum phase transition with a superfluid gas in an optical cavity. *Nature* **464**, 1301–1306 (2010).

[88] Shannon, C. E. A mathematical theory of communication. *The Bell System Technical Journal* **27**, 379–423 (1948).

[89] Amico, L., Fazio, R., Osterloh, A. & Vedral, V. Entanglement in many-body systems. *Review Modern Physics* **80**, 517 (2008).

[90] Horodecki, R., Horodecki, P., Horodecki, M. & Horodecki, K. Quantum entanglement. *Revies of Modern Physics* **81**, 865 (2009).

[91] Horodecki, R. & Horodecki, M. Information-theoretic aspects of inseparability of mixed states. *Physical Review A* **54**, 1838–1843 (1996).

[92] Vidal, G. & Werner, R. F. Computable measure of entanglement. *Physical Review A* **65**, 032314 (2002).

[93] Essler, F. H. L., Frahm, H., Göhmann, F., Klümper, A. & Korepin, V. E. *The one-dimensional Hubbard model* (Cambridge University Press, 2005).

[94] Dutta, O. *et al.* Non-standard Hubbard models in optical lattices: a review. *Reports on Progress in Physics* **78**, 066001 (2015).

[95] Woodgate, G. K. *Elementary Atomic Structure* (Oxford University Press, 1980).

[96] Foot, C. J. *Atomic Physics* (Oxford University Press, 2004).

[97] Pethick, C. J. & Smith, H. *Bose-Einstein Condensation in Dilute Gases* (Cambridge University Press, 2001).

[98] Pitaevskii, L. & Stringari, S. *Bose-Einstein Condensation* (Oxford University Press, 2003).

[99] Wannier, G. H. The structure of electronic excitation levels in insulating crystals. *Physical Review* **52**, 191 (1937).

[100] Rokhsar, D. S. & Kotliar, B. G. Gutzwiller projection for bosons. *Physical Review B* **44**, 10328 (1991).

[101] Sheshadri, K., Krishnamurthy, H. R., Pandit, R. & Ramakrishnan, T. V. Superfluid and insulating phases in an interacting-boson model: Mean-field theory and the RPA. *European Physics Letters* **22**, 257 (1993).

[102] Mattis, D. C. *The Theory of Magnetism Made Simple: An Introduction to Physical Concepts and to Some Useful Mathematical Methods* (World Scientific, 2006).

[103] Kramers, H. A. L'interaction Entre les Atomes Magnétogènes dans un Cristal Paramagnétique. *Physica* **1**, 182 – 192 (1934).

[104] Anderson, P. W. Antiferromagnetism. Theory of superexchange interaction. *Physical Review* **79**, 350–356 (1950).

[105] Scully, M. O. & Zubairy, M. S. *Quantum Optics* (Cambridge University Press, 1997).

[106] Jaynes, E. T. & Cummings, F. W. Comparison of quantum and semiclassical radiation theories with application to the beam maser. *Proceedings of the IEEE* **51**, 89–109 (1963).

[107] Bloch, I., Dalibard, J. & Zwerger, W. Many-body physics with ultracold gases. *Reviews of Modern Physics* **80**, 885 (2008).

[108] Hadzibabic, Z. *et al.* Fiftyfold improvement in the number of quantum degenerate fermionic atoms. *Physical Review Letters* **91**, 160401 (2003).

[109] Altman, E., Demler, E. & Lukin, M. D. Probing many-body states of ultracold atoms via noise correlations. *Physical Review A* **70**, 013603 (2004).

[110] Fölling, S. *et al.* Spatial quantum noise interferometry in expanding ultracold atom clouds. *Nature* **434**, 481–484 (2005).

[111] Perrin, H. Ultracold atoms and Bose-Einstein condensation for quantum metrology. *EPJ Special Topics* **172**, 37–55 (2009).

[112] Nelson, K. D., Li, X. & Weiss, D. S. Imaging single atoms in a three-dimensional array. *Nature Physics* **3**, 556–560 (2007).

[113] Bakr, W. S., Gillen, J. I., Peng, A., Folling, S. & Greiner, M. A quantum gas microscope for detecting single atoms in a Hubbard-regime optical lattice. *Nature* **462**, 74–77 (2009).

[114] Sherson, J. F. *et al.* Single-atom resolved fluorescence imaging of an atomic Mott insulator. *Nature* **467**, 68–72 (2010).

[115] Weitenberg, C. *et al.* Single-spin addressing in an atomic Mott insulator. *Nature* **471**, 319–324 (2011).

[116] Recati, A., Fedichev, P. O., Zwerger, W., Von Delft, J. & Zoller, P. Atomic quantum dots coupled to a reservoir of a superfluid Bose-Einstein condensate. *Physical Review Letters* **94**, 40404 (2005).

[117] Bruderer, M. & Jaksch, D. Probing BEC phase fluctuations with atomic quantum dots. *New Journal of Physics* **8**, 87 (2006).

[118] Goold, J., Fogarty, T., Gullo, N. L., Paternostro, M. & Busch, T. Orthogonality catastrophe as a consequence of qubit embedding in an ultracold fermi gas. *Physical Review A* **84**, 063632 (2011).

[119] Knap, M. *et al.* Time-dependent impurity in ultracold fermions: Orthogonality catastrophe and beyond. *Physical Review X* **2**, 041020 (2012).

[120] Dorner, R. *et al.* Extracting quantum work statistics and fluctuation theorems by single-qubit interferometry. *Physical Review Letters* **110**, 230601 (2013).

[121] Haikka, P., McEndoo, S. & Maniscalco, S. Non-Markovian probes in ultracold gases. *Physical Review A* **87**, 012127 (2013).

[122] Borrelli, M., Haikka, P., De Chiara, G. & Maniscalco, S. Non-Markovian qubit dynamics induced by Coulomb crystals. *Physical Review A* **88**, 010101 (2013).

[123] Mazzola, L., De Chiara, G. & Paternostro, M. Measuring the characteristic function of the work distribution. *Physical Review Letters* **110**, 230602 (2013).

[124] Haikka, P. & Maniscalco, S. Non-Markovian quantum probes. *Open Systems & Information Dynamics* **21**, 1440005 (2014).

[125] Sabín, C., White, A., Hackermuller, L. & Fuentes, I. Impurities as a quantum thermometer for a Bose-Einstein condensate. *Scientific Reports* **4**, 6436 (2014).

[126] Fusco, L. *et al.* Assessing the nonequilibrium thermodynamics in a quenched quantum many-body system via single projective measurements. *Physical Review X* **4**, 031029 (2014).

[127] Batalhão, T. B. *et al.* Experimental reconstruction of work distribution and study of fluctuation relations in a closed quantum system. *Physical Review Letters* **113**, 140601 (2014).

[128] Hangleiter, D. *et al.* Nondestructive selective probing of phononic excitations in a cold Bose gas using impurities. *Physical Review A* **91**, 013611 (2015).

[129] Johnson, T. H., Cosco, F., Mitchison, M. T., Jaksch, D. & Clark, S. R. Thermometry of ultracold atoms via nonequilibrium work distributions. *Physical Review A* **93**, 053619 (2016).

[130] Cosco, F., Borrelli, M., Plastina, F. & Maniscalco, S. Detection of superfluid excitations via local quantum probing. *arXiv:1511.00833* (2015).

[131] Catani, J. *et al.* Quantum dynamics of impurities in a one-dimensional bose gas. *Physical Review A* **85**, 023623 (2012).

[132] Scelle, R., Rentrop, T., Trautmann, A., Schuster, T. & Oberthaler, M. K. Motional coherence of fermions immersed in a bose gas. *Physical Review Letters* **111**, 070401 (2013).

[133] Inouye, S. *et al.* Observation of heteronuclear Feshbach resonances in a mixture of bosons and fermions. *Physical Review Letters* **93**, 183201 (2004).

[134] Roati, G., Riboli, F., Modugno, G. & Inguscio, M. Fermi-bose quantum degenerate ^{40}K-^{87}Rb mixture with attractive interaction. *Physical Review Letters* **89**, 150403 (2002).

[135] Zaccanti, M. *et al.* Control of the interaction in a fermi-bose mixture. *Physical Review A* **74**, 041605 (2006).

[136] Günter, K., Stöferle, T., Moritz, H., Köhl, M. & Esslinger, T. Bose-fermi mixtures in a three-dimensional optical lattice. *Physical Review Letters* **96**, 180402 (2006).

[137] Daley, A. J., Pichler, H., Schachenmayer, J. & Zoller, P. Measuring entanglement growth in quench dynamics of bosons in an optical lattice. *Physical Review Letters* **109**, 020505 (2012).

[138] Vidal, G. Efficient classical simulation of slightly entangled quantum computations. *Physical Review Letters* **91**, 147902 (2003).

[139] Vidal, G. Efficient simulation of one-dimensional quantum many-body systems. *Physical Review Letters* **93**, 040502 (2004).

[140] Johnson, T. H., Clark, S. R., Bruderer, M. & Jaksch, D. Impurity transport through a strongly interacting bosonic quantum gas. *Physical Review A* **84**, 023617 (2011).

[141] Hastie, T. J. & Tibshirani, R. J. *Generalized Additive Models* (Taylor & Francis, 1990).

[142] Maik, M., Hauke, P., Dutta, O., Lewenstein, M. & Zakrzewski, J. Density-dependent tunneling in the extended Bose–Hubbard model. *New Journal of Physics* **15**, 113041 (2013).

[143] Verstraete, F., Murg, V. & Cirac, J. I. Matrix product states, projected entangled pair states, and variational renormalization group methods for quantum spin systems. *Advances in Physics* **57**, 143–224 (2008).

[144] Verstraete, F. & Cirac, J. I. Matrix product states represent ground states faithfully. *Physical Review B* **73**, 094423 (2006).

[145] Eisert, J., Cramer, M. & Plenio, M. B. Colloquium: Area laws for the entanglement entropy. *Reviews of Modern Physics* **82**, 277 (2010).

[146] Suzuki, M. Fractal decomposition of exponential operators with applications to many-body theories and Monte Carlo simulations. *Physics Letters A* **146**, 319–323 (1990).

[147] Mekhov, I. B. & Ritsch, H. Quantum optics with quantum gases: Controlled state reduction by designed light scattering. *Physical Review A* **80**, 013604 (2009).

[148] Kozlowski, W., Caballero-Benitez, S. F. & Mekhov, I. B. Probing matter-field and atom-number correlations in optical lattices by global nondestructive addressing. *Physical Review A* **92**, 013613 (2015).

[149] Pichler, H., Daley, A. J. & Zoller, P. Nonequilibrium dynamics of bosonic atoms in optical lattices: Decoherence of many-body states due to spontaneous emission. *Physical Review A* **82**, 063605 (2010).

[150] Miyake, H. *et al.* Bragg scattering as a probe of atomic wave functions and quantum phase transitions in optical lattices. *Physical Review Letters* **107**, 175302 (2011).

[151] Mekhov, I. B. & Ritsch, H. Quantum optics with quantum gases. *Laser Physics* **19**, 610 (2009).

[152] Macon, N. & Spitzbart, A. Inverses of Vandermonde matrices. *American Mathematics Monthly* **65**, 95–100 (1958).

[153] Bartlett, S. D., Rudolph, T. & Spekkens, R. W. Reference frames, superselection rules, and quantum information. *Reviews of Modern Physics* **79**, 555 (2007).

[154] Lloyd, S. Coherent quantum feedback. *Physical Review A* **62**, 022108 (2000).

[155] Nelson, R. J., Weinstein, Y., Cory, D. & Lloyd, S. Experimental demonstration of fully coherent quantum feedback. *Physical Review Letters* **85**, 3045–3048 (2000).

[156] Ivanov, D. A. & Ivanova, T. Y. Feedback-enhanced self-organization of atoms in an optical cavity. *JETP Letters* **100**, 481–485 (2014).

[157] Embrey, C. S., Turnbull, M. T., Petrov, P. G. & Boyer, V. Observation of localized multi-spatial-mode quadrature squeezing. *Physical Review X* **5**, 031004 (2015).

[158] Braunstein, S. L. & McLachlan, R. I. Generalized squeezing. *Physical Review A* **35**, 1659 (1987).

[159] Dicke, R. H. Coherence in spontaneous radiation processes. *Physical Review* **93**, 99–110 (1954).

[160] Carmichael, H. *An Open Systems Approach to Quantum Optics* (Springer, 1993).

[161] Simon, C. Natural entanglement in Bose-Einstein condensates. *Physical Review A* **66**, 052323 (2002).

[162] Ruostekoski, J. & Walls, D. Nondestructive optical measurement of relative phase between two Bose-Einstein condensates. *Physical Review A* **56**, 2996–3006 (1997).

[163] Horak, P. & Barnett, S. M. Creation of coherence in Bose-Einstein condensates by atom detection. *Journal of Physics B* **32**, 3421 (1999).

[164] Ekert, A. K. *et al.* Direct estimations of linear and nonlinear functionals of a quantum state. *Physical Review Letters* **88**, 217901 (2002).

[165] Alves, C. M., Horodecki, P., Oi, D. K. L., Kwek, L. C. & Ekert, A. K. Direct estimation of functionals of density operators by local operations and classical communication. *Physical Review A* **68**, 032306 (2003).

[166] Abanin, D. A. & Demler, E. Measuring entanglement entropy of a generic many-body system with a quantum switch. *Physical Review Letters* **109**, 020504 (2012).

[167] Pichler, H., Bonnes, L., Daley, A. J., Läuchli, A. M. & Zoller, P. Thermal versus entanglement entropy: A measurement protocol for fermionic atoms with a quantum gas microscope. *New Journal of Physics* **15**, 063003 (2013).

[168] Islam, R. *et al.* Measuring entanglement entropy in a quantum many-body system. *Nature* **528**, 77–83 (2015).

[169] Jaksch, D., Briegel, H. J., Cirac, J. I., Gardiner, C. W. & Zoller, P. Entanglement of atoms via cold controlled collisions. *Physical Review Letters* **82**, 1975 (1999).

[170] Carteret, H. A. Noiseless quantum circuits for the Peres separability criterion. *Physical Review Letters* **94**, 040502 (2005).

[171] Trotzky, S. *et al.* Time-resolved observation and control of superexchange interactions with ultracold atoms in optical lattices. *Science* **319**, 295–299 (2008).

[172] Bastarrachea-Magnani, M. A., Lerma-Hernández, S. & Hirsch, J. G. Comparative quantum and semiclassical analysis of atom-field systems. I. Density of states and excited-state quantum phase transitions. *Physical Review A* **89**, 032101 (2014).

[173] de Aguiar, M. A. M., Furuya, K. & Nemes, M. C. The classical analogue of the super-radiant phase transition in the Dicke model. *Quantum Optics* **3**, 305 (1991).

[174] Horn, D. Finite matrix models with continuous local gauge invariance. *Physics Letters B* **100**, 149–151 (1981).

[175] Orland, P. & Rohrlich, D. Lattice gauge magnets: Local isospin from spin. *Nuclear Physics B* **338**, 647–672 (1990).

[176] Brower, R., Chandrasekharan, S. & Wiese, U.-J. QCD as a quantum link model. *Physical Review D* **60**, 094502 (1999).

[177] Banerjee, D. *et al.* Atomic quantum simulation of U(N) and SU(N) non-Abelian lattice gauge theories. *Physical Review Letters* **110**, 125303 (2013).

[178] Stannigel, K. *et al.* Constrained dynamics via the Zeno effect in quantum simulation: Implementing non-Abelian lattice gauge theories with cold atoms. *Physical Review Letters* **112**, 120406 (2014).

[179] Itano, W. M., Heinzen, D. J., Bollinger, J. J. & Wineland, D. J. Quantum Zeno effect. *Physical Review A* **41**, 2295–2300 (1990).

[180] Kwiat, P., Weinfurter, H., Herzog, T., Zeilinger, A. & Kasevich, M. A. Interaction-free measurement. *Physical Review Letters* **74**, 4763–4766 (1995).

[181] Xiao, L. & Jones, J. A. NMR analogues of the quantum Zeno effect. *Physical Letters A* **359**, 424 – 427 (2006).

[182] Streed, E. W. *et al.* Continuous and pulsed quantum Zeno effect. *Physical Review Letters* **97**, 260402 (2006).

[183] Signoles, A. *et al.* Confined quantum Zeno dynamics of a watched atomic arrow. *Nature Physics* **10**, 715–719 (2014).

[184] Schäfer, F. *et al.* Experimental realization of quantum Zeno dynamics. *Nature Communications* **5**, 3194 (2014).

[185] Patil, Y. S., Chakram, S. & Vengalattore, M. Measurement-induced localization of an ultracold lattice gas. *Physical Review Letters* **115**, 140402 (2015).

[186] Beige, A., Braun, D., Tregenna, B. & Knight, P. L. Quantum computing using dissipation to remain in a decoherence-free subspace. *Physical Review Letters* **85**, 1762 (2000).

[187] Nakazato, H., Takazawa, T. & Yuasa, K. Purification through Zeno-like measurements. *Physical Review Letters* **90**, 060401 (2003).

[188] Nakazato, H., Unoki, M. & Yuasa, K. Preparation and entanglement purification of qubits through Zeno-like measurements. *Physical Review A* **70**, 012303 (2004).

[189] Erez, N., Aharonov, Y., Reznik, B. & Vaidman, L. Correcting quantum errors with the Zeno effect. *Physical Review A* **69**, 062315 (2004).

[190] Wu, L.-A., Lidar, D. A. & Schneider, S. Long-range entanglement generation via frequent measurements. *Physical Review A* **70**, 032322 (2004).

[191] Compagno, G. *et al.* Distillation of entanglement between distant systems by repeated measurements on an entanglement mediator. *Physical Review A* **70**, 052316 (2004).

[192] Militello, B. & Messina, A. Distilling angular momentum nonclassical states in trapped ions. *Physical Review A* **70**, 033408 (2004).

[193] Wang, X.-B., You, J. Q. & Nori, F. Quantum entanglement via two-qubit quantum Zeno dynamics. *Physical Review A* **77**, 062339 (2008).

[194] Erez, N., Gordon, G., Nest, M. & Kurizki, G. Thermodynamic control by frequent quantum measurements. *Nature* **452**, 724–727 (2008).

[195] Verstraete, F., Wolf, M. M. & Cirac, J. I. Quantum computation and quantum-state engineering driven by dissipation. *Nature Physics* **5**, 633–636 (2009).

[196] Yi, W., Diehl, S., Daley, A. J. & Zoller, P. Driven-dissipative many-body pairing states for cold fermionic atoms in an optical lattice. *New Journal of Physics* **14**, 055002 (2012).

[197] Paz-Silva, G. A., Rezakhani, A. T., Dominy, J. M. & Lidar, D. A. Zeno effect for quantum computation and control. *Physical Review Letters* **108**, 080501 (2012).

[198] Raimond, J. M. *et al.* Quantum Zeno dynamics of a field in a cavity. *Physical Review A* **86**, 032120 (2012).

[199] Burgarth, D. *et al.* Non-Abelian phases from quantum Zeno dynamics. *Physical Review A* **88**, 042107 (2013).

[200] Everest, B., Hush, M. R. & Lesanovsky, I. Many-body out-of-equilibrium dynamics of hard-core lattice bosons with nonlocal loss. *Physical Review B* **90**, 134306 (2014).

[201] Mazzucchi, G., Caballero-Benitez, S. F. & Mekhov, I. B. Quantum measurement-induced antiferromagnetic order and density modulations in ultracold fermi gases in optical lattices. *arXiv:1510.04883* (2015).

[202] Layden, D., Martín-Martínez, E. & Kempf, A. Perfect Zeno-like effect through imperfect measurements at a finite frequency. *Physical Review A* **91**, 022106 (2015).

[203] Dhar, S., Dasgupta, S., Dhar, A. & Sen, D. Detection of a quantum particle on a lattice under repeated projective measurements. *Physical Review A* **91**, 062115 (2015).

[204] Ruseckas, J. & Kaulakys, B. Real measurements and the quantum Zeno effect. *Physical Review A* **63**, 062103 (2001).

[205] Kozlowski, W., Caballero-Benitez, S. F. & Mekhov, I. B. Non-Hermitian dynamics in the quantum Zeno limit. *Physical Review A* **94**, 012123 (2016).

[206] Liu, N. *et al.* Power of one qumode for quantum computation. *Physical Review A* **93**, 052304 (2016).

[207] Mekhov, I. B. Quantum non-demolition detection of polar molecule complexes: dimers, trimers, tetramers. *Laser Physics* **23**, 015501 (2013).

[208] Ruostekoski, J., Foot, C. J. & Deb, A. B. Light scattering for thermometry of fermionic atoms in an optical lattice. *Physics Review Letters* **103**, 170404 (2009).

[209] Cordobes Aguilar, F., Ho, A. F. & Ruostekoski, J. Optical signatures of antiferromagnetic ordering of fermionic atoms in an optical lattice. *Physical Review X* **4**, 031036 (2014).

[210] Trauzettel, B., Bulaev, D. V., Loss, D. & Burkard, G. Spin qubits in graphene quantum dots. *Nature Physics* **3**, 192–196 (2007).

[211] Fink, J. M. *et al.* Dressed collective qubit states and the Tavis-Cummings model in circuit QED. *Physical Review Letters* **103**, 083601 (2009).

[212] Davis, K. B. *et al.* Bose-Einstein condensation in a gas of sodium atoms. *Physical Review Letters* **75**, 3969 (1995).

[213] Anderson, M. H., Ensher, J. R., Matthews, M. R., Wieman, C. E. & Cornell, E. A. Observation of Bose-Einstein condensation in a dilute atomic vapor. *Science* **269**, 198–201 (1995).